TECTONIC INFLUENCES ON SURFICIAL PROCESSES AND DEFORMATION ALONG THE NANKAI ACCRETIONARY PRISM, SOUTHWEST JAPAN

A DISSERTATION SUBMITTED TO THE GRADUATE DIVISION OF THE UNIVERSITY OF HAWAIʻI AT MĀNOA IN PARTIAL FULFILLMENT OF THE REQUIREMENTS FOR THE DEGREE OF

DOCTOR OF PHILOSOPHY

IN

EARTH AND PLANETARY SCIENCES

March 2019

By

Jason K. Lackey

Dissertation Committee:

Gregory Moore, Chairperson
Patricia Fryer
Bridget Smith-Konter
Garrett Apuzen-Ito
Horst Brandes

Keywords: Seismic, Landslides, Nankai, Accretionary, Subduction, Kinematics

ABSTRACT

This dissertation presents interpretations of new, high-resolution multibeam bathymetric data, reprocessed 3D seismic data and drill cores from the southern Kumano Basin and Nankai accretionary prism off southwest Japan. These combined data sets show a widely variable surface morphology and provide insight into: 1) the distribution of landsliding along the prism, 2) a nested series of moderately-sized mass transport deposits (MTDs) along the seaward side of the forearc basin, 3) and record ~2.87 million years of structural and depositional history of a trench slope basin. We mapped and cataloged 718 individual landslide scars, 56% of which are part of complex (multi-slide) structures. One of the more prominent complexes in the forearc basin is completely contained within the 3D seismic volume and dates to ~0.3 – 0.9 Ma. A kinematic investigation revealed 10 individual landslides that originate from the same prominent scar as a likely result of earthquake cycle related faulting along a regional out-of-sequence thrust (megasplay fault). Fault related landsliding also occurs within a trench slope basin seaward of the outer ridge. The 3D seismic volume and drill core data permit a kinematic reconstruction of the basin since ~2.4 Ma. In the NE, deformation is accommodated by the main megasplay while deformation in the SW is along break-backward imbricate branches of the megasplay. We suggest that these differences are caused by subsurface geometry and seamount subduction and directly influence the depth and surface morphology of the trench slope basin via landsliding.

TABLE OF CONTENTS

LIST OF TABLES

LIST OF FIGURES

CHAPTER 1
INTRODUCTION

This dissertation's focus is submarine landsliding on the Nankai accretionary prism off southwest Japan. Submarine landslides are an important process by which sediment is redistributed across the seafloor. They help shape the seafloor, range in size from a few hundred square meters to hundreds of square kilometers, and can cause damage both by destroying submarine infrastructure and generating tsunamis (Prior & Coleman 1978; Moore *et al.* 1989; Bondevik *et al.* 1997; Lee 2009). In an accretionary prism environment, such as the Nankai Trough, landslides are largely linked to the growth of the prism and the prism's underlying tectonics (Ikari *et al.* 2011). The study area is located where the Philippine Sea Plate is presently subducting under the Amur plate at a rate of 4 to 6 cm yr^{-1} (Kimura *et al.* 2007a). The Nankai Trough extends roughly 120 km NE and 400 km SW of the study area and is paralleled by the Cretaceous and Tertiary Shimanto accretionary complex that is exposed on Kyushu, Honshu and Shikoku Islands (Taira 2001). The NW oblique subduction has led to the creation of both an accretionary prism spanning roughly 700 km as well as a large right lateral strike-slip fault, known as the Median Tectonic Line, along the SW portion of Japan (Fig. 1.1; Fitch 1972; Taira 2001). While there are many factors that both precondition and cause slopes to fail, here we aim to better understand the mechanisms by which landsliding is initiated and distributed in an accretionary prism.

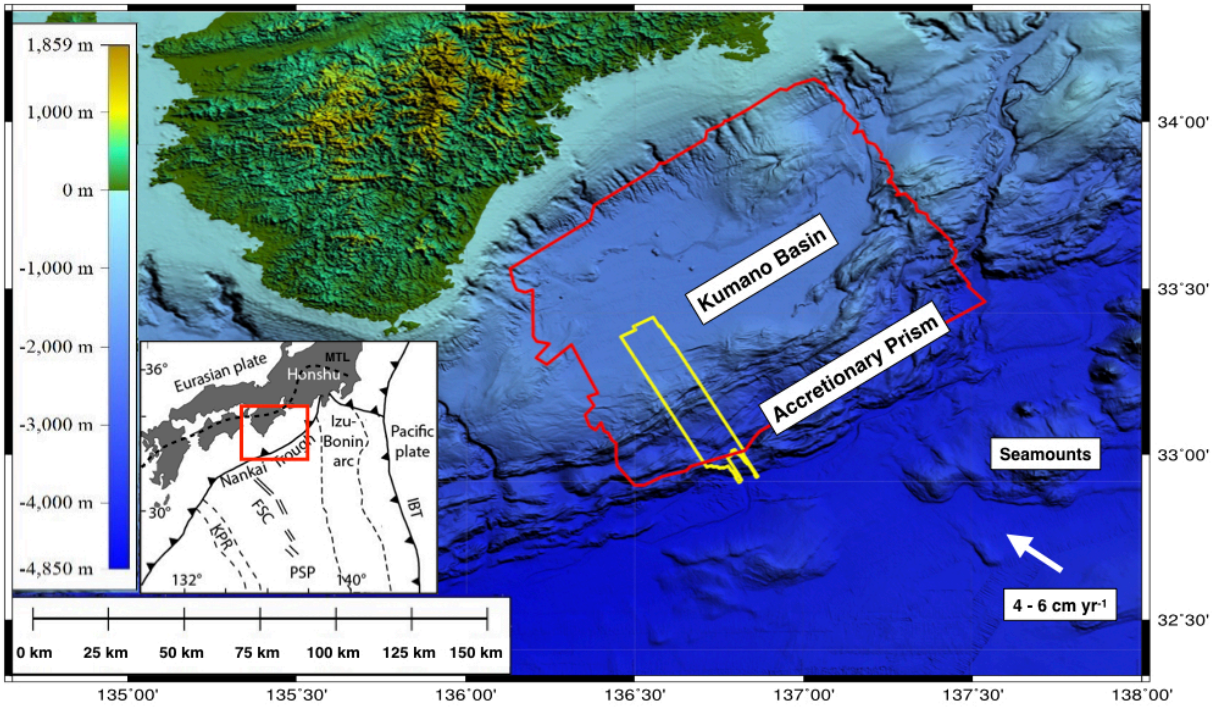

Fig. 1.1. Bathymetry of the study are and surrounding region. The red outline represents the area of high-resolution bathymetry while the yellow outline represents the area of a 3D seismic volume. PSP = Philippine Sea Plate; FSC = Fossil Spreading Center; KPR = Kyushu-Palau Ridge; MTL = Median Tectonic Line; IBT = Izu-Bonin Trench.

Chapter Two (Lackey *et al.* 2018a) involves a study of surficial processes along the accretionary prism. By locating landslides on the seafloor, the goal is to create a catalog of landslides and try to determine any spatial or temporal interactions between faults and landslides. In total we mapped more than 718 individual landslide scars and three distinct fault populations over a 4,000 square kilometer area. Of the 718 landslides, 80 were found to have a spatial relationship with a fault. This means that while faulting is definitely related to and a cause of landsliding, it is not the primary cause nor primary preconditioning mechanism. Therefore, something else, such as slope over steepening, seismic loading, or gas hydrate dissociation is at work behind causing these landslides (Westbrook *et al.* 2009; Bangs *et al.* 2010; Underwood & Moore 2012; Moore & Strasser 2016; Kremer *et al.* 2017).

Chapter Three (Lackey *et al.* 2018b) takes a much more detailed look at two landslide scars within the Kumano Basin as discussed in Chapter Two. One of the second chapter's findings was a noticeable lack of surficial landslide deposits, considering the large number of scars that were identified (Lackey *et al.* 2018a). We focused on two scars without deposits that are located within a 3D seismic survey (Moore *et al.* 2009). This would allow us to infer what happened to the deposits by either locating them in the data or by using kinematic indicators (Bull *et al.* 2009) to determine where they arrested. Although initially identified as two landslides, we found that they are actually at least 10 landslides nested together (3 deposits on the surface and 7 in the subsurface). We concluded that the location of the landslides is likely explained by faulting related to post-seismic relaxation during the earthquake cycle (Sacks *et al.* 2013).

The fourth chapter takes a detailed look at the seaward side of the prism using the 3D seismic data. Here, we aim to investigate the tectonic influences on a prominent trench slope basin being overridden by the megasplay. Several landslide scars identified in Chapter Two are located within this basin and may be influenced by the megasplay or other subsurface structures. The 3D survey allows us to take a detailed, subsurface look at the true interactions between these landslides and the subsurface geology (Strasser *et al.* 2009; Kimura *et al.* 2011; Strasser *et al.* 2011). To do this, we performed a temporal reconstruction of the displacement of the prism and faults using biostratigraphic age constraints from Integrated Ocean Drilling Program (IODP) sediment cores (Expedition 316 Scientists 2009a, b; Strasser *et al.* 2012; Strasser *et al.* 2014). This provided a working kinematic model for the prism and how it changes the overlying trench slope basin through faulting and subsequent landsliding.

CHAPTER 2

SPATIAL AND TEMPORAL CROSS-CUTTING RELATIONSHIPS BETWEEN FAULT STRUCTURES AND SLOPE FAILURES ALONG THE OUTER KUMANO BASIN AND NANKAI ACCRETIONARY WEDGE, SOUTHWEST JAPAN

This chapter has been published as: Lackey JK, Moore GF, Strasser M, Kopf A, Ferreira CS (2018) Spatial and temporal cross-cutting relationships between fault structures and slope failures along the outer Kumano Basin and Nankai accretionary wedge, SW Japan. Subaqueous Mass Movements. Geological Society, London, Special Publications, 477.

Abstract

New, high-resolution multi-beam bathymetric data from RV *Sonne* cruise SO251 show a widely variable surface morphology along the southern Kumano Basin and Nankai accretionary prism off SW Japan. Combined with a three-dimensional seismic volume, these data provide insight into the ubiquitous and varied nature of faulting typical of accretionary prism settings, a high number of submarine landslides across the entire study area that vary both spatially and temporally, a pronounced absence of slide deposit bathymetric manifestations, widely varied slope angles and a potential subducted seamount scar. We have mapped scars of 442 primary and 184 secondary landslides and have measured the areas evacuated by these slides. Most of the slides are completely disintegrative, so surficial landslide deposits are almost absent. The incidence with which temporally sequential slope failures and fault structures cross-cut themselves and one another provides evidence of potential failure pre-conditioning such as gas hydrates, pore fluid overpressures and bottom current activity. Seismic loading and slope over-steepening are then the most likely final trigger mechanisms to slope failure. The majority of observed landslides (64%) occur seawards of the outer ridge, providing insight into the relationship between surficial landsliding and subsurface tectonic processes along this accretionary prism.

Introduction

Roughly 23% of the global population lives within 100 m elevation and 100 km distance from a shoreline (Nicholas & Small 2002). This fact brings to light the need to understand the natural hazards to which almost 1/4 of the global population are exposed. These hazards include landslides, local and eustatic sea level changes, storm activity, seismicity, volcanism, and tsunamis. Of these hazards, subaqueous landslides are some of the least understood and characterized phenomena affecting coastal populations and close-to-shore operations due to their inaccessible and unpredictable nature. Evidence of the potential impact was documented in the past during events such as the Storegga landslide in Norway 7200 years BP. This subaqueous landslide was massive enough to cause a tsunami that affected the entire coast of Norway, to include a 10 to 11 m run-up most proximal to the slide scar (Bondevik *et al.* 1997).

Subaqueous landslides can occur on a great variety of slopes (ranging from < 0.01º to vertical (Prior & Coleman 1978)) in many different environments all over the world including both active and passive margins, along the flanks of volcanic islands, and river deltas (Prior & Coleman 1978; Moore *et al.* 1989; Lee 2009). They are characterized by their size, shape, and kinematics (Ward & Day 2001) to distinguish between such categories as slides, rockfalls, and debris flows. However, for the purposes of this study, the terms “landslide” and “slide” will be used interchangeably in a general sense while more specific terms will be reserved for specific instances and occurrences.

To characterize submarine landslides on the active Nankai Trough accretionary prism, we use high-resolution multibeam bathymetric data, regional two-dimensional (2D) seismic reflection lines, and a three-dimensional (3D) seismic data set (Moore *et al.* 2009) to identify their unique structure and morphology. By integrating analysis of both of these data types, we can identify both surface characteristics on the sea floor and subsurface behavior of the landslide deposit after it has arrested. This aids in characterizing the landslide type and relative age. These data provide the unique opportunity to investigate the distribution of subaqueous landslides and other bathymetric features along an active accretionary margin. By mapping and characterizing this region in detail we aim to gain

a greater understanding of landslides and their potential triggers in depositional/accretionary environments. Not only will this aid in landslide research for future hazard mitigation, but it may also provide insight into possible links between modern subaqueous lithologies and lithologies observed in outcrops via identification of landslide scar morphology and mass transport deposits (MTDs) (Sharman *et al.* 2017).

Study Area

The study area is within the Nankai Trough subduction zone where the Philippine Sea Plate is presently subducting under the Amur plate at a rate of 4 to 6 cm yr^{-1} (Kimura *et al.* 2007a). The Nankai Trough extends roughly 120 km NE and 400 km SW of the study area and is paralleled by the Cretaceous and Tertiary Shimanto accretionary complex that is exposed on Kyushu, Honshu and Shikoku Islands (Taira 2001). The NW oblique subduction has led to the creation of both an accretionary prism spanning roughly 700 km as well as a large right lateral strike-slip fault, known as the Median Tectonic Line, along the SW portion of Japan (Fitch 1972; Taira 2001). The prism is divided into three sections: the inner and outer wedge and their transition zone (Kimura *et al.* 2007b). The present study area is located in the transition zone, characterized by steep surface slopes and an internal structure of out-of-sequence thrusts, and inner wedge zone, characterized by in-sequence imbricate thrusts (Kimura *et al.* 2007b). The accreted sediment is primarily terrigenous detritus from Japan and hemipelagic on the Philippine Sea Plate (Underwood and Moore 2012). The upper part of the hemipelagic section from the Philippine Sea Plate is accreted while the lower part is subducted beyond the inner prism (e.g., Kinoshita *et al.* 2009; Kimura *et al.* 2011; Strasser *et al.* 2011; Strasser *et al.* 2012; Underwood and Moore 2012; Moore *et al.* 2014). The inner prism is overlain by the Kumano forearc basin. The seismic regime of the Nankai region is well established with a recurrence time of roughly 100 to 200 years for large earthquakes (Ando 1975). The rapid growth of the accretionary prism is an important factor for large, repeated earthquakes in this subduction zone setting (Ruff & Kanamori 1980). Of particular interest to the present study, the hanging wall block of the seismogenic fault zone is composed entirely of the accretionary prism. This, in turn, promotes surface erosion along the

entirety of the trough that partly manifests as landslides and other mass movements (Kimura *et al.* 2007a).

The present study area is the seaward edge of the Kumano forearc basin and the associated accretionary prism (Fig. 2.1). This roughly 4,000 km^2 area is located entirely within the transition zone of the accretionary wedge between 20 and 45 km from the deformation front (Kimura *et al.* 2007b). Depths vary from 1300 m along the outer ridge to 3700 m toward the trench. Notable bathymetric characteristics include numerous faults, landslides both on the basin and wedge sides of the outer ridge, and two likely subducted seamount scars (e.g., Strasser *et al.* 2009; Moore *et al.* 2013).

To accomplish the goal of understanding the characteristics of landslides in the region, we utilized newly acquired bathymetric data to identify small (less than 1 km^2) to moderate (less than 100 km^2) sized landslides. The ubiquitous nature of these identified features permits an analysis of their spatial and physical characteristics with the aim of characterizing landslides in this area in greater detail than has previously been accomplished. After a thorough analysis of the area's landslides, the same bathymetric data allow for the identification of fault structures and other sea floor features to analyze the cross-cutting relationships with landslide type, size and distribution. To validate conclusions drawn from the bathymetry, seismic cross sections (extracted from a 3D seismic volume; Moore *et al.* 2009) were employed to identify the subsurface structures controlling the location of faults and their morphology. Using both bathymetry and seismic data will aid in pinpointing any relationships between landslides and subsurface features in the area.

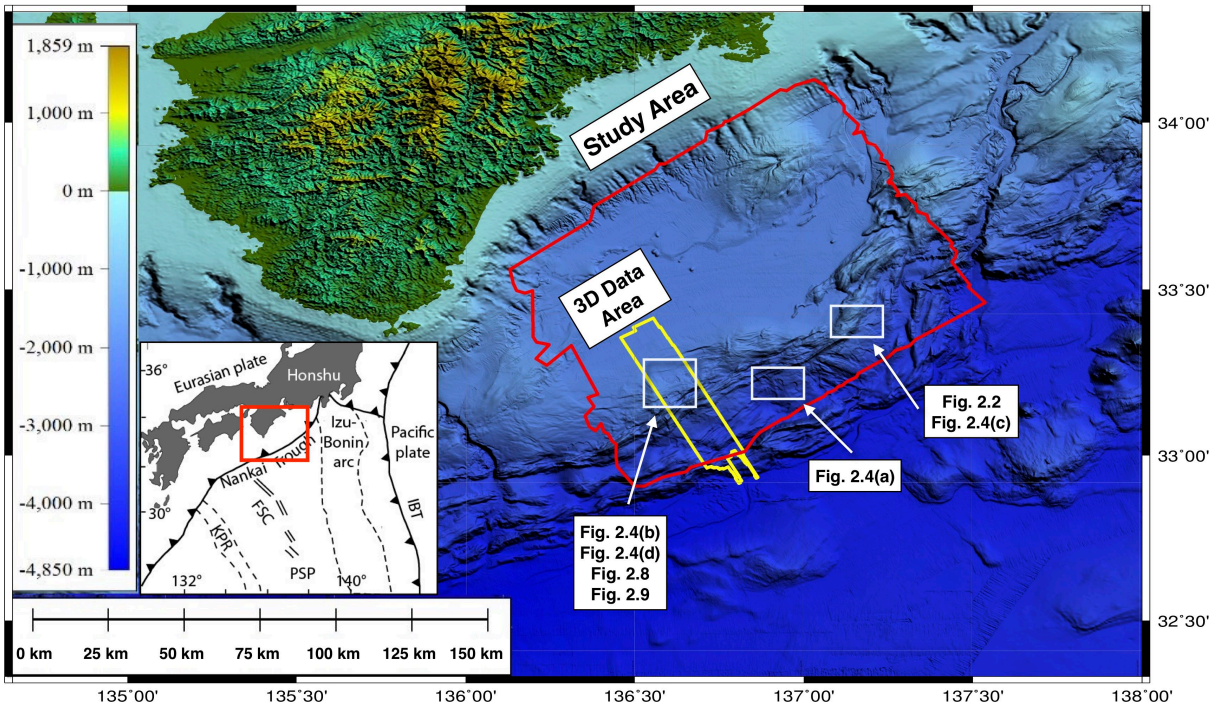

Fig. 2.1. Regional map of the study area. The location of the SO251 bathymetric data set is outlined in red while the boundary of the 3D seismic volume is outlined in yellow.

Methods

Bathymetry and acoustic backscatter data were acquired with a 0.5º × 1º Simrad EM122 multibeam system on R/V Sonne. The multibeam system was calibrated with 2 Chlorinity Temperature Depth (CTD) water column sound velocity profiles in the basin. The bathymetric data were gridded in 30m × 30m cells in latitude and longitude using MB-System 5.4 (Caress & Chayes 2008) and Generic Mapping Tools 5.1 (GMT) (Wessel *et al.* 2013) software.

The 3D survey covers roughly 12 km x 56 km extending from the Kumano Basin seaward to the frontal thrust in the dip direction. Acquisition occurred aboard the M/V *Nordic Explorer* from April 2006 to May 2006 under contract by Petroleum Geo-Services (PGS). Two sound source arrays (totaling 51 L or 3090 in^3) were utilized and fired alternately at 37.5 m shot intervals. The survey used four 4500 m long receiver cables spaced 150 m

apart with 360 receiver groups at 12.5 m spacing. This geometry yielded 8 source-receiver common midpoint (CMP) lines per sail line at 37.5 m spacing (Moore *et al.* 2009).

We used headwall scarps as the primary means of visually identifying landslides in the study area. They were easily resolved in the data set because these features can be 10's or 100's of meters high (Ward & Day 2001), typically have a characteristic inverted "U" shape that points in the downslope direction, and have slopes that generally exceed 10º (easily distinguishable from the surrounding slopes of < 6º). The extent of each slide was determined by following the sidewall scarp morphology for each slide and, where possible, by identifying the toe of the slide deposit (Fig. 2.2). Landslides were mapped manually as user-defined polygons using the Global Mapper software package.

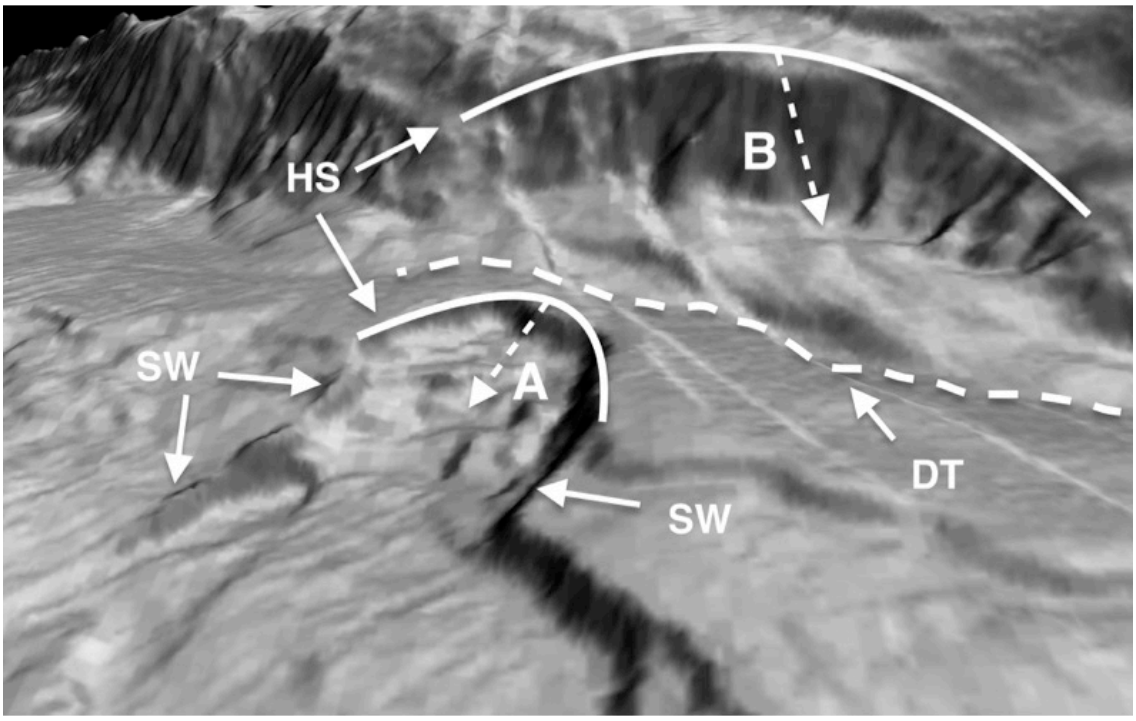

Fig. 2.2. Location shown in Figure 2.5. Two examples of morphological features used to identify landslide scars in bathymetry. Scar A is interpreted to have a fully disintegrated deposit. Scar B has a clearly visible deposit and toe. HS, headwall scarp; SW, sidewall; DT, deposit toe; dashed arrows indicate direction of slide propagation.

The following characteristics were then observed and/or calculated for each individual landslide:

(a) location as measured by the visual center of the headwall scarp recorded in decimal degrees longitude and latitude;
(b) headwall scarp height and slope angle as measured from the deepest point to the shallowest point of the headwall scarp using the Global Mapper 3D path tool;
(c) area as calculated from the area of the enclosed polygon;
(d) evacuated volume as calculated from the Global Mapper volumetric calculation tool of each enclosed polygon (Fig. 2.3);
(e) hierarchy of each slide being primary (red polygon, the initial slope failure in a given location), secondary (green polygon, occurs either downslope within the primary landslide's scar or as an upslope event that cuts across the primary landslide scar) or tertiary (blue polygon, any other landslide that cuts across secondary slides) after Katz *et al.* (2015);
(f) cross-cutting relationships with fault structures (Fig. 2.4).

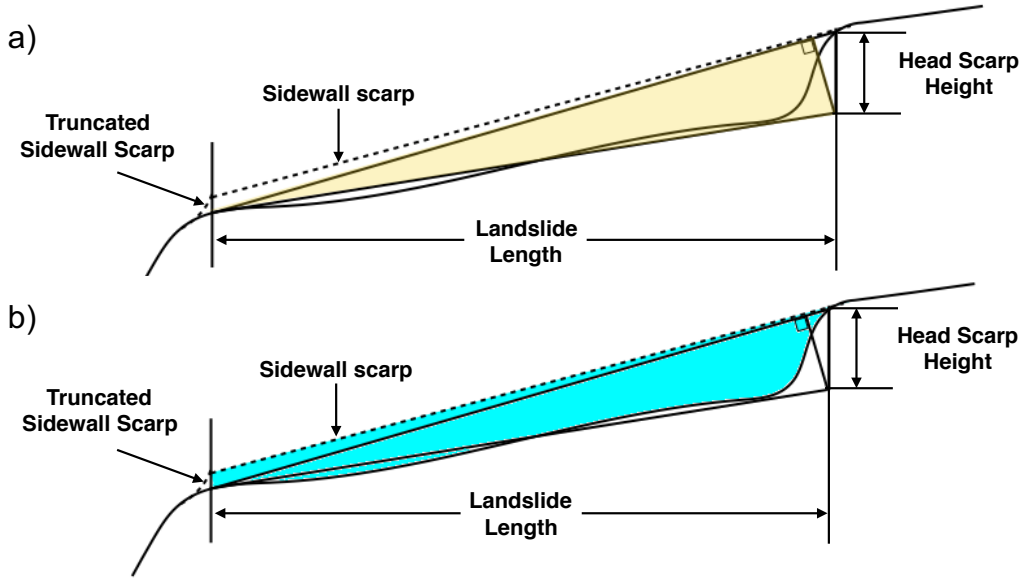

Fig. 2.3. Evacuated volume measurement method. (**a**) Adapted from McAdoo *et al.* 2000. Schematic diagram of landslide volume calculation. (**b**) Schematic diagram of the Global Mapper software's volume calculation.

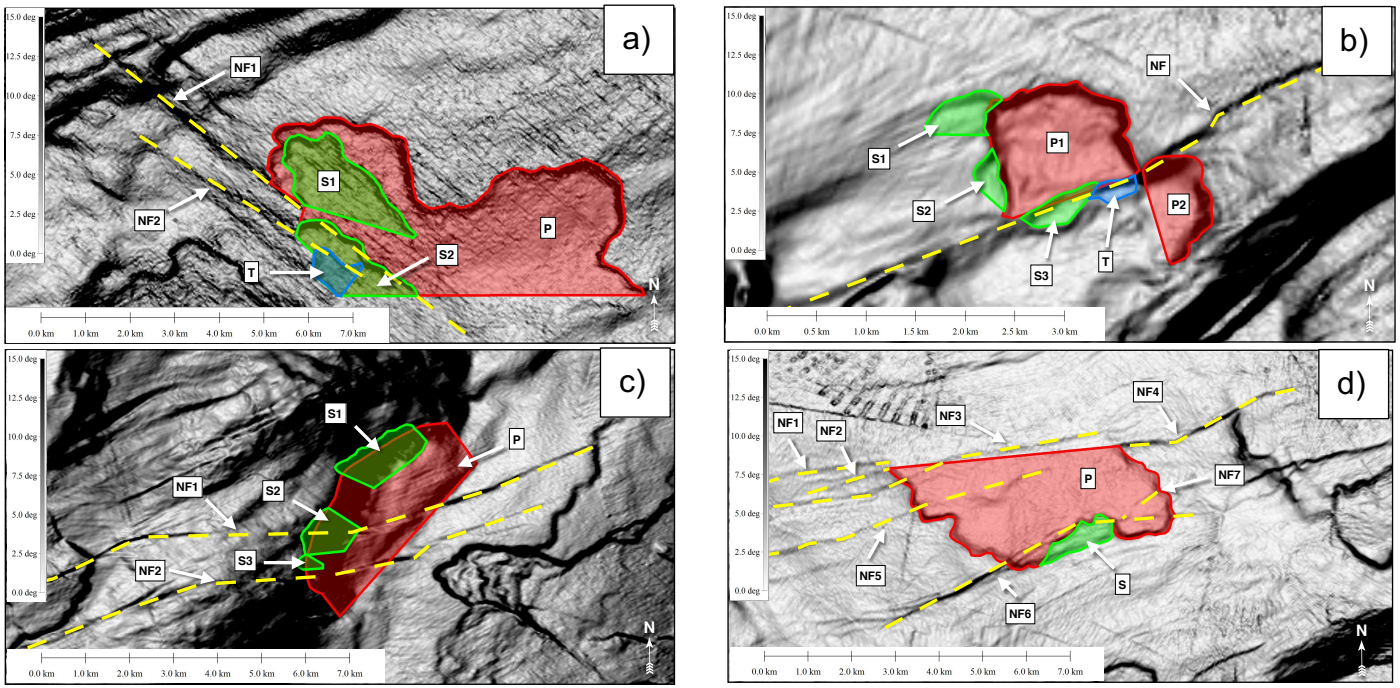

Fig. 2.4. Observed cross cutting relationships. Map view images of bathymetric data from the Global Mapper software. Image locations are indicated in Fig. 2.5. Red, green and blue polygons are primary, secondary and tertiary landslides respectively. Yellow lines indicate faults. Only faults that interact with landslides are identified in the images. (**a**) The fault is the apparent cause of the landslide. Secondary landslide 2 (S2) appears to have been caused by normal fault 1 (NF1) and the tertiary landslide (T) appears to have been caused by normal fault 2 (NF2). The primary landslide (P) displays relationship "c" with normal fault 1 (NF1) and secondary landslide 1 (S1) is part of the entire complex landslide structure. (**b**) The landslide covers the fault scarp. The deposit from primary landslide 1 (P1) covers the normal fault (NF). Primary landslide 2 (P2), secondary landslide 3 (S3) and the tertiary landslide (T) display relationship "a" with the normal fault. Secondary landslides 1 and 2 (S1, S2) are part of the entire complex landslide structure. (**c**) The fault cuts across a landslide scar. Normal fault 1 (NF1) creates a bathymetric offset across the primary landslide (P) and secondary landslide 2 (S2) while normal fault 2 (NF2) creates an offset across only the primary landslide (P). Secondary landslides 1 and 3 (S1, S3) are part of the entire complex landslide structure. (**d**) Relationships b and c apply to a single landslide. The primary landslide (P) displays relationship "b" by covering parts of normal faults 1 through 4 (NF1, NF2, NF3, NF4) and displays relationship "c" by being cut by normal faults 5 through 7 (NF5, NF6, NF7). The secondary landslide (S) displays relationship "b" by covering normal fault 6 (NF6).

The Global Mapper software calculates the volume and area for a given polygon. The points along the perimeter of the polygon are connected to create a planar surface that serves as landslide area and as the top of the volume to be calculated. Elevation data are then used to calculate the base of the volume. A similar method was successfully used by ten Brink *et al.* (2006) to measure volumes of carbonate landslides from northern Puerto Rico.

To further constrain the volume data, evacuated volumes of landslides that were part of complex structures were calculated by subtracting secondary and/or tertiary landslide evacuated volumes from the primary and/or secondary landslide. Because the evacuated volume of the initial slide would not include the evacuated volume of any subsequent slides, it is not appropriate to include this volume as measured by the Global Mapper volumetric calculation tool. This volumetric correction was required for 31 landslides resulting in a total volume correction of 0.29 km^3 or 16.2%.

The primary morphological characteristics used to identify faults are a relatively steeper slope than surrounding bathymetric features and little deviation in strike along the seafloor. To ensure the accuracy of our identification method, two lines from the 3D seismic volume are interpreted and compared to the bathymetric data. Seismic lines are interpreted landward of the outer ridge because faults in this area are more ubiquitous and uniform. This presents more opportunities to compare faults identified in bathymetry to seismically interpreted faults.

Faults were mapped manually as user defined polyline features in the Global Mapper software. A full characterization and mapping of fault structures within the study area is outside the scope of this paper and has been well documented by Kimura *et al.* (2011) & Moore *et al.* (2013). This study does, however, aim to identify seafloor fault structures that cut or are cut by landslides to aid in the determination of spatial and/or temporal relations with landslides.

Results

Morphology

Overall, we mapped and characterized 718 landslides in the study area. The total area of failed slopes covers approximately 595 km^2 with 81.6% (485 km^2) of the failed slope area occurring seaward of the outer ridge, as would be expected in an accretionary environment. Landslides ranged in depth from 1308 meters below sea level (mbsl) at the highest observed headwall scarp to 3615 m at the lowest observed headwall scarp. The largest single failed slope is 86.2 km^2 while the smallest measured failed slope is 4.7 x 10^{-3} km^2. Headwall scarps ranged in height and slope angle from 6.2 m to 660.4 m and 4.5º to 33.1º with mean values of 68.1 m and 16.9º respectively. Primary landslides account for 61.5% (442) of the total number mapped while secondary landslides account for 25.6% (184) and tertiary landslides for 12.8% (92). Following the categorization of Katz *et al.* (2015), landslides displayed either a "simple" or "complex" overall structure. Simple landslides are defined as single events that result from a single slope failure whereas complex landslides result from a hierarchal pattern of multiple sequential slope failures over time. Of those observed, 44% (317) of the landslides are categorized as simple while the remaining 56% (401) are part of 81 separate complex structures.

Size and Distribution

Across the entire study area, the majority of observed landslides, 64%, occur seaward of the outer ridge (Fig. 2.5). Landslides range in surface area from roughly 4.7 x 10^{-3} km^2 being the smallest measured to 86.2 km^2 being the largest measured. The footprint of the bathymetric data is 9 x 10^{-4} km^2, indicating that the methodology used to create the inventory of identified landslides is complete and comprehensive. The mean area for all landslides is 0.83 km^2 while the median is 0.16 km^2. The large difference between these two values is indicative of a distribution that is positively skewed toward larger area values. Of the 718 landslides, only 94 (13%) were larger than 1 km^2 accounting for 458 of the 595 km^2 (77%) of failed slope area. Because of the skewed nature of the data, the median is the more accurate representation of the central tendency (Fig. 2.6). The evacuated volume of landslides has a mean of 1.9 x 10^{-2} km^3 with a median of 9.7 x 10^{-4} km^3. Here again, the median is the more accurate central tendency representation

because of the data exhibiting a skewed distribution. The most and least volumetric evacuations were 3.77 km^3 and 4.0 x 10^{-6} km^3 respectively, further demonstrating the wide range of landslides in the study area (Fig. 2.6).

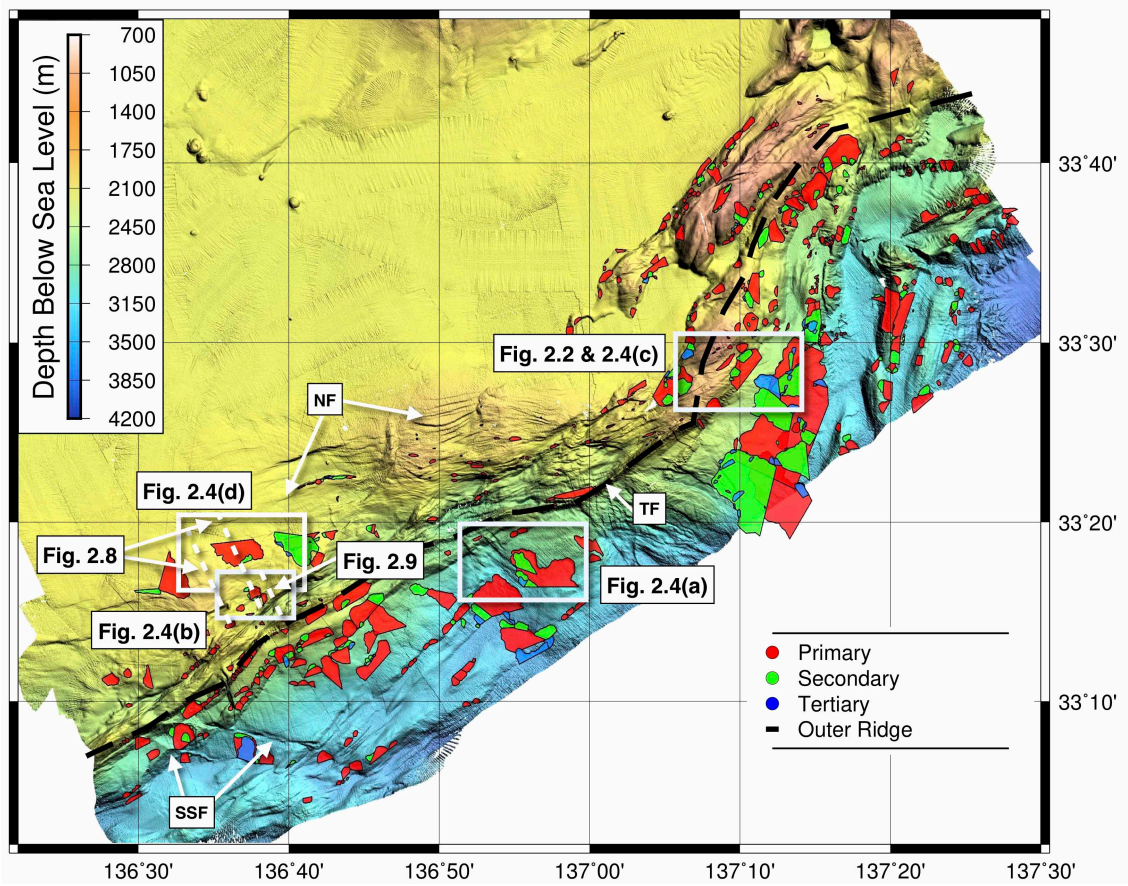

Fig. 2.5. Landslide locations. Polygons represent manually mapped landslide areas. Dashed lines are seismic line locations used in Fig. 2.8 & 2.9. SSF, strike-slip fault; NF, normal fault; TF, thrust fault. Generated using the Generic Mapping Tool (Wessel *et al.* 2013).

It is important to note the most likely sources of error for these measurements. Geomorphic landslide parameter measurement errors increase with increasing area, volume, and hierarchal complexity of the landslide(s) due to a higher degree of difficulty in determining the slide boundaries. While the headwall and sidewall scarps of a slide scar more readily remain visible in the bathymetry throughout sediment deposition, the scar itself infills with new sediment, causing the measured volume to be less than the actual volume. Additionally, it is likely that the top layers of sediment (10s to 100s of cm)

have been remobilized many times because of seismic activity (Ashi *et al.* 2014). Redistributing surficial sediment across scarps can alter their surface morphology and bring about inaccuracies in area and volumetric measurements.

The full area of many landslides was unmeasurable as no deposit or only partial deposits were present. Of the 718 identified landslides, only 192 had full or partial deposits (66 and 136 respectively) indicating that landslide deposits in this region are largely fully disintegrative. For this reason, the majority of area measurements were made from the headwall scarp to the furthest observable sidewall scarps (Fig. 2.3). Fault structures that cross cut slide scars also increase the complexity and difficulty in making accurate measurements. Both the evacuated volume and area are geometrically distorted as a result of the fault's interaction with the slide scar and, in most cases, cannot be fully accounted for in the measurements.

To further constrain the volume data, evacuated volumes of landslides that were part of complex structures were calculated by subtracting secondary and/or tertiary landslide evacuated volumes from the primary and/or secondary landslide. Because the evacuated volume of the initial slide would not include the evacuated volume of any subsequent slides, it is not appropriate to include this volume as measured by the Global Mapper volumetric calculation tool. This volumetric correction was required for 31 landslides resulting in a total volume correction of 0.29 km^3 or 16.2%.

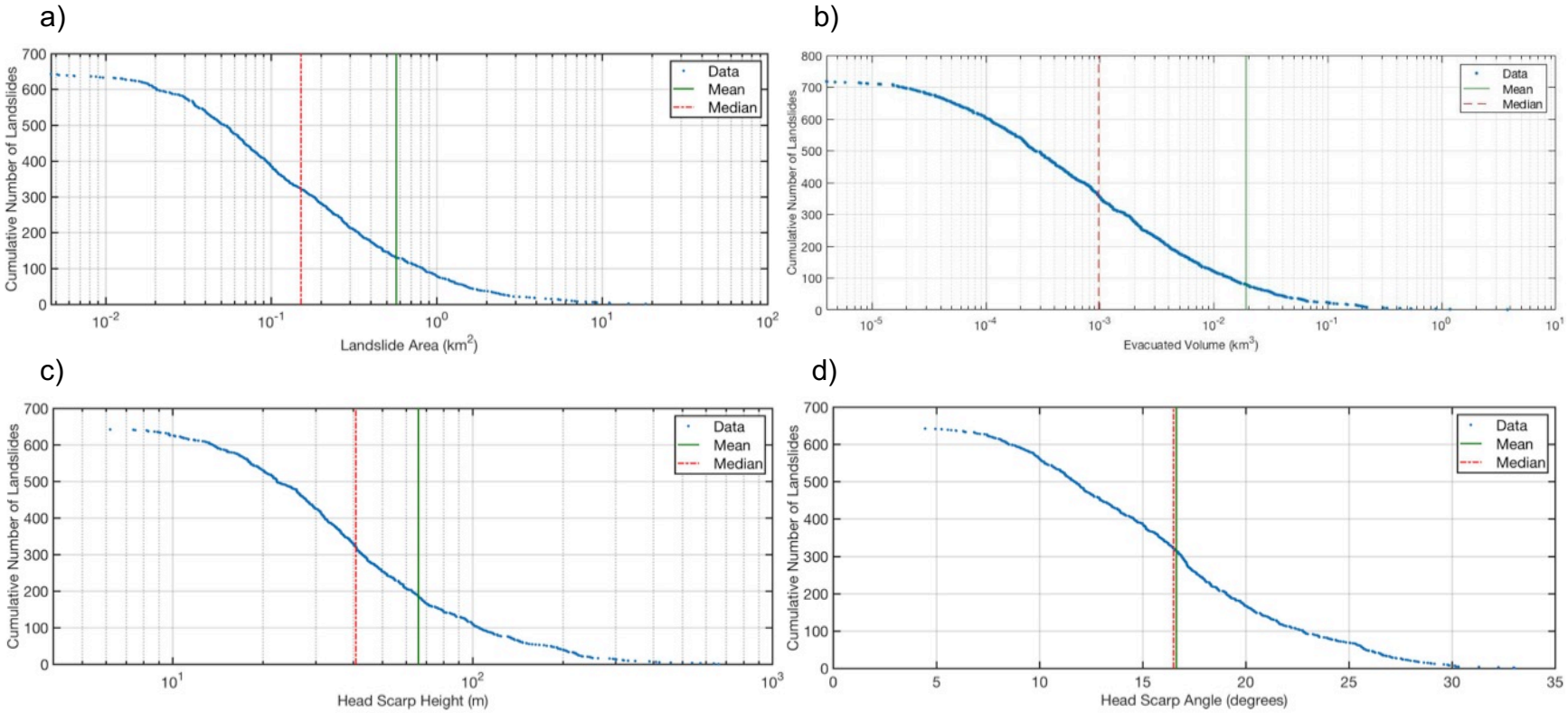

Fig. 2.6. Log plots of landslide characteristics. (**a**) Plot of landslide area versus cumulative number of landslides. (**b**) Plot of landslide evacuated volume versus cumulative number of landslides. (**c**) Plot of head scarp height versus cumulative number of landslides. (**d**) Plot of head scarp angle versus cumulative number of landslides.

Morphological Relationships

Once a high confidence in area and volumetric measure was achieved for all landslides, it was found that 542 (75.5%) are smaller than 0.5 km^2 and 594 (82.7%) are smaller than 0.01 km^3 respectively. Head scarp heights are less than 100 m for 593 (82.6%) landslides and head scarp slope angles are less than 20º for 518 (72.1%) landslides (Fig. 2.6). The primary statistical correlation is between landslide area and evacuated volume (correlation coefficient of 0.96). Outside of a very weak correlation between head scarp height and head scarp slope angle (correlation coefficient of 0.55), no statistical correlation exists between head scarp height and any other measured parameter. Also, there are no other correlations between head scarp slope angle and any other measured parameter. Based on this and the observed locations of landslides with large head scarp heights, we believe head scarp height to be a function of landslide location on the accretionary prism (i.e. proximity to thrust fault scarps).

As with other large submarine landslide inventories (ten Brink *et al.* 2006; Urgeles & Camerlenghi 2013; Katz *et al.* 2015) we found that the population characteristics fit a power law relationship within certain bounds. Landslide volume fits to a power law behavior for volumes greater than 0.019 km^3. Below this volume the population tends to exhibit a logarithmic behavior, although not as strongly (Fig. 2.7). Landslide area also exhibits a power law behavior for areas greater than 0.9 km^2 and a more characteristic logarithmic behavior for areas small than this (Fig. 2.7). The logarithmic behavior of these characteristics is interesting when compared to other inventories. ten Brink *et al.* (2006) and Urgeles & Camerlenghi (2013) both attribute the “roll over” (point at which population behavior changes) in the data to a likely under sampling of smaller landslides due to bathymetric resolution limitations. Due to the comprehensive nature of this study regarding smaller landslides it appears that the “roll over” is more likely due to geological influences than sampling constraints. The differences in power law exponents between studies is also likely due to the geological setting of each data set (active and passive margins, deltas, etc.), however investigating these differences further is outside the scope of this study.

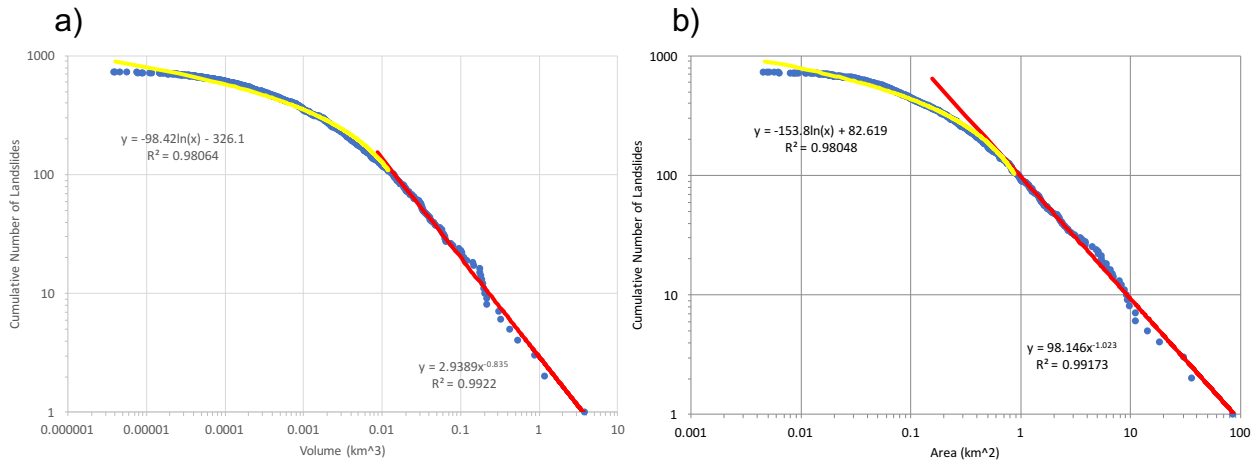

Fig. 2.7. Loglog plots of landslide characteristics showing power law and logarithmic behaviors. (**a**) Plot of landslide volume versus cumulative number of landslides. (**b**) Plot of landslide area versus cumulative number of landslides.

Faults

We distinguish three primary groups of faults in the data. Normal faults are found primarily on the basin side of the accretionary prism and within the subducted seamount scar. Thrust faults are located along the seaward side and at the apex of the accretionary wedge (e.g., Moore *et al.* 2009; Strasser *et al.* 2009; Kimura *et al.* 2011). We also identified a few strike-slip faults along a second inferred subducted seamount scar. While the study of the seamount scars is outside the scope of this paper, it is important to recognize the faults that can occur because of these subduction events. Sand box experiments have shown that a subducting bathymetric high creates a variety of fault structures dependent upon the high's general morphology (Dominguez *et al.* 1998). All three fault types are present indicating a likely source of cross-cutting relationships and/or slope failure causal mechanisms for the present study.

Faults are found to traverse predominantly along strike of the accretionary wedge. There are three instances of faults identified in bathymetry that are not interpreted in the seismic data (Fig. 2.8). Fault 2 is not interpreted in seismic line 2390. However, the fault appears in seismic lines 2411 to 2440 (Fig. 2.9) indicating one of two likely scenarios: either the user drawn polyline feature is incorrectly drawn (too long) or the fault has been eroded

due to landslide processes. Faults 1 and 3 are either bathymetric misidentifications or are newly developed faults that manifested between the acquisition of the 3D seismic volume (2006) and the bathymetric data (2016). Verification of our method results in accurately identifying a fault more than 90% of the time using bathymetric data alone, thus placing a high level of confidence in our method.

Cross-cutting Relationships

Numerous instances of faults and landslides spatially overlapping and interacting occur within in the study area. Examples of interaction are found on both sides of the outer ridge between normal faults and landslides and between thrust faults and landslides. We did not identify interaction between strike-slip faults and landslides, although this could be due to the limited occurrence of strike-slip faulting in the study area or to the difficulty in identifying the strike-slip component of displacement in seismic section.

Of the 718 landslides mapped, 80 have a cross-cutting relationship with a fault. Interactions between faults and landslides are divided into 4 categories based on their cross-cutting relationships (e.g., Katz *et al.* 2015):

(a) a mechanical relationship in which the fault predates the landslide as evidenced by the fault being the apparent cause of the landslide (Fig. 2.4(**a**));
(b) a non-mechanical relationship in which the fault predates the landslide as evidenced bythe landslide covering or cutting the fault scarp (Fig. 2.4(**b**));
(c) a second non-mechanical relationship in which a fault postdates a landslide as evidenced by the fault cutting across a landslide scar or deposit (Fig. 2.4(**c**));
(d) a case in which more than one of the above relationships appear to apply to a single landslide (Fig. 2.4(**d**)).

Utilizing this scheme, we mapped 17 mechanical relationships (a), 31 instances of slides covering faults (b), 17 instances of faults cross-cutting slide scars or deposits (c) and 13 instances of coexisting relationships (d).

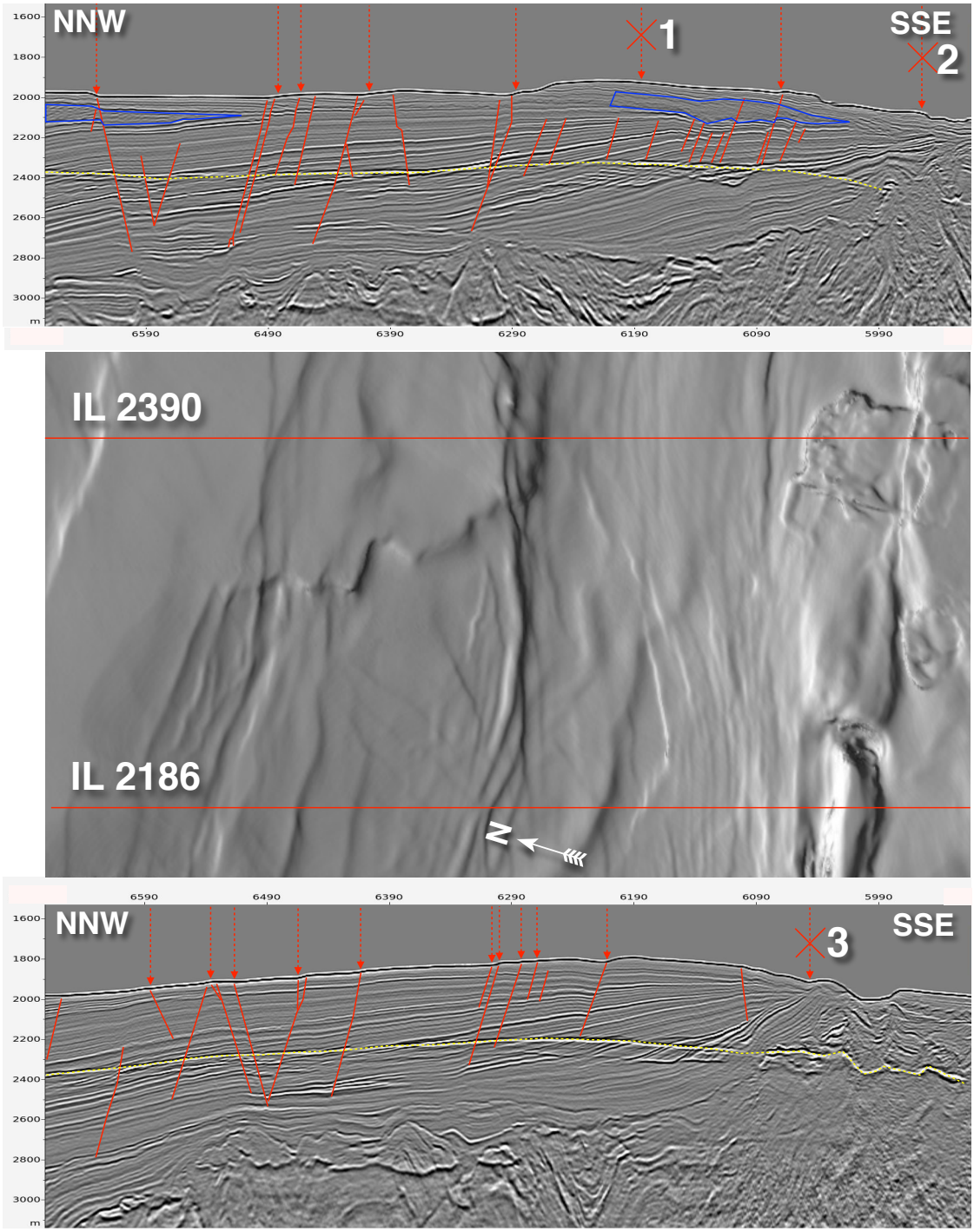

Fig. 2.8. Seismic lines and bathymetry extracted from 3D volume. The top seismic image is Inline 2390 and the bottom seismic image is inline 2186. Red dashed arrows indicate locations of faults identified using bathymetric data, red dashed arrows with "X's" are possible bathymetric misidentifications, red lines indicate fault plane reflectors, yellow lines indicate bottom simulating reflectors, and blue areas are previously identified mass transport deposits identified by Moore & Strasser (2016). The red lines across the bathymetry indicate the location and extent of the seismic lines.

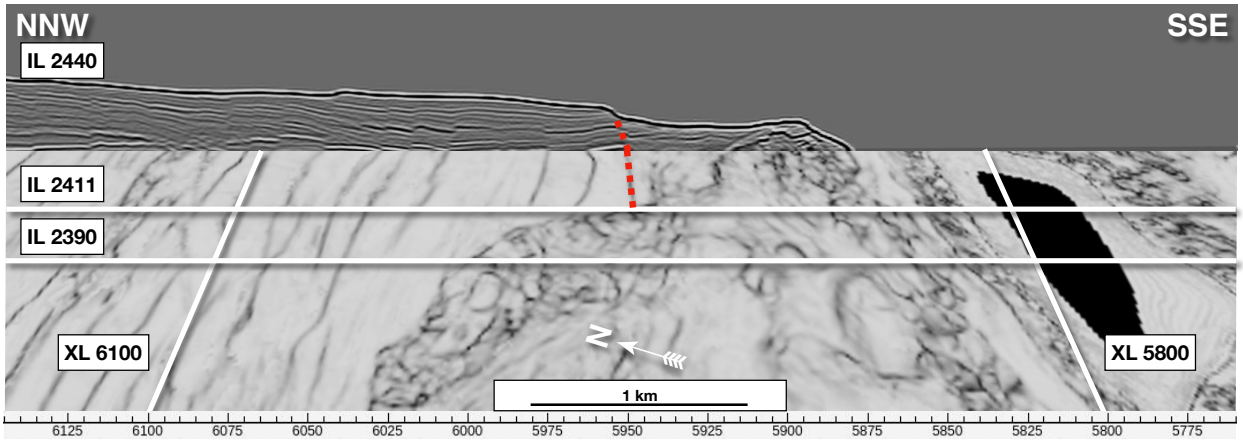

Fig. 2.9. Coherency depth slice 2148. The depth slice is taken 100 mbsf at the location of fault "2" in Fig. 2.8. The seismic image is inline 2440. Red dashed lines indicate a fault while white lines indicate inline and cross line locations for reference.

Discussion

The areal distribution of cross-cutting relationships helps to constrain likely trigger mechanisms to sliding. Of the 80 observed relationships, 60 are found in the western area of the study area (19 seaward and 41 landward of the outer ridge) while only 20 are in the eastern half (10 seaward and 10 landward of the outer ridge). Additionally, areas where faulting causes landslides (relationship "a") occur primarily seaward of the outer ridge (12 of 17, or 71%), and areas where slides cover or cut faults scarps (relationship "b") occur primarily landward of the outer ridge (27 of 31, or 87%) while faults cutting slides (relationships "c" and "d") are evenly distributed throughout the study area. This distribution indicates that faulting is more likely to be a trigger for landslide initiation seaward of the outer ridge where thrust faulting tends to dominate. While fault triggered landslides are not absent landward of the outer ridge, they appear to be far less common (17 of 80, or 21%) indicating that there are other trigger mechanisms at work in the Kumano Basin.

The constant supply of terrigenous sediment could precondition slopes for failure. Although sedimentary strata vary along and across strike of the entirety of the accretionary prism, the 78 to 207 m thick slope apron deposited on the Kumano section largely consists of interbedded hemipelagic mud, volcanic ash, and silt and silty sand

turbidites as identified in various cores throughout the region (Kimura *et al.* 2011; Strasser *et al.* 2011; Underwood & Moore 2012). The mud contains increasing concentrations of calcareous nanofossils up stratigraphic section, indicating tectonic activity causing uplift above the carbonate compensation depth (Underwood *et al.* 2003). Pore fluids entrained within the turbidite layers may have become trapped between mud layers during diagenesis. The trapped fluids would increase poor pressures locally potentially creating a mechanically weak failure plane. During wedge growth, this failure plane can be activated via many mechanisms including slope over-steepening or seismic loading (Ikari *et al.* 2011).

Methane gas and hydrates (frozen gas) exist along most continental margins (Milkov 2004). These reservoirs have been hypothesized to be metastable with minor changes in temperature and/or pressure initiating methane venting or hydrate dissociation (Westbrook *et al.* 2009). This venting and dissociation can lead to seafloor mobilization or failure. Strong bottom currents, often found in combination with strong surface currents (Holbrook *et al.* 2002) such as the Kuroshio Current, can erode 10's of meters of sediment thereby changing the temperature-pressure conditions at a particular site. If the conditions change enough, free methane gas venting or hydrate dissociation from within the underlying strata could initiate landsliding locally or on kilometer scale sections of the seafloor (Westbrook *et al.* 2009; Bangs *et al.* 2010). Bangs *et al.* (2010) have hypothesized this to be the case in a large section of the Nankai accretionary prism and is therefore likely to be both a preconditioning factor and trigger mechanism of landsliding throughout the study area (Kremer *et al.* 2017).

The Nankai region has a well-documented and regular history of small and great earthquake activity (Ando 1975; Kimura *et al.* 2011; Moore *et al.* 2013). Great earthquakes along the margin, which has been in motion since 6 Ma (Saffer *et al.* 2010), are documented as far back as 648 AD with a recurrence interval of 100 to 200 years (Ando 1975). If a splay fault, such as the Nankai megasplay, ruptures co-seismically, amplification of seismic ground shaking can occur within the hanging wall (Abrahamson & Somerville 1996). This has been suggested for Nankai and other splay fault systems

(e.g., Plafker 1972; Tanioka & Satake 2001; Baba *et al.* 2006), thereby representing a plausible causal link between seismic loading and slope failure. However, as noted by Moore & Strasser (2016) the recurrence interval for landsliding in the Kumano Basin appears to be on the order of 0.05 to 0.1 Ma, which is much less frequent than the recurrence interval for Nankai's great earthquakes. This implies that seismic loading, while a possible ultimate trigger for landsliding, likely requires a slope to be pre-conditioned to fail before failure actually takes place as also suggested by Strasser *et al.* (2012) and Kremer *et al.* (2017) seaward of the Kumano Basin.

An actively deforming accretionary prism combined with mechanically weak sediment layers suggests that the primary triggering mechanism is either slope over-steepening due to the formation of anticlinal structures or seismic loading that triggers failure within weak layers. However, it is important to note that the slopes are likely preconditioned for failure regardless of final triggering mechanism for various reasons such as interactions with fault structures (as evidenced by this study), bottom current activity, lithology, and gas hydrate dissociation (Westbrook *et al.* 2009; Bangs *et al.* 2010; Underwood & Moore 2012; Moore & Strasser 2016; Kremer *et al.* 2017).

Conclusions

As evidenced by a high occurrence? of unique morphological structures, landslides and faults are ubiquitous phenomena on the accretionary prism of the Nankai Trough of SW Japan. While the 718 observed landslides are widespread throughout the study region, many of them occur in complex structures involving multiple temporally sequential landslides seaward of the outer ridge on the actively deforming transition zone of the accretionary prism. Faults tend to strike along the accretionary prism (WSW to ENE) and, while not found to be a primary triggering mechanism, appears to play a role in the preconditioning of various slopes for failure. Additionally, methane gas and hydrates, pore fluid overpressures, and bottom current activity all are likely factors that precondition slopes in the study area for failure. Seismic loading and slope over-steepening are then the most likely final trigger mechanisms to slope failure.

Acknowledgements

The new bathymetric compilation was made possible by the hard work of the SO251 Hydroacoustic Group (K. Bachmann, K. Lange, J. Moernaut). We thank Paradigm Geophysical and Blue Marble Geographics for making their software available to us. SOEST Contribution # 10028.

CHAPTER 3
THREE-DIMENSIONAL MAPPING AND KINEMATIC CHARACTERIZATION OF MASS TRANSPORT DEPOSITS ALONG THE OUTER KUMANO BASIN AND NANKAI ACCRETIONARY WEDGE, SOUTHWEST JAPAN

This chapter has been published as: Lackey JK, Moore GF, Strasser M (2018) Three-dimensional Mapping and Kinematic Characterization of Mass Transport Deposits Along the Outer Kumano Basin and Nankai Accretionary Wedge, Southwest Japan. Prog. Earth Planet. Sci., Special Issue, v. 5/65.

Abstract

Three-dimensional (3D) seismic data from the southern Kumano Basin of southwest Japan image a nested series of moderately sized mass transport deposits (MTDs) that slid from a slope along the seaward side of the forearc basin. The deposits are dated to be approximately 0.3 to 0.9 Ma. These MTDs are likely linked to the movement along a prominent out-of-sequence thrust (OOST) fault, regionally steeper slopes that would have existed during deposition, and shifts in sedimentation over the past 0.9 Ma. The spatial resolution provided by the 3D seismic data permits the identification of kinematic characteristics and the internal geometries of the MTDs which total over 2.8 km^3 in volume and cover more than 59 km^2 of the seafloor at various stratigraphic levels. Each MTD is well imaged and exhibits various kinematic indicators while most of the basal glide planes and original headwall scarps above the deposits have been partially or fully eroded by subsequent MTDs. There are at least seven individual deposits that range in volume from 0.005 to 1.16 km^3, in area from 0.2 to 21.8 km^2; have runouts between 0.55 and 7.9 km, and generally translate downslope from the SE to NW. Basal, internal, and top surface kinematic indicators, such as grooves, thrust and fold systems, and pressure ridges, show that these MTDs originate from a prominent slide scar recognized in the high-resolution regional bathymetry. This, combined with a regionally shifting depocenter and faulting

related to the earthquake cycle, points to regional tectonic activity as being the most likely failure trigger for these nested landslides.

Introduction

Subaqueous landslides occur in many different environments all over the world including both active and passive margins, along the flanks of volcanic islands, and river deltas (Prior and Coleman 1978; Moore *et al.* 1989; Lee 2009) and can occur on a great variety of slopes (ranging from < 0.01º to vertical (Prior and Coleman 1978)). These slides can be devastating to seafloor infrastructure via high speed turbidity currents and to coastal communities in the form of tsunami (Bondevik *et al.* 1997; Bardet *et al.* 2003; Satake 2012). Characterization by their size, shape, and kinematics allows us to better understand how they initiate and translate downslope to the point at which they arrest (Ward and Day 2002).

The movement of the failed mass from the source of failure to the point of arrestment can be analyzed and described using kinematic indicators present in either seismic data (Prior *et al.* 1984; Bøe *et al.* 2000; Gee *et al.* 2005, 2006) or outcrops (Farrell 1984; Lucente and Pini 2003; Matheus *et al.* 2017). In a general sense, kinematics describes the motion of bodies without the consideration of the body's mass or forces that caused its motion. Here, we follow Bull *et al.* (2009) in defining "kinematic indicator" as a geologic structure or feature which records information related to the type and direction of motion at the time of emplacement. This information is of great use in helping us understand the motions involved with slide initiation, evolution during translation downslope, and cessation. Additionally, because of the complex nature of submarine landsliding, many variably active processes are likely involved in each mass movement. This leads to a litany of potential classifications and terminology. Here we chose to simplify the classification of deposits from various mass movements identified in the data as simply "mass transport deposits" (MTD).

This study represents a unique opportunity to analyze several Quaternary MTDs via a 3D seismic reflection survey in the Kumano Basin along the Nankai accretionary prism.

Some of these MTDs were previously identified by Moore and Strasser (2016), however, no kinematic analysis was performed nor was a reconstruction of the original slope attempted. Because they are fully imaged in the 3D survey, a complete analysis of kinematic indicators and morphology is possible. A kinematic analysis of these MTDs should provide greater insight into the depositional environment in which sliding occurred and determine a possible explanation as to the origin of a prominent seafloor scar (Lackey *et al.* 2018a).

Regional Setting and Study Area

The Kumano Basin is within the Nankai Trough subduction zone where the Philippine Sea Plate is presently subducting under the Amur Plate at a rate of 4 to 6 cm yr^{-1} (Seno *1989*). The NW oblique subduction has led to the creation of an accretionary prism spanning roughly 700 km, with the overall oblique slip being apportioned along a large right lateral strike-slip fault, known as the Median Tectonic Line, landward of the prism (Fitch 1972; Taira 2001). The accreted sediment is primarily terrigenous detritus from Honshu arc, Japan and hemipelagic deposits on the Philippine Sea Plate (Underwood and Moore 2012). The upper part of the hemipelagic section from the Philippine Sea Plate is accreted while the lower part is subducted beyond the inner prism (e.g., Kinoshita *et al.* 2009; Kimura *et al.* 2011; Strasser *et al.* 2011; Strasser *et al.* 2012; Underwood and Moore 2012; Moore *et al.* 2014). The inner prism is overlain by the Kumano forearc basin which has formed over approximately the past 1.95 to 2.0 Ma behind the outer ridge that is believed to be the result of movement along the mega-splay fault (Gulick *et al.* 2010; Moore *et al.* 2015). The seismic recurrence interval of roughly 100 to 200 years for large earthquakes has been well established for Nankai (Ando 1975). The rapid growth of the accretionary prism is an important factor for large, repeated earthquakes in this subduction zone setting (Ruff and Kanamori 1980).

The present study area is within the Kumano forearc basin just landward of the outer ridge of the accretionary prism (Fig. 3.1). The 3D seismic data used for this study covers roughly 275 km^2 (Moore and Strasser 2016) and is located entirely within the transition zone of the accretionary prism between 35 and 50 km from the deformation front (Kimura

et al. 2007). Seafloor depths vary from 1700 m seaward of the study area to 2100 m landward. Notable characteristics include numerous faults in both the 3D data and bathymetry, temporally sequential landslide scars, and an absence of surficial landslide deposits (e.g., Strasser *et al.* 2009; Moore *et al.* 2013; Lackey *et al.* 2018a).

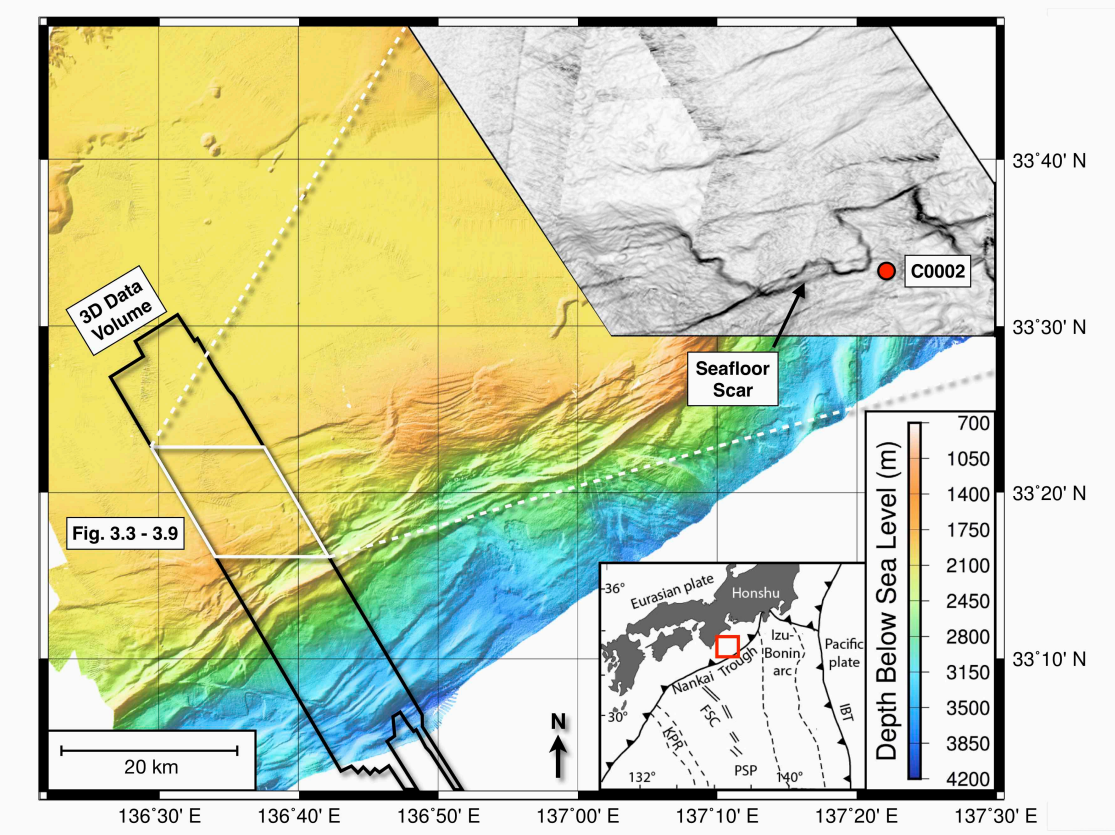

Fig. 3.1. Study Area. High resolution bathymetry of the Kumano Basin acquired by R/V *Sonne* during Cruise SO251 in 2016 (Strasser *et al.* 2017). Trapezoidal inset shows a slope gradient map of a prominent seafloor scar from Lackey *et al.* (2018) and the location of IODP drill site C0002.

Methods

To identify MTDs and kinematic indicators, we interpreted several prominent horizons throughout our 3D seismic survey, including basal shear surfaces (BSS), tops of MTDs, and various depositional layers. Amplitude and coherency data are then displayed on these horizons to highlight geomorphic structures and kinematic indicators with the goal of reconstructing the various MTDs to their original positions. To validate conclusions drawn from the data, we compare our results to other subaqueous landslide kinematic

studies (e.g. Frey Martinez *et al.* 2005, 2006; Gee *et al.* 2005, 2006; Bull *et al.* 2009; Moore and Strasser 2016) that utilize 3D seismic reflection data.

3D Volume

The full 3D survey covers roughly 12 km x 56 km extending from the Kumano Basin seaward to the frontal thrust in the dip direction (Fig. 3.1). Acquisition occurred aboard the M/V *Nordic Explorer* during April-May 2006 under contract by Petroleum Geo-Services (PGS). Two sound source arrays (totaling 51 L or 3090 in^3) were utilized and fired alternately at 37.5 m shot intervals. The survey used four 4500 m long receiver cables spaced 150 m apart with 360 receiver groups at 12.5 m spacing. This geometry yielded eight source-receiver common midpoint (CMP) lines per sail line at 37.5 m spacing (Moore *et al.* 2009). The interval between lines and cross lines of the resulting dataset is 18.75 m and 12.5 m, respectively. The vertical resolution is ~5-7 m near the seafloor, degrading to ~10-20 m at depths near 1400 meters below seafloor (mbsf; Moore *et al.* 2009). Standard pre-processing to reduce noise preceded pre-stack depth migration (PSDM) and produced a clear seismic image in depth (Moore *et al.* 2009). For the seaward part of our area, we were able to use a reprocessed version of the 3D data set that produced much higher-resolution images of the sedimentary section (Shiraishi *et al.*, in review).

Bathymetry Data

High resolution bathymetry data analyzed for surficial MTDs has been acquired during R/V *Sonne* Expedition 251 in October 2016 (Strasser *et al.* 2017). The R/V *Sonne* is equipped with an EM 122 KONGSBERG multibeam echosounder (MBES) operated at 12 kHz. The transducers have a nominal opening of 0.5° in along-track direction and 1° in across track direction. The MBES recorded 433 individual beams across track within a swath of 120°. Actual sound velocity profiles were recorded with the ships CTD and inserted as basis for optimized performance. Data were processed with software MB-System (Caress and Chayes, 1996).

Core Data

Coring of the Kumano Basin sediments was accomplished on Integrated Ocean Drilling Program (IODP) Expeditions 315 (Kinoshita *et al.* 2009) and 338 (Strasser *et al.* 2014) (Fig. 3.1). The cored interval consists of hemipelagic mud and numerous thin interbeds of normally graded silt, sandy silt and sand with local layers of volcanic ash (Underwood and Moore 2012). For a more detailed analysis of the core data see Underwood and Moore (2012). These data demonstrate that nearly all the basin fill accumulated within the last 1.6 Ma.

MTD Recognition and Kinematic indicators

MTDs are typically identified by their internal chaotic reflection character or semitransparent to transparent seismic character. Once an MTD is identified, other seismic indicators (e.g., hummocky reflections, truncations of stratigraphic layers, folds and thrusts) are used to characterize the remainder of the MTD. For the purposes of this study, we subdivide each MTD into three domains based on which kinematic indicators are most likely to occur in a typical "tripartite" MTD anatomy (Martinsen 1994; Lastras *et al.* 2002): the headwall, translational, and toe domains (Fig. 3.2). While there is almost always overlap between these domains, it is important to have a clear delineation between them to properly study kinematic indicators in the data.

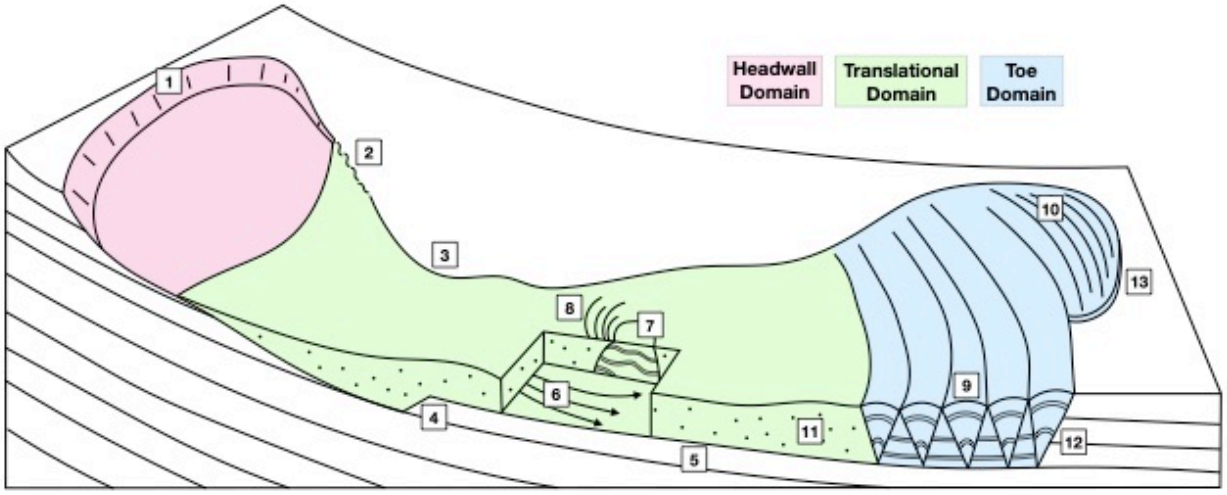

Fig. 3.2. Key geometric and geologic criteria for kinematic indicator recognition. 1 – Headwall scarp. Direction of initial movement roughly perpendicular to the headwall propagation. 2 – En-echelon sigmoidal segments. Strike-slip affected MTD material differentiates lateral margin from headwall scarp. 3 – Lateral margins. Delimits strike-parallel extent of MTD and constrains gross general transport direction. 4 – Ramp. Location(s) where the BSS jumps to a higher stratigraphic level. 5 – Flat. Location(s) where the BSS is parallel with local stratigraphy. 6 – Grooves. Implies debris flow processes with translation parallel to their trend. 7 – Translated block. Often align long-axis downslope. 8 – Secondary flow fabric. Translation direction indicated by trend of flow parallel banding. 9 – Pop-up blocks. Typically 100's of meters high, translation perpendicular to alignment of ridges. 10 – Pressure ridges. Typically 10's of meters high, translation perpendicular to the strike of thrust faults. 11 – MTD matrix. 12 – Frontally confined toe. 13 – Frontally emergent toe. BSS – Basal shear surface. MTD – Mass Transport deposit. Modified after Bull *et al.* (2009).

Headwall Domain

The two prominent kinematic indicators in this region are headwall scarps and extensional ridges and blocks that represent the extensional, up-slope portion of the MTD (Bull *et al.* 2009). Crown cracks may also develop upslope of the primary headwall scarp (Fig. 3.2).

Translational Domain

The translational domain is defined as the main body of failed material that has moved downslope. It is subdivided into four sections based on their differing physical parameters: lateral margins, basal shear surface, internal MTD body, and top MTD surface (Martinsen 1994; Frey Martinez *et al.* 2005; Bull *et al.* 2009).

Toe Domain

Characterized by an overall convex-downslope morphology, the toe domain represents the region of downslope termination of the main MTD body and is characterized by thrust and fold systems and pressure ridges (Prior *et al.* 1984; Frey Martinez *et al.* 2005). Frontally confined MTDs are those where the toe domain exhibits impressive thrust and fold systems that are buttressed against stratigraphically equivalent undisturbed strata downslope while frontally emergent MTDs are able to ramp up from the original basal shear surface and translate freely across the seafloor (Frey Martinez *et al.* 2006) (Fig. 3.3).

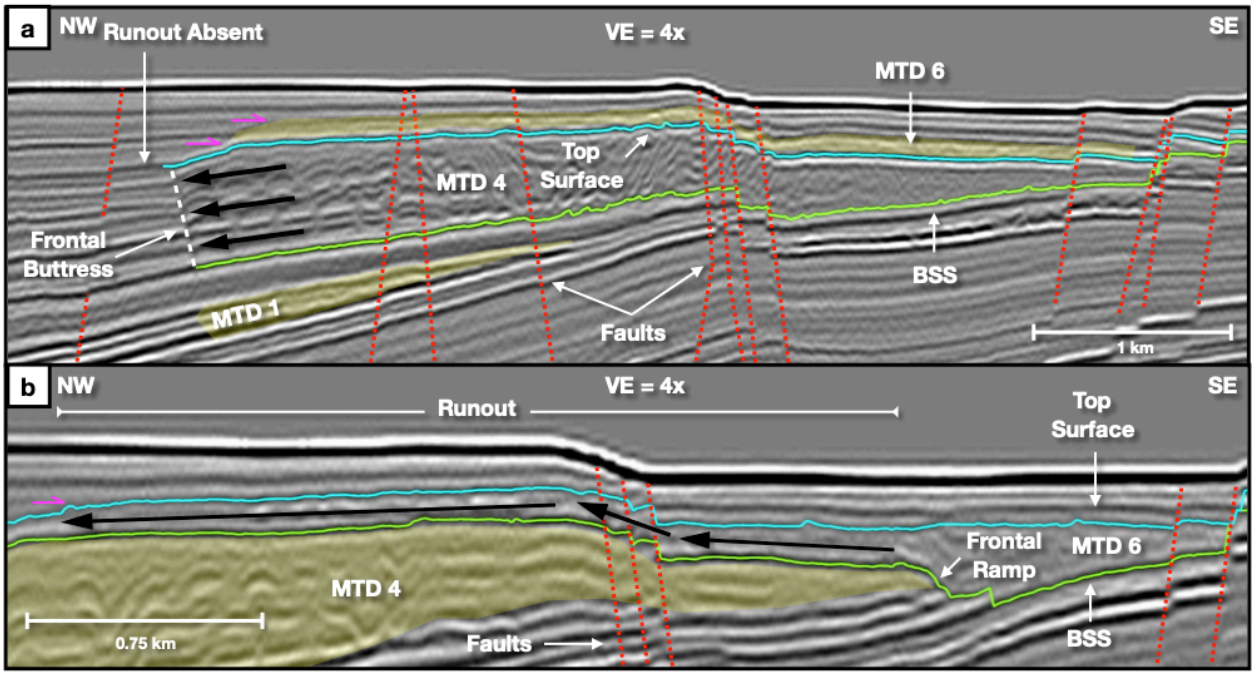

Fig 3.3. Frontally confined vs. frontally emergent MTDs. Black arrows indicate primary translation direction. Purple arrows indicate on-lapping relationships. BSS - Basal Shear Surface. (**a)** Frontally confined landslide. Arbitrary seismic line across MTD 4 (see Fig. 3.6 for location). Note how the landslide mass is buttressed against undisturbed strata. (**b)** Frontally emergent landslide. Seismic Inline 2352 across MTD 6 (see Fig. 3.7 for location). Note the runout of the landslide mass beyond the frontal ramp.

Results

We identified 7 individual MTDs in the 3D data that range in volume from 0.005 to 1.16 km^3, in area from 0.2 to 21.8 km^2, have runouts between 0.55 and 7.88 km, and generally translate downslope from the SE to NW. The MTDs total over 2.8 km^3 in volume and cover more than 59 km^2 of seafloor at various stratigraphic levels. The MTDs have been designated as MTD 1 through MTD 7 based upon their relative temporal occurrences with MTD 1 being the oldest. Measurements for all MTDs are summarized in Table 3.1. Additionally, three surficial MTDs were identified in high resolution bathymetry that were not fully resolvable in the 3D seismic data.

Headwall Domain

Kinematic indicators for the headwall domain were difficult to identify in the data. While headwall scarps were partially or fully identified in most of the MTDs, extensional blocks were completely absent.

Headwall Scarps

Although evidence for headwall scarps exists for most of the landslides, most of them could not be fully identified (Fig. 3.4 – 3.7). All headwall scarps are located under a prominent complex landslide scar identified by Lackey *et al.* (2018a) except for MTD 2. Because of the overlapping nature of their locations, we believe the difficulty in identifying full headwall scarps to be due to erosion by subsequent mass failures at higher stratigraphic levels. This is especially true for MTDs 1, 3, and 6 as there are no discernable headwall scarps in the data leading us to conclude that they have been fully eroded (Fig. 3.4b, 3.5b, 3.7b). Additionally, only a portion of the headwall scarp was identifiable for MTD 4 (Fig. 3.6b).

Table 1. Physical MTD Parameters and Identified Kinematic Indicators

MTD	Stratigraphic Sequence and Age	Volume (km^3)	Area (km^2)	Average Thickness (m)	Runout (km)	Translation Direction	Headwall Domain	Translational Domain*	Toe Domain (Confined/ Emergent)
1	Kumano 4 0.9 Ma – (0.3 – 0.44) Ma	0.999	21.8	45.8	7.884	S → N	None	*LM:* Scarps, En-echelon sigmoidal segments *BSS:* Flats, Grooves *IMB:* Translated Block *TMS:* Second Order Fabric	Confined: Thrusts
2	Kumano 4 0.9 Ma – (0.3 – 0.44) Ma	0.03	1.5	20	1.729	SE → NW	Headwall	*LM:* Scarps *BSS:* Flats *IMB:* None *TMS:* None	Emergent: Pressure Ridges
3	Kumano 3 (0.3 – 0.44) Ma – Present	0.358**	7.73**	46.3	3.238	SE → NW	None	*LM:* Scarps, En-echelon Sigmoidal Segments *BSS:* Ramps, Flats *IMB:* Translated Blocks *TMS:* None	Confined: Thrusts
4	Kumano 3 (0.3 – 0.44) Ma – Present	1.155	14.15	81.62	5.741	SE → NW	Headwall	*LM:* Scarps, En-echelon Sigmoidal Segments *BSS:* Ramps, Flats *IMB:* Translated Blocks *TMS:* None	Mostly Confined: Thrusts
5	Kumano 3 – 2 (0.3 – 0.44) Ma – Present	0.005	0.2	25	0.552	S → N	Headwall	*LM:* Scarps *BSS:* Ramps, Flats *IMB:* None *TMS:* None	Mostly Confined: Thrusts, Pressure Ridges
6	Kumano 2 – 1 (0.3 – 0.44) Ma – Present	0.297	13.1	22.7	4.136	S → N	None	*LM:* Scarps *BSS:* Ramps, Flats *IMB:* None *TMS:* None	Emergent: None
7	Kumano 2 – 1 (0.3 – 0.44) Ma – Present	0.031	1.2	25.8	1.508	SW → NE	Headwall	*LM:* Scarps *BSS:* Flats *IMB:* None *TMS:* None	Emergent: Pressure Ridges

* LM: Later Margins, BSS: Basal Shear Surface, IMB: Internal MTD Body, TMS: Top MTD Surface.

** This is a pre-erosional estimate based on the assumption that 1/3 of the MTD was eroded by MTD 4.

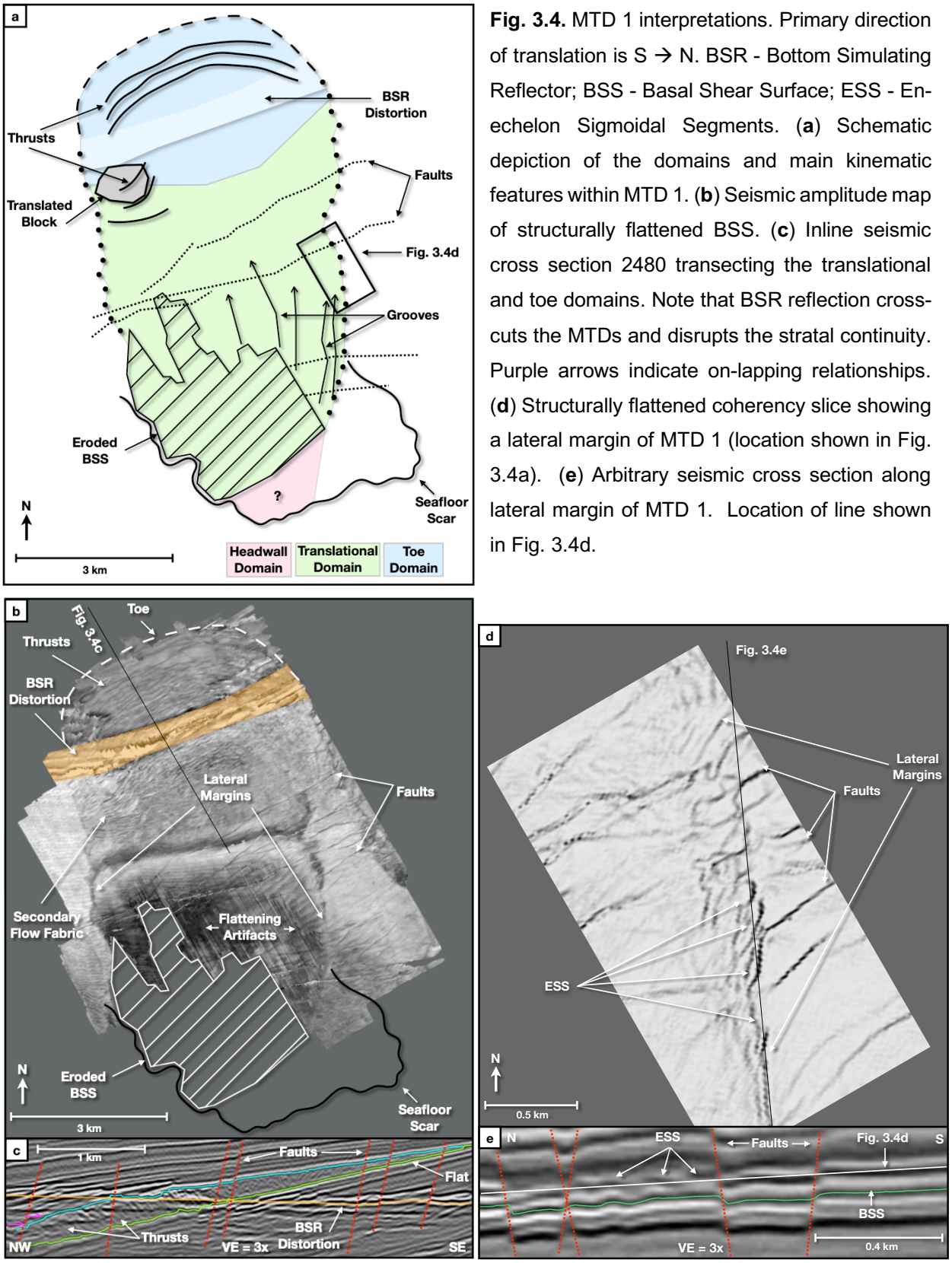

Fig. 3.4. MTD 1 interpretations. Primary direction of translation is S → N. BSR - Bottom Simulating Reflector; BSS - Basal Shear Surface; ESS - En-echelon Sigmoidal Segments. (**a**) Schematic depiction of the domains and main kinematic features within MTD 1. (**b**) Seismic amplitude map of structurally flattened BSS. (**c**) Inline seismic cross section 2480 transecting the translational and toe domains. Note that BSR reflection cross-cuts the MTDs and disrupts the stratal continuity. Purple arrows indicate on-lapping relationships. (**d**) Structurally flattened coherency slice showing a lateral margin of MTD 1 (location shown in Fig. 3.4a). (**e**) Arbitrary seismic cross section along lateral margin of MTD 1. Location of line shown in Fig. 3.4d.

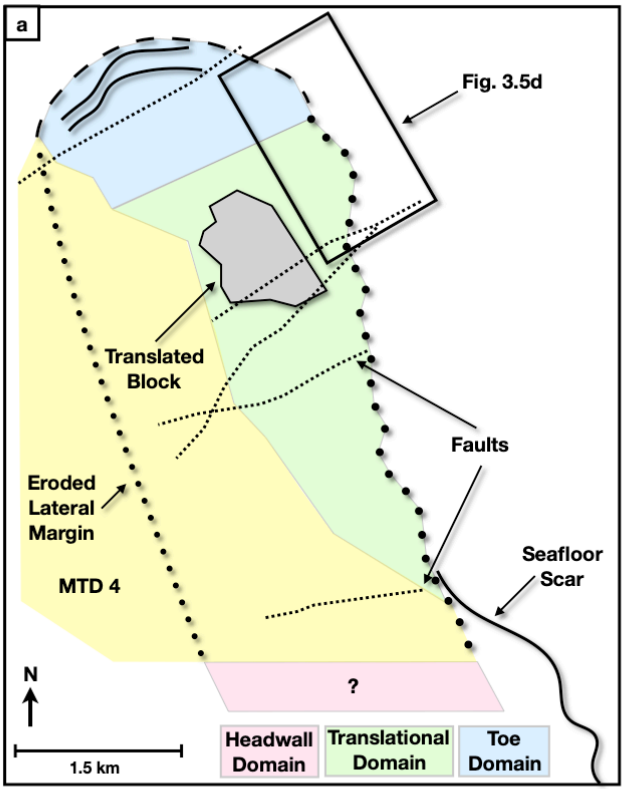

Fig. 3.5. MTD 3 interpretations. Primary direction of translation is SE → NW. BSS - Basal Shear Surface; ESS - En-echelon Sigmoidal Segments. (**a**) Schematic depiction of the domains and main kinematic features within MTD 3. The question mark indicates an undefined headwall domain due to erosion. The large yellow area indicates the location of MTD 4. (**b**) Seismic amplitude map of structurally flattened top surface of MTD 3 (blue line in Fig. 3.5c). Inset is a structurally flattened portion of the BSS showing thrusts in the toe domain. (**c**) Inline seismic cross section 2492 transecting the translational and toe domains (location shown in Fig. 3.5b). (**d**) Structurally flattened coherency slice showing a lateral margin of MTD 3 (location shown in Fig. 3.5a). Note the en-echelon sigmoidal segments. (**e**) Arbitrary seismic cross section along lateral margin of MTD 3 (location shown in Fig. 3.5d).

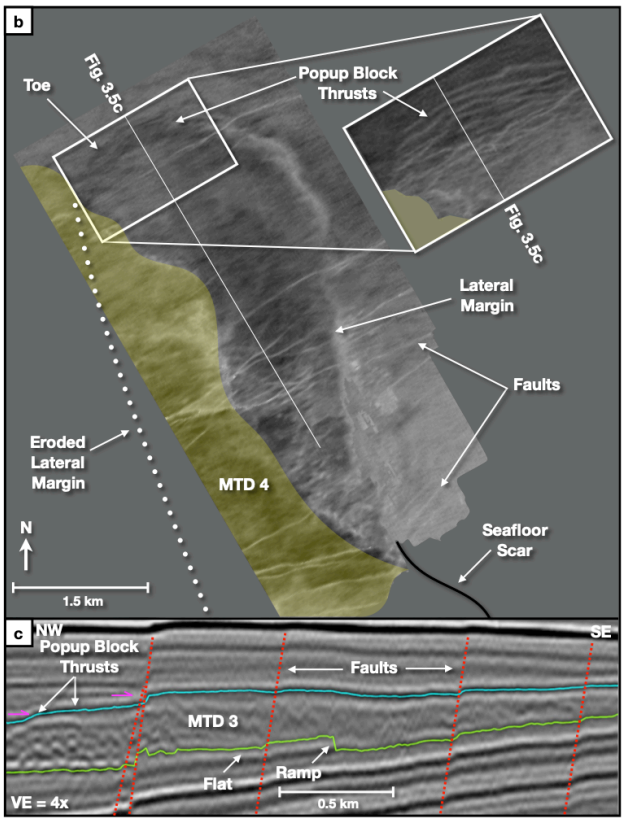

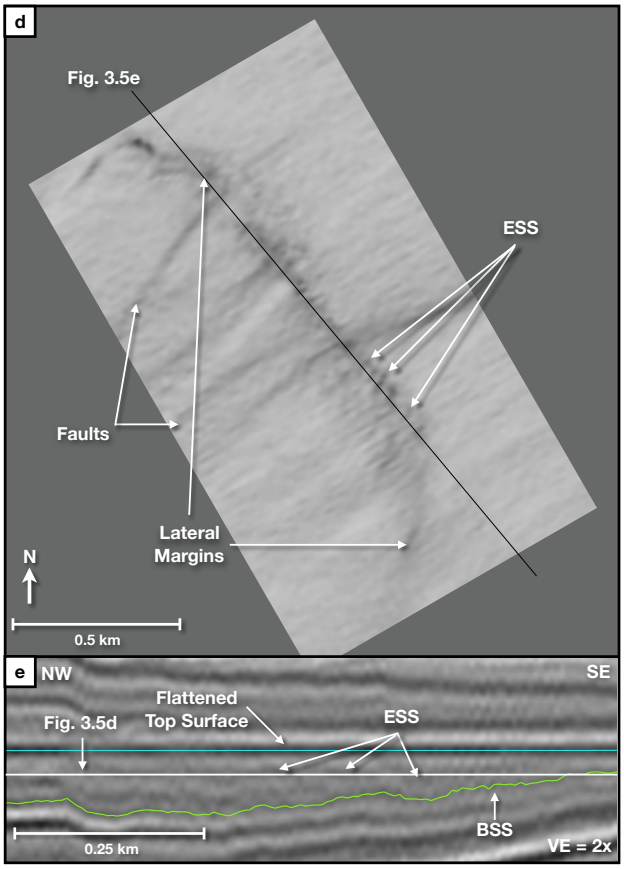

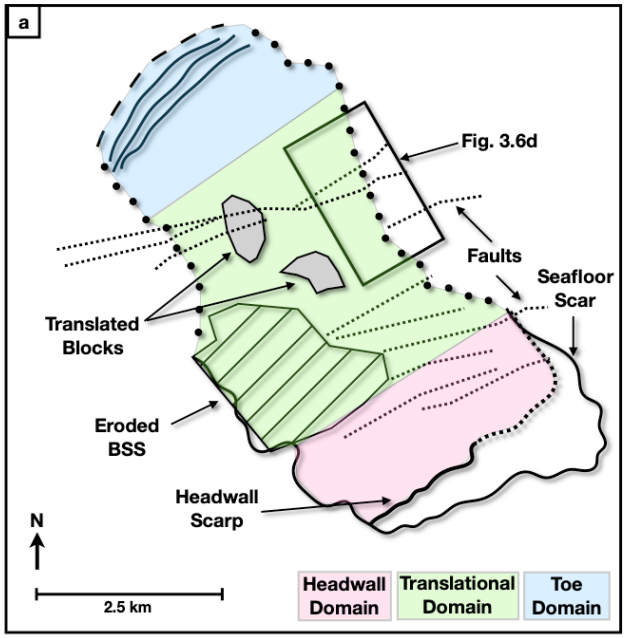

Fig. 3.6. MTD 4 interpretations. Primary direction of translation is SE → NW. BSS - Basal Shear Surface; ESS - En-echelon Sigmoidal Segments. a Schematic depiction of the domains and main kinematic features within MTD 4. (**b**) Coherency map of structurally flattened BSS. (**c**) Arbitrary seismic cross section transecting MTD 4 from the headwall domain to the toe domain (location shown in Fig. 3.6b). (**d**) Structurally flattened coherency slice showing lateral margin of MTD 4 (location shown in Fig. 3.6a). Note the en-echelon sigmoidal segments. (**e**) Arbitrary seismic cross section along lateral margin of MTD 4 (location of line shown in Fig. 3.6d).

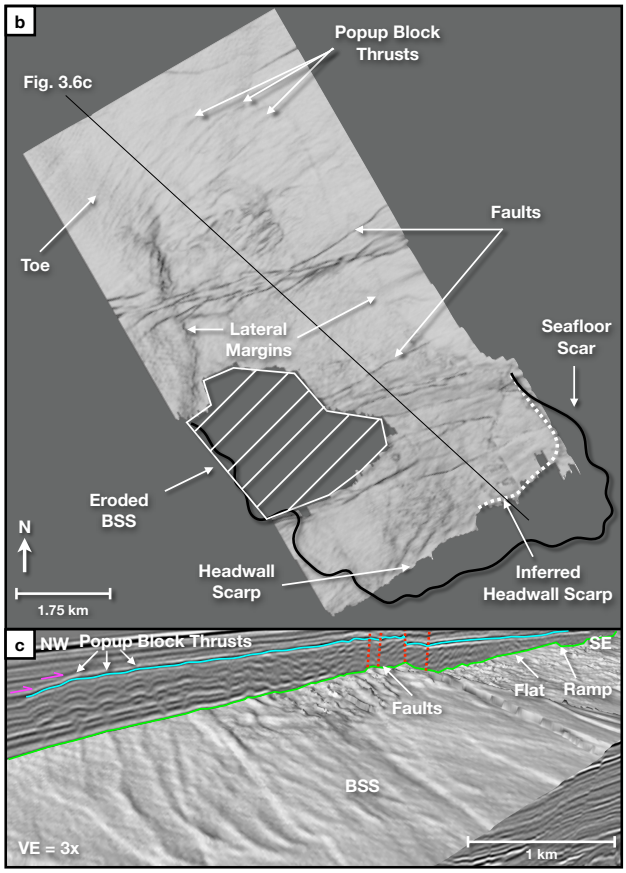

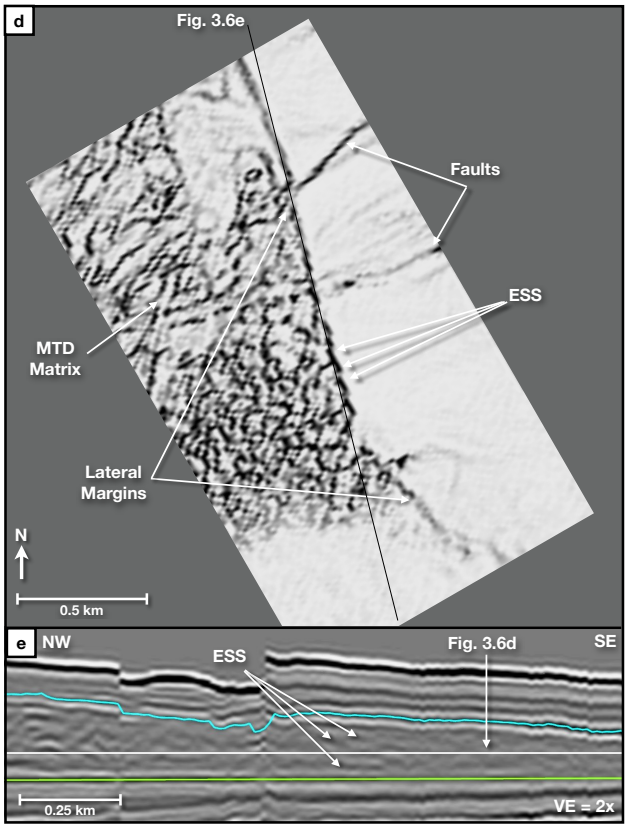

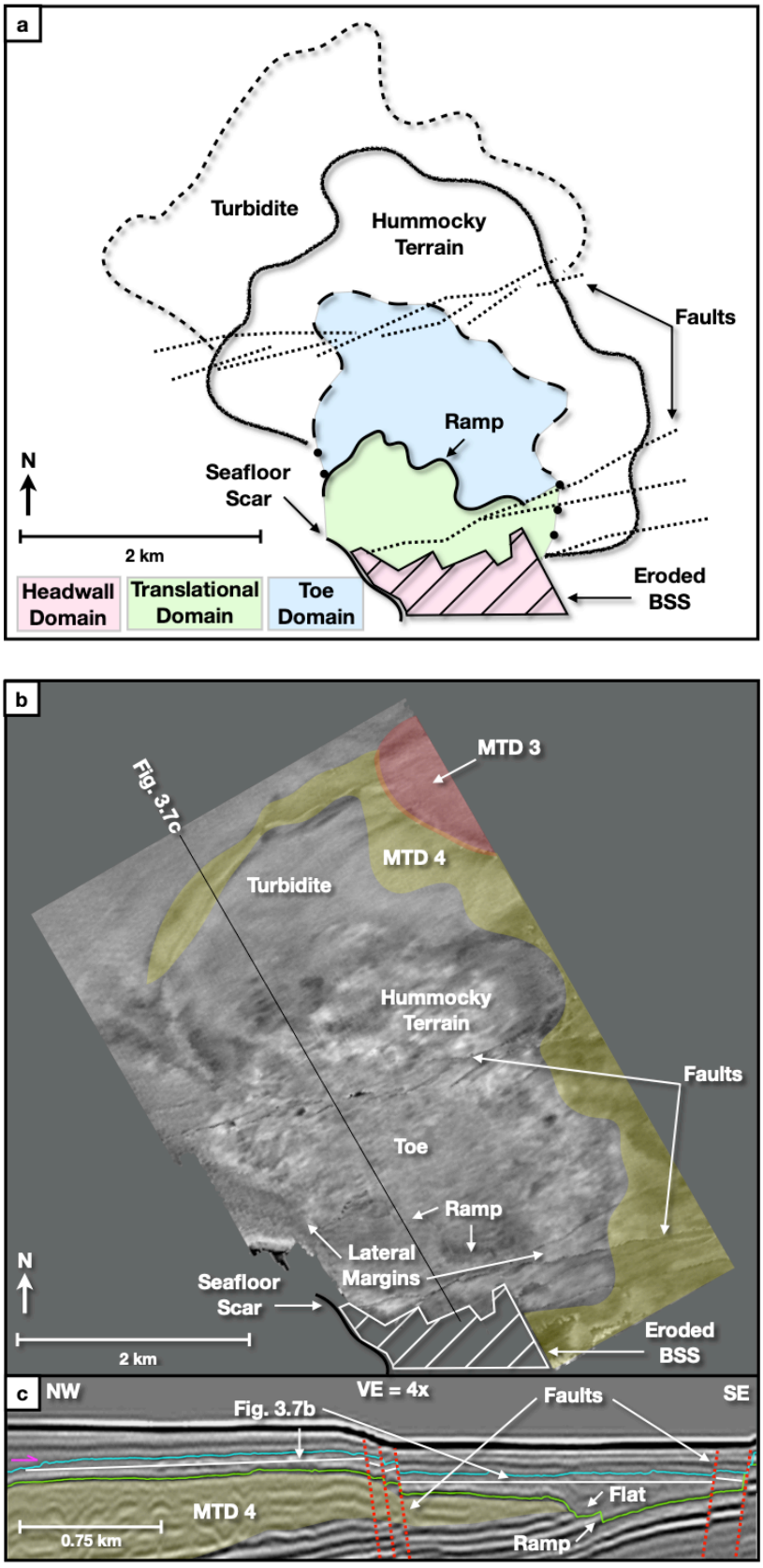

Fig. 3.7. MTD 6 interpretations. Primary direction of translation is S → N. BSS - Basal Shear Surface. (**a**) Schematic depiction of the domains and main kinematic features within MTD 6. Distribution of hummocky terrain and a turbidite are also identified. (**b**) Structurally flattened amplitude slice through MTD 6. Inline seismic cross section 2352 transecting the translational and toe domains of the MTD. Location shown in Fig. 3.7b. (**c**) Inline seismic cross section 2352 transecting all three domains (location shown in Fig 3.7b). Note the hummocky reflections in the NW half of the cross section.

Extensional Ridges and Blocks

No extensional blocks were identified for any of the MTDs. The most likely reasons for their absence are that the headwall regions were fully evacuated of material, subsequent erosion by stratigraphically higher failures (as with the headwall scarps), or insufficient resolution of the data. All headwall regions appear to be void of any failure material, indicating that any extensional blocks that may have formed continued to translate downslope and become blocks in the translational domain or fully disintegrated into the MTD matrix. Because we believe many of the headwall scarps were eroded by subsequent mass failures, it is also likely that any extensional blocks that may have remained immediately after failure were also eroded.

Translational Domain

The majority of the kinematic indicators found in the data are located in the translational domain. Lateral margins, ramps, and flats are well represented in the data. We believe this domain to be so well represented due to it containing the bulk of the failed material for each MTD and because almost all the translational domains were well preserved and imaged when compared to the headwall and toe domains.

Lateral Margins

All MTDs have lateral margin scarps that are visible in the data. Some of the margins are easily interpreted for the entire MTD (Fig. 3.4b, 3.6b) while others have either been eroded by subsequent mass failure (Fig. 3.5b) or are not fully resolvable in the data (Fig. 3.7b). En-echelon sigmoidal segments are imaged in MTDs 1, 3, and 4 (Fig. 3.4d, 3.5d, 3.6d). Only portions of the lateral margins exhibit these segments and in each instance the segments are only 50 to 100 m in length.

There was added difficulty in the accurate identification of lateral margins as the strata are offset by numerous faults throughout the 3D volume (Moore *et al.* 2013). To overcome this, seismic amplitude and coherency are displayed onto interpreted horizons that are then structurally flattened (Fig. 3.8). When viewing an internal amplitude slice using MTD 1's structurally flattened basal shear surface, a linear break in amplitude

appears upslope of the main body of failed material (Fig. 3.4b). The orientation of this linear feature is consistent with the MTD's other kinematic indicators such as grooves found in the basal shear surface. These data support an interpretation that this linear feature is most likely a lateral margin.

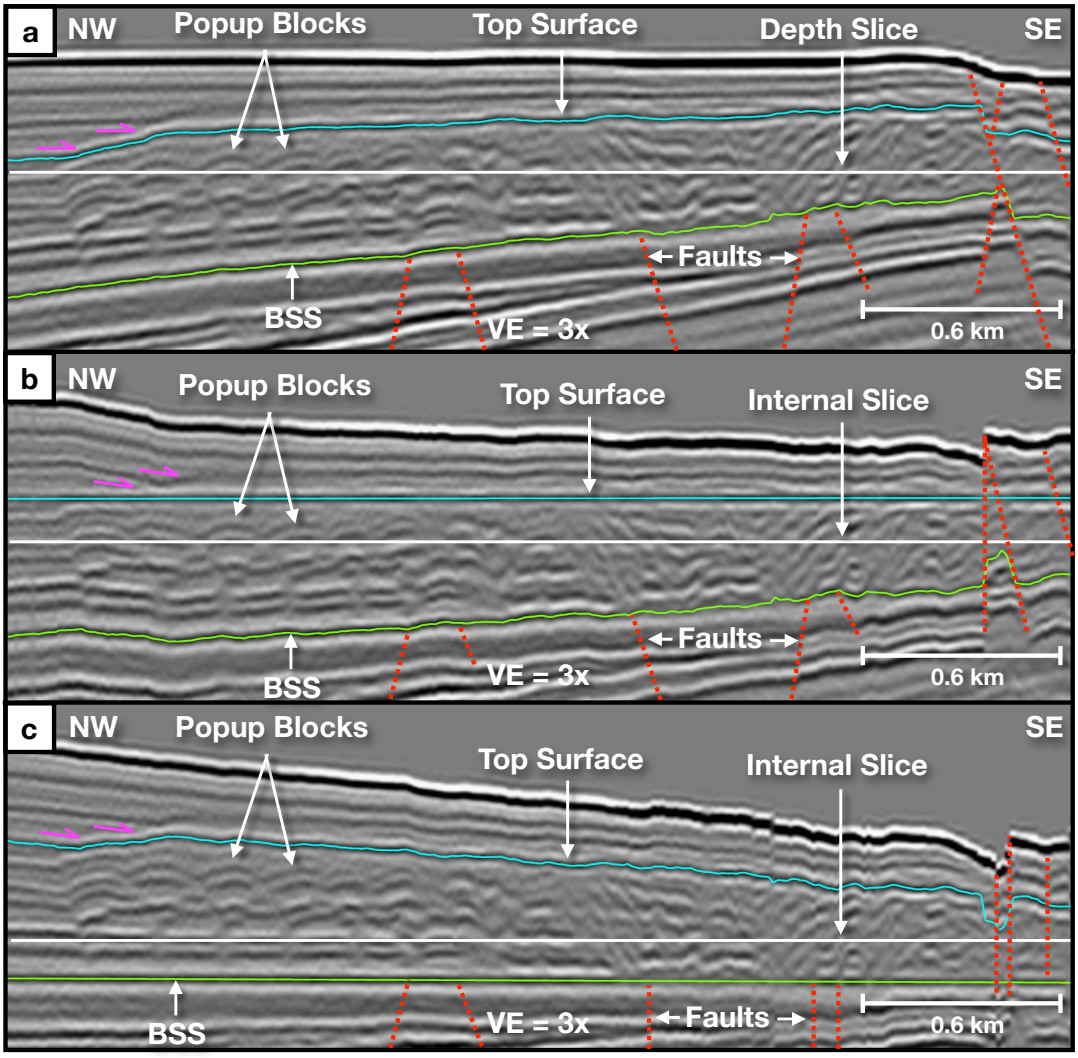

Fig. 3.8. Structural flattening of interpreted horizons. See Fig. 3.11a for arbitrary line location. Primary direction of translation is SE → NW. BSS - Basal Shear Surface. Purple arrows indicate on-lapping relationships. (**a**) Arbitrary seismic line of MTD 4 toe domain. Note how the depth slice (white line) intersects the pop-up blocks at various stratigraphic levels. (**b**) Structurally flattened top surface. Note how the flattened image permits an internal slice (white line) to cross the top surface of each pop-up block. (**c**) Structurally flattened BSS. Note how the flattened image permits an internal slice (white line) to cross the pop-up blocks at the same stratigraphic level near the BSS.

Basal Shear Surface

The basal shear surfaces for all MTDs are mapped to their fullest extent possible. Many of the surfaces are incomplete due to uncertainties in the data from ubiquitous faulting throughout the data set or due to erosion from subsequent mass failures. Grooves appear in the basal shear surface of only MTD 1 and are made visible only by displaying amplitude data onto a structurally flattened basal shear surface. The fact that they do not show in seismic cross section suggests that these features are near the limit of the data's resolution. This could also explain their absence in the remainder of the MTDs.

Flats are present in all the MTDs as all their basal shear surfaces are primarily parallel to the local stratigraphy. Ramps, however, are only located in MTDs 3, 4, 5, and 6 (Fig. 3.5c, 3.6c, and 3.7c) and all trend perpendicular to their MTD's primary flow direction. The absence of parallel trending ramps, by definition, means that slots are also absent from the data (Bull *et al.* 2009). Additionally, there are no instances of the basal shear surface ramping down and cutting into the underlying stratigraphy, only ramping up to higher stratigraphic levels.

None of the MTD basal shear surfaces exhibit signs of striations. As these features are caused by out-runner blocks (of which there were none identified), their absence is not a surprise. It is possible, however, that these features exist, especially for the MTDs that are partially or fully emergent and are simply unresolvable in the data.

Internal MTD Body

Translated blocks were identified in MTDs 1, 3, and 4 (Fig. 3.4a, 3.5a, 3.6a). Their absence in the remaining MTDs likely has a connection with their average thickness (Table 3.1). Because each stratigraphic horizon is roughly equal to the vertical resolution of the data, a block would need to be at least 20 – 28 m (4x the vertical resolution) in height to be easily distinguishable from the surrounding strata. The average thickness of MTDs 2, 5, 6, and 7 is 20 – 26 m. Therefore, any blocks within the failed mass of these MTDs could have been easily overlooked as belonging to the local stratigraphy. This may

also explain the absence of remnant and out-runner blocks as neither of these block types were identified for any of the MTDs.

Outside of the toe domain's thrust and fold systems, folds were not identified in any of the MTDs. Given the large degrees of deformation and the runouts for these deposits, it is unlikely that folding did not take place during emplacement. Therefore, the most likely explanation for their absence is that they are below the resolution of the data as folding has been identified in sub-seismic scale failures in outcrop (Farrell 1984; Lucente and Pini 2003; Matheus *et al.* 2017).

Top MTD Surface

Only MTD 1 exhibited a kinematic indicator from the top surface. A second order flow fabric was identified above and around a translated block (Fig. 3.4b). The likely explanation for this fabric centers around the MTD's translated block. It likely became buttressed against the lateral margin of the MTD, causing the failed material to be forced around the flow obstruction which lead to thrusting within the failed mass and a secondary fabric in the top surface (Fig. 3.4b).

There were no instances of longitudinal shear zones in any of the MTDs. The majority of these types of kinematic indicators have been found on much larger MTDs in other places around the world (Masson *et al.* 1993; Gee *et al.* 2005; Gafeira *et al.* 2007). Therefore, we believe that the MTDs in this study are either too small to exhibit such differences in flow speed within the failed mass or that this indicator is simply not resolved in the data.

Toe Domain

The toe domain is identified on all MTDs. However, although the toe of MTD 6 was identifiable, it lacked any kinematic indicators within the domain (Fig. 3.7). The most likely explanation for this absence is that the toe domain is not thick enough to either contain or resolve any of the indicators. Also unique to MTD 6 were a hummocky terrain and turbidite located beyond the toe domain. Their existence is likely due to the amount of material scoured from MTD 4 during the emplacement of MTD 6 (eroded BSS; Fig. 3.6).

The toe domain of MTD 1 also proved difficult to map. A strong bottom simulating reflector (BSR) caused by gas hydrate accumulations is imaged 200 – 400 mbsf across the entire area of interest within the 3D seismic volume (Miyakawa *et al.* 2014). This led to inaccuracies in mapping the toe domain of MTD 1, causing kinematic indicators that would otherwise be visible to be either partially or fully obscured (Fig. 3.4).

Thrust and Fold Systems

Thrust and fold systems were identified in MTDs 1, 3, 4, and 5 (Fig. 3.3c, 3.5c, and 3.6c). The confined nature and thickness of these MTDs are the primary causes of the thrust and fold systems. Of note, MTDs 3 and 4 both display pop-up block systems while MTDs 1 and 5 exhibit simple thrust systems. It is possible, however, that MTD 1 also contains pop-up blocks as its thickness is similar to that of MTD 3. The BSR that obscures MTD 1's toe domain may simply prevent the pop-up blocks from being resolvable (Fig. 3.3c).

Pressure Ridges

MTDs 2 and 7 both exhibit pressure ridges in their toe domains. Because thrusts are typically found in conjunction with pressure ridges in outcrop (Masson *et al.* 1993; Gee *et al.* 2005; Gafeira *et al.* 2007), it is likely that some sort of thrust system exists in both MTDs and are simply too small to resolve in the 3D data.

Surficial MTDs

The seafloor scar identified by Lackey *et al.* (2018a) appears to contain at least three surficial MTDs that could not be fully identified in the 3D data (Fig. 3.9b). These MTDs are clearly visible as seafloor features in high resolution bathymetry (Strasser *et al.* 2017). Their absence from the 3D data is likely due to their relatively small scale and their recent occurrence. Because they are recent failures, they have yet to be buried and will, therefore, be poorly imaged in 3D seismic data. While kinematic indicators from these surficial MTDs cannot be identified in the 3D data, they are still important in understanding the evolution of the seafloor with respect to this study.

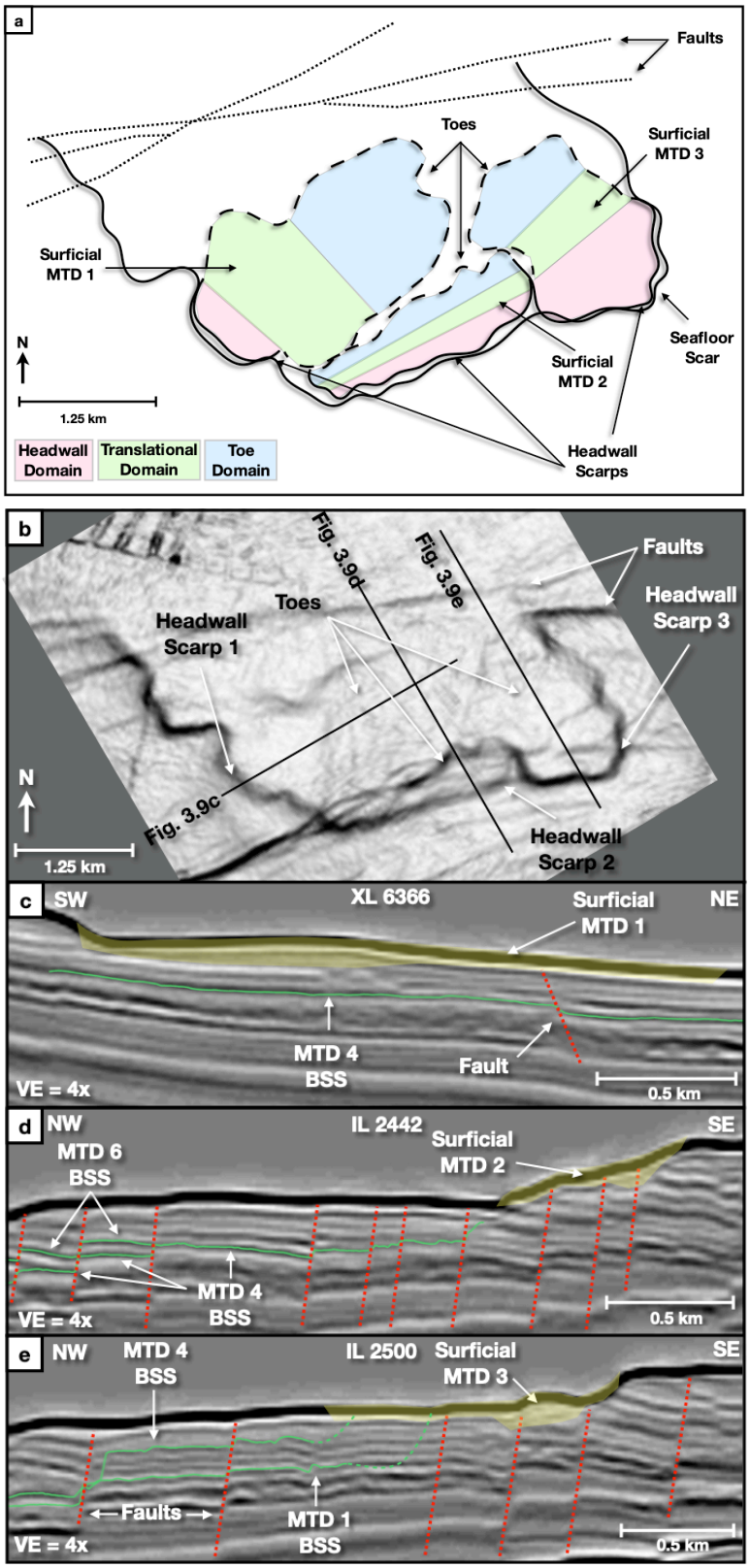

Fig. 3.9. Surficial MTDs.

(**a**) Schematic depiction of three surficial MTDs.

(**b**) Bathymetric image of surficial landslide scar showing the location of three surficial landslides.

(**c**), (**d**), (**e**) Seismic cross sections across the surficial MTDs in the 3D seismic data. Green lines are BSSs of older landslides. Red dotted lines are normal faults.

Discussion

The MTDs identified in this study exhibit numerous kinematic indicators that enable us to determine the spatial and relative temporal origin of each failure. We have reconstructed each of the failures to their original positions and, using the local stratigraphy, temporally sequenced each failure in the most probable order (Fig. 3.10). Each of the MTDs (with the notable exception of MTD 2) appear to originate stratigraphically below the seafloor scar identified by Lackey *et al.* (2018a). These, combined with the three surficial deposits that could not be identified in the 3D data, fully explain the geometry of the scar.

We interpret the scar's location to be associated with the local depositional and tectonic environment over the past 0.9 Ma. All MTDs are located within the stratigraphic sequences Kumano 4 – Kumano 1 identified by Gulick *et al.* (2010). Kumano 4 is the oldest of these sequences, with deposition beginning ~0.9 Ma. During this time, motion along a prominent out of sequence thrust (OOST) was reactivated, potentially by the continued subduction of a seamount on the Philippine Sea Plate (Kimura *et al.* 2011; Moore *et al.* 2013), causing the outer forearc to continue tilting landward as it had during the deposition of the Kumano 8 sequence ~1.2 Ma (Moore *et al.* 2015). A series of normal faults that are spatially correlated with a SW uplift penetrates through the Kumano 5 and Kumano 4 sequences but does not penetrate the Kumano 4 sequence boundary (K4) (Fig. 3.11b). This indicates that the uplift took place rapidly and ceased by ~0.3 – 0.44 Ma (Moore *et al.* 2015). This rapid uplift and resultant slope steepening coupled with seismic loading could explain the occurrence of MTDs 1 and 2 since they are fully contained within the Kumano 4 sequence and are spatially correlated. Of note, there is a lack of MTDs in stratigraphic sequences older than the Kumano 4 sequence. We believe this to be because of the hiatus in tilting (a key preconditioning factor) between the deposition of Kumano sequences 5 – 7 (Moore *et al.* 2015).

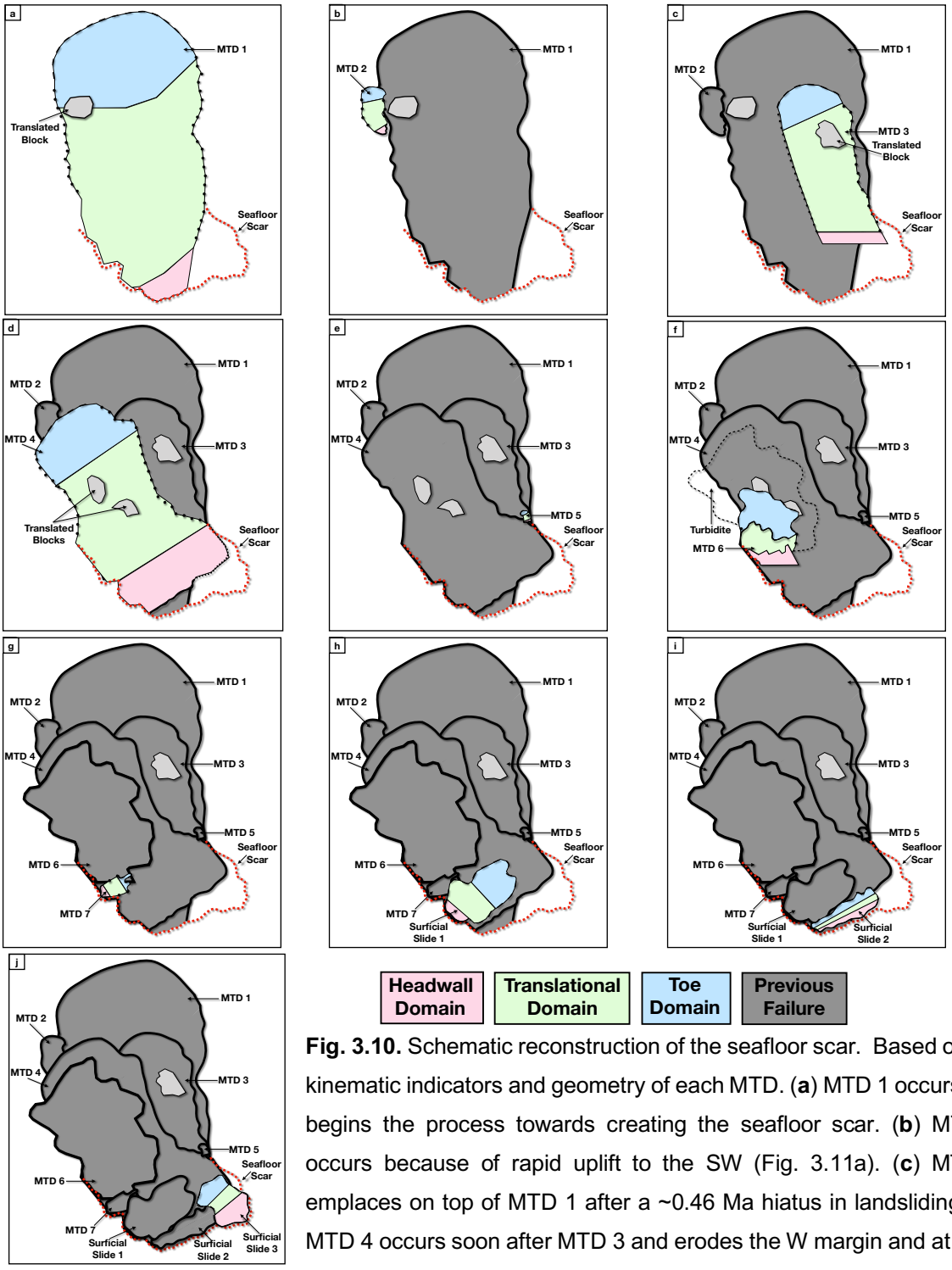

Fig. 3.10. Schematic reconstruction of the seafloor scar. Based on the kinematic indicators and geometry of each MTD. (**a**) MTD 1 occurs and begins the process towards creating the seafloor scar. (**b**) MTD 2 occurs because of rapid uplift to the SW (Fig. 3.11a). (**c**) MTD 3 emplaces on top of MTD 1 after a ~0.46 Ma hiatus in landsliding. (**d**) MTD 4 occurs soon after MTD 3 and erodes the W margin and at least 1/3 of MTD 3 as well as a portion of the BSS of MTD 1. (**e**) MTD 5 is possibly a result of lateral margin failure of either MTD 3 or 4. (**f**) MTD 6 erodes a portion of MTD 4's BSS and deposits a turbidite on its top surface. (**g**) MTD 7 erodes a portion of MTD 6's basal shear surface and creates the W boundary of the seafloor scar. (**h**), (**i**), (**j**) Three surficial landslides finish shaping the current seafloor scar.

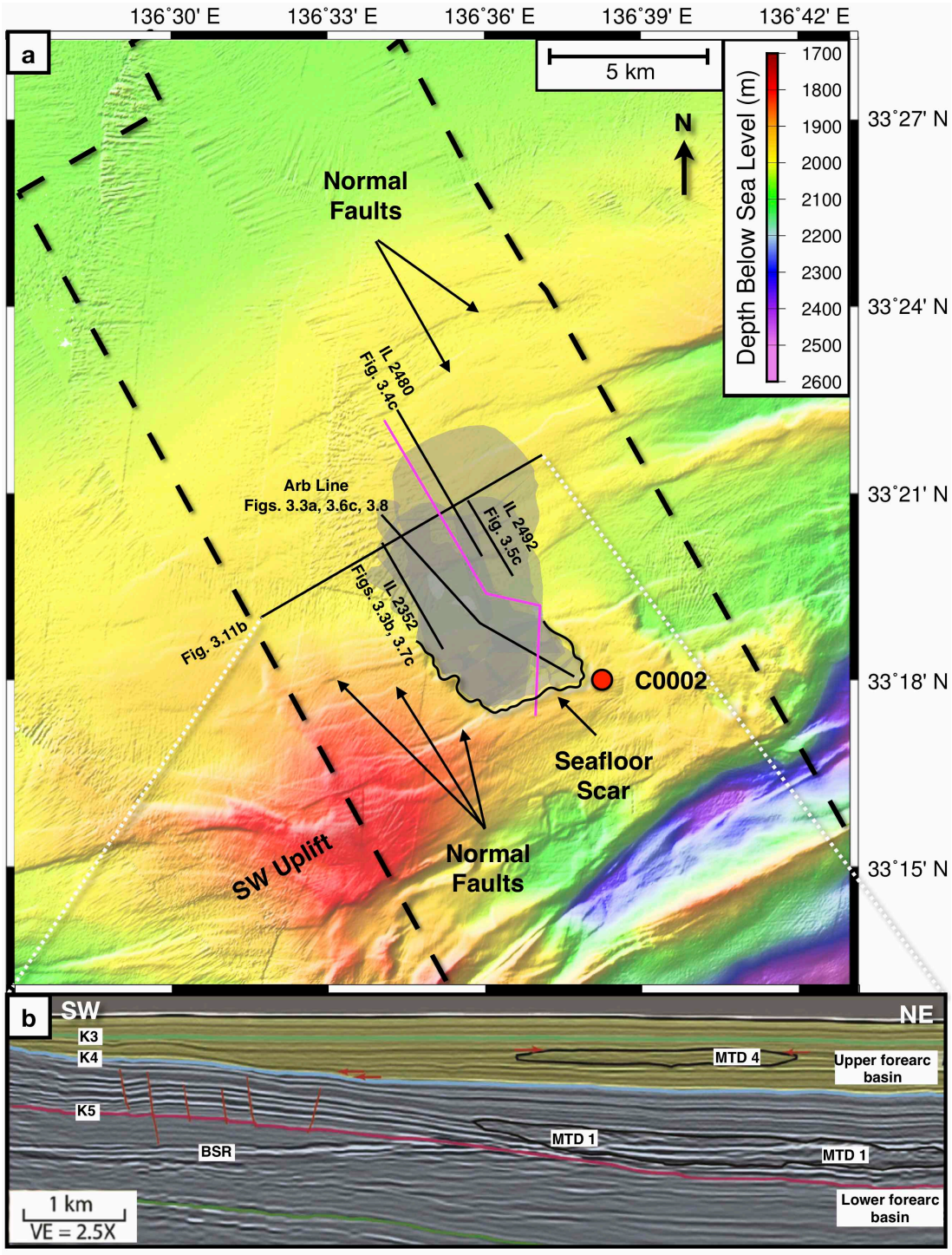

Fig. 3.11. (**a**) High resolution bathymetry showing SW uplift in relation to the seafloor scar. The gray area represents all the identified MTDs. Purple line indicates the location of the Abstract Fig. (**b**) Seismic cross section showing the relative stratigraphic positions of MTD 1 in the Lower forearc basin stratigraphy and MTD 4 within the Upper forearc basin stratigraphy. K3, K4, and K5 are upper boundaries of the Kumano Basin seismic sequences, based on toplap, downlap, onlap, or angular relations as defined by Gulick *et al.* (2010). BSR - Bottom Simulating Reflector. Modified from Moore *et al*. (2015).

MTDs 3 – 7 and the surficial MTDs occur within or above the Kumano 3 sequence, making them < 0.3 – 0.44 Ma in age and indicating potentially different causal mechanisms. Kumano sequences 3 – 1 thicken in the landward direction from < 50 m in the seaward region to > 600 m toward the basin center (Moore *et al.* 2015). Isopach maps created by Moore *et al.* (2015) show a general widening and NW shift of the basin depocenter over time (Fig. 3.12). This shift has led to a decrease in deposition around the seafloor scar since 0.3 – 0.44 Ma and is the most likely explanation for the general decrease in size of the MTDs over time. We infer this because, as sediment deposition decreases with time, there will be less material available to slide. Additionally, the edge of the forearc basin ceased tilting by the deposition of K4 as evidenced by the on-lapping relationships of the Kumano 4 – 1 sequences (Gulick *et al.* 2010). Because neither local steepening nor high rates of sedimentation occurred during the emplacement of MTDs 3 – 7 or the surficial MTDs, another causal mechanism likely exists.

The Nankai region has a well-documented and regular history of small and great earthquake activity (Ando 1975; Kimura *et al.* 2011). Great earthquakes along the margin are documented as far back as 648 AD with a recurrence interval of 100 to 200 years (Ando 1975). If a splay fault, such as the Nankai megasplay, ruptures co-seismically, amplification of seismic ground shaking can occur within the hanging wall (Abrahamson and Somerville 1996). This has been suggested for Nankai and other splay fault systems (e.g., Plafker 1972; Tanioka and Satake 2001; Baba *et al.* 2006), thereby representing a plausible causal link between seismic loading and slope failure. However, as noted by Moore and Strasser (2016) the recurrence interval for landsliding in the Kumano Basin appears to be about 0.05 to 0.1 Ma, which is much less frequent than the recurrence interval for Nankai's great earthquakes. Kremer *et al.* (2017) suggested that this difference could be due to slopes being preconditioned to fail because of climate forcing during interglacial periods. However, they were unable to resolve the relative contributions of tectonic versus climate preconditioning factors and Urlaub *et al.* (2013) showed that the ages of landslides on passive margins can be described by a temporally random Poisson distribution and therefore do not show a positive correlation between the

Fig. 3.12. Kumano Basin sedimentation through time. (**a**) Map showing the primary sediment inputs to the Kumano Basin. Solid lines show present-day pathways; dashed lines show possible older pathways. Note the bathymetric high to the NE of the 3D seismic volume that prevents modern sedimentation near IODP cite C0002. Red dots are IODP drill sites. White box shows location of isopach maps. (**b**) – (**f**) Isopach maps of Kumano Basin stratigraphic sequences. Sequence Kumano 1 is the youngest sequence; Kumano 5 is the oldest. White dots show the thickest point of the basin during each isopach interval. Identified MTDs that occur within each sequence are shown for reference. The pattern of deposition changes once the SW uplift appears during the Kumano 4 sequence. Additionally, a lack of sedimentation at the headwalls during Kumano sequences 3 – 1 helps to explain the reduction in size of MTDs 5 – 7 and the surficial MTDs. Because their relative timing cannot be determined from the data, MTDs 6 and 7 are shown in both the Kumano 3 and 2 maps and the surficial MTDs are shown in both the Kumano 2 and Kumano1 maps (**d**), (**e**), and (**f**). SS – Surficial Slide. Modified from Moore *et al.* (2015).

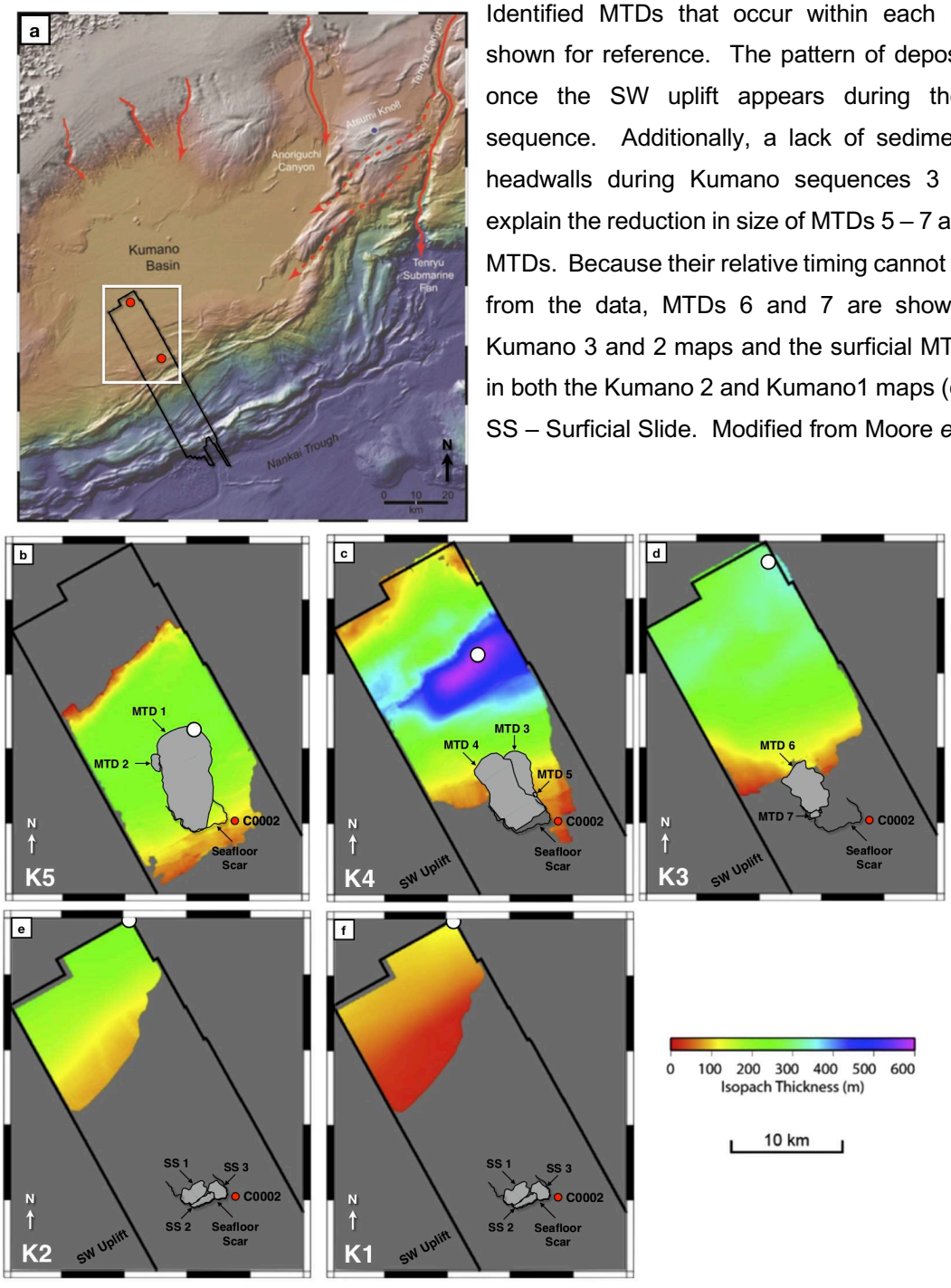

frequency of major slope failures on passive margins and sea level changes during the past 0.18 Ma. Another possibility is that the extent of up dip rupture propagation along the megasplay fault is not always sufficient to cause slope failure. Ikari *et al.* (2011) found that the triggering of slope failure for a statically stable slope by a M_w 6-8 earthquake requires the megasplay to rupture within 12 km of the slope.

Shear strengthening (Locat *et al.* 2002; Lee *et al.* 2004) could also be an explanation as to why failure is less frequent than the great earthquake recurrence interval, especially for M_w 6-8 earthquakes (Ikari *et al.* 2011). An instantaneous increase in pore pressure is induced on saturated, fine-grained sediment during an earthquake. This temporarily weakens the sediment. However, if it is not weakened to the point of failure, the pore pressure diffuses over time permitting the sediment to become over-consolidated. Therefore, an earthquake that does not cause slope failure could lead to an increase in the slope's shear strength that increases its resistance to future failures (DeVore and Sawyer 2016). A resistance to future failure implies that either an even larger earthquake would be required to initiate sliding or another causal mechanism is ultimately at work such as the activation of a fault.

Three normal fault populations exist in the study area. The youngest population (Phase 3; Sacks *et al.* (2013); Moore *et al.* (2013)), tends to cut the upper strata of the forearc basin and manifest as scarps on the seafloor which have been identified in this study. Sacks *et al.* (2013) proposed a mechanism, via the earthquake cycle, by which the differing orientation of these fault populations and the arcuate geometry of the faults associated with our study originated. During the late inter-seismic period, faults perpendicular to the trench can undergo slip, while faults oriented parallel to the trench undergo slip during post-seismic extension. Additionally, Moore *et al.* (2013) showed that these faults are likely short-lived rather than regional phenomenon as they lack growth structures. These two conclusions support the idea that these faults occur in conjunction with the earthquake cycle.

A landslide does not occur during each seismic event, possibly in part to the effects of shear strengthening. However, landsliding can occur because of the change in the regional stress regime during the post-seismic phase of the earthquake cycle leading to favorable normal faulting conditions that strike parallel to the trench axis. Because all of the MTDs in this study (except for MTDs 1 and 2, likely caused by local over steepening and seismic loading) appear to have headwall scarps either on or near a trench parallel fault within the youngest of Sacks *et al.*'s (2013) populations, we propose that the primary final trigger mechanism for these nested MTDs is failure as a result of faulting during the post-seismic relaxation of the accretionary prism or massive megathrust earthquakes along the megasplay fault.

Conclusions

A series of nested MTDs is imaged using both 3D seismic data and high-resolution bathymetry in the outer forearc of the Kumano Basin. The nested nature of the observed MTDs and the stratigraphic sequences in which they occur show how sedimentation of the Kumano Basin and tectonic activity of the Nankai accretionary prism affect local mass wasting. We use kinematic indicators from the observed MTDs to reconstruct a prominent seafloor scar. Local slope over-steepening from a rapid uplift SW of the study area possibly coupled with seismic loading caused the initiation of landsliding in the study area ~0.9 Ma. Subsequent failures likely occurred because of faulting caused by post-seismic relaxation of the accretionary prism and seismic activity from (0.3 – 0.44) Ma – present.

Acknowledgements

The new bathymetric compilation was made possible by the hard work of the SO251 Hydroacoustic Group (C. dos Santos Ferreira, K. Bachmann, K. Lange, J. Moernaut). We thank two anonymous reviewers for comments that greatly improved the manuscript. Paradigm Geophysical and Blue Marble Geographics for making their software available to us. The 3D data reprocessing was supported by the Japan Society for the Promotion of Science (JSPS) through a KAKENHI Grant-in-Aid for Scientific Research S (JP15H05717), and by the Ministry of Education, Culture, Sports, Science, and Technology (MEXT) through management expense grants at the Research and

Development Center for Ocean Drilling Science (ODS) and the Center for Deep Earth Exploration (CDEX) of Japan Agency for Marine-Earth Science and Technology (JAMSTEC). SOEST Contribution # 10345.

CHAPTER 4
TECTONIC INFLUENCES ON SLOPE BASIN DEVELOPMENT VIA STRUCTURAL RESTORATION ALONG THE OUTER NANKAI ACCRETIONARY PRISM, SOUTHWEST JAPAN

This chapter will be published as: Lackey JK, Moore GF, Strasser M (2019) Tectonic influences on slope basin development via structural restoration along the outer Nankai accretionary prism, southwest Japan.

Abstract

Three-dimensional (3D) seismic data and sediment cores record ~2.87 million years of structural and depositional history of a trench slope basin along the outer Nankai accretionary prism, SW Japan. Numerous mass transport deposits (MTDs) and fault structures are present in the data. Here, we investigate the links between slope failures, trench slope basin development, and movement along a prominent out-of-sequence thrust (OOST) fault and a large anticline. Three two-dimensional (2D) cross sections are reconstructed ~2.4 Ma using stratigraphic and structural relationships interpreted in the 3D data. The reconstructions are then compared and combined to provide a 3D perspective of basin development. We find that the OOST is slipping differentially along multiple branches, with 5.5 km, 4.8 km, and 5.7 km of shortening from NE to SW over the past ~2.4 Ma. In the NE, deformation is primarily accommodated by the parent OOST and internal anticlinal faulting, while deformation in the SW is primarily along deeper branches of the OOST. This differential motion explains the occurrences of various mass wasting events, to include a previously identified prominent MTD, and bathymetric differences within the study area. We suggest that the differential motion is caused by a combination of strike-slip related faulting within the prism to the SW and by seamount subduction to the NE.

Introduction

Accretionary prisms are a dominant structural component of many convergent margins, such as Barbados, the Aleutians, Sunda, Cascadia, and the Nankai Trough (e.g., McCarthy & Scholl, 1985; Moore *et al.*, 1989; Moore *et al.*, 1990; Gutscher *et al.*, 2001; Kopp & Kukowski, 2003). These prisms form from sediment scraped off the incoming oceanic plate. As they accrete new material, their taper is maintained via fold and fault structures that form along the length of the prism (Davis *et al.*, 1983; Dahlen *et al.*, 1984). Hemipelagic and terrigenous sediment is deposited on the prism during its growth and can form small trench slope basins 200+ m thick (Kimura *et al.*, 2011; Strasser *et al.*, 2011; Underwood & Moore, 2012). The structural changes within the underlying prism, along with other preconditioning factors, such as gas hydrate dissociation or earthquake cycle related faulting (e.g., Bangs *et al.* 2010; Sacks *et al.* 2013; Kremer *et al.*, 2017; Lackey *et al.* 2018b), provide an environment in which subaqueous landslides may occur, shaping the surface of the prism.

Subaqueous landslides occur in many different environments all over the world, including both active and passive margins, along the flanks of volcanic islands, and river deltas (Prior & Coleman, 1978; Moore *et al.*, 1989; Lee, 2009), and they are prominent morphologic features along the Nankai and other accretionary prisms (Prior & Coleman, 1978; Moore *et al.*, 1989; Lee, 2009; Lackey *et al.*, 2018a, b). These slides can be devastating to seafloor infrastructure via high speed turbidity currents and to coastal communities in the form of tsunamis (Bondevik *et al.*, 1997; Bardet *et al.*, 2003; Satake, 2012). Moreover, investigating and characterizing submarine landslides allows us to better understand how they initiate and translate downslope to the point at which they arrest (Ward & Day, 2002).

The primary trigger mechanism for a subaqueous landslide can be difficult, if not impossible, to determine due to a lack of conclusive data. However, various mechanisms for failure initiation, based upon a landslide's location and characteristics, may be suggested. Co-seismic rupture of a fault, such as the Nankai megasplay (MS), can amplify ground shaking within the hanging wall (Abrahamson & Somerville, 1996) and

lead to slope failure. This has been suggested for Nankai and other splay fault systems (e.g., Plafker, 1972; Tanioka & Satake, 2001; Baba *et al.*, 2006). Free methane gas venting or hydrate dissociation from within the underlying strata could also initiate landsliding locally or on kilometer scale sections of the seafloor (Westbrook *et al.*, 2009; Bangs *et al.*, 2010).

This study represents an opportunity to analyze tectonic influences on slope failures and trench slope basin development along the outer Nankai accretionary prism. Strasser *et al.* (2011) and Lackey *et al.* (2018a, b) identified and proposed numerous trigger mechanisms for several MTDs and surficial landslide scars respectively that spatially correlate with the MS. Analyses of sediment cores obtained by the International Ocean Drilling Program (IODP) during Expedition 316 (Expedition 316 Scientists, 2009a, b, c) provide age constraints on prominent stratigraphic horizons and MTDs within the study area. Utilizing the core data and a 3D seismic reflection survey, we aim to investigate the underlying geologic processes and influences on slope failures via a comprehensive structural reconstruction.

Regional Setting and Study Area

The Nankai accretionary prism is within the Nankai Trough subduction zone where the Philippine Sea Plate is presently subducting under the Amur Plate at a rate of 4 to 6 cm yr^{-1} (Kimura *et al.*, 2007a). The NW oblique subduction has led to the prism spanning roughly 700 km, with the overall oblique slip being apportioned along a large right lateral strike-slip fault, known as the Median Tectonic Line, landward of the prism (Fitch, 1972; Taira, 2001). The sediment comprising the prism is primarily terrigenous detritus from Japan and hemipelagic deposits in the Shikoku Basin of the Philippine Sea Plate (Underwood & Moore, 2012), the upper part of which is accreted while the lower part is subducted beyond the inner prism (e.g., Kinoshita *et al.*, 2009; Kimura *et al.*, 2011; Strasser *et al.*, 2011, 2012; Underwood & Moore, 2012; Moore *et al.*, 2014). The rapid growth of the accretionary prism is an important factor for large, repeated earthquakes (~100 – 200-year recurrence interval (Ando, 1975)) in this subduction zone setting (Ruff & Kanamori, 1980).

The study area is along the outer accretionary prism just seaward of the Kumano Basin where the trench slope basin sediment is being overridden by the MS (Fig. 4.1, 4.2, 4.3). The 3D seismic data used for this study is located entirely within the transition zone of the accretionary prism between 35 and 50 km from the deformation front (Kimura *et al.*, 2007b) and covers roughly 275 km^2 (Moore & Strasser, 2016). Water depths vary from ~2950 m at the seaward edge of the study area to ~2150 m at the landward edge. Notable characteristics include the shallow extent of the MS, various landslide scars in both the 3D survey and bathymetry, and large anticlines (e.g., Strasser *et al.*, 2009, 2011; Moore *et al.*, 2013; Lackey *et al.*, 2018a, b).

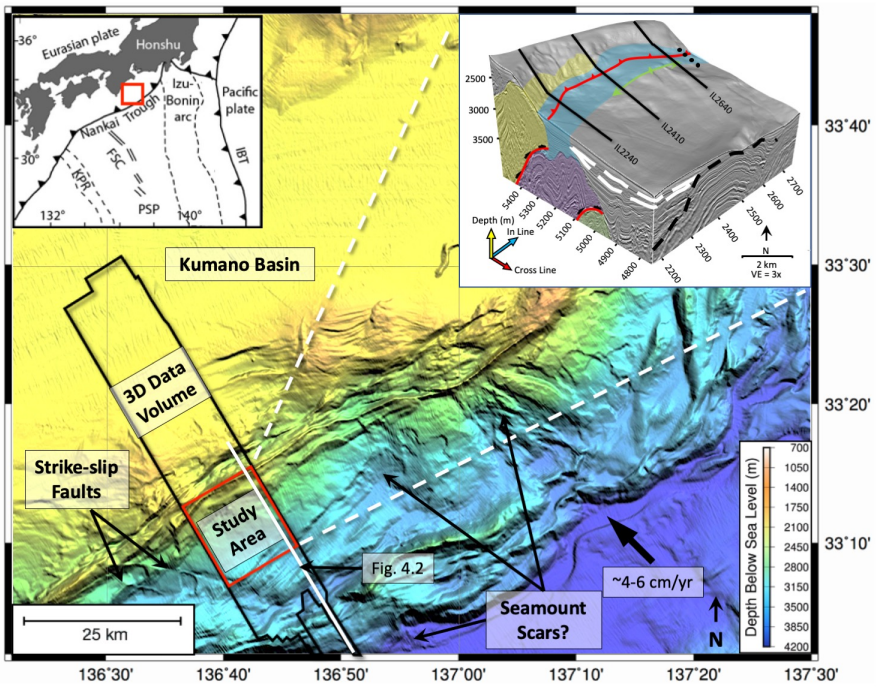

Fig. 4.1. Study Area. High resolution bathymetry of the Kumano Basin (location indicated in the regional inset). Barbed red line in 3D cube inset represents the location of the megasplay (MS; see Fig. 4.3 for greater detail). PSP = Philippine Sea Plate; FSC = Fossil Spreading Center; KPR = Kyushu-Palau Ridge.

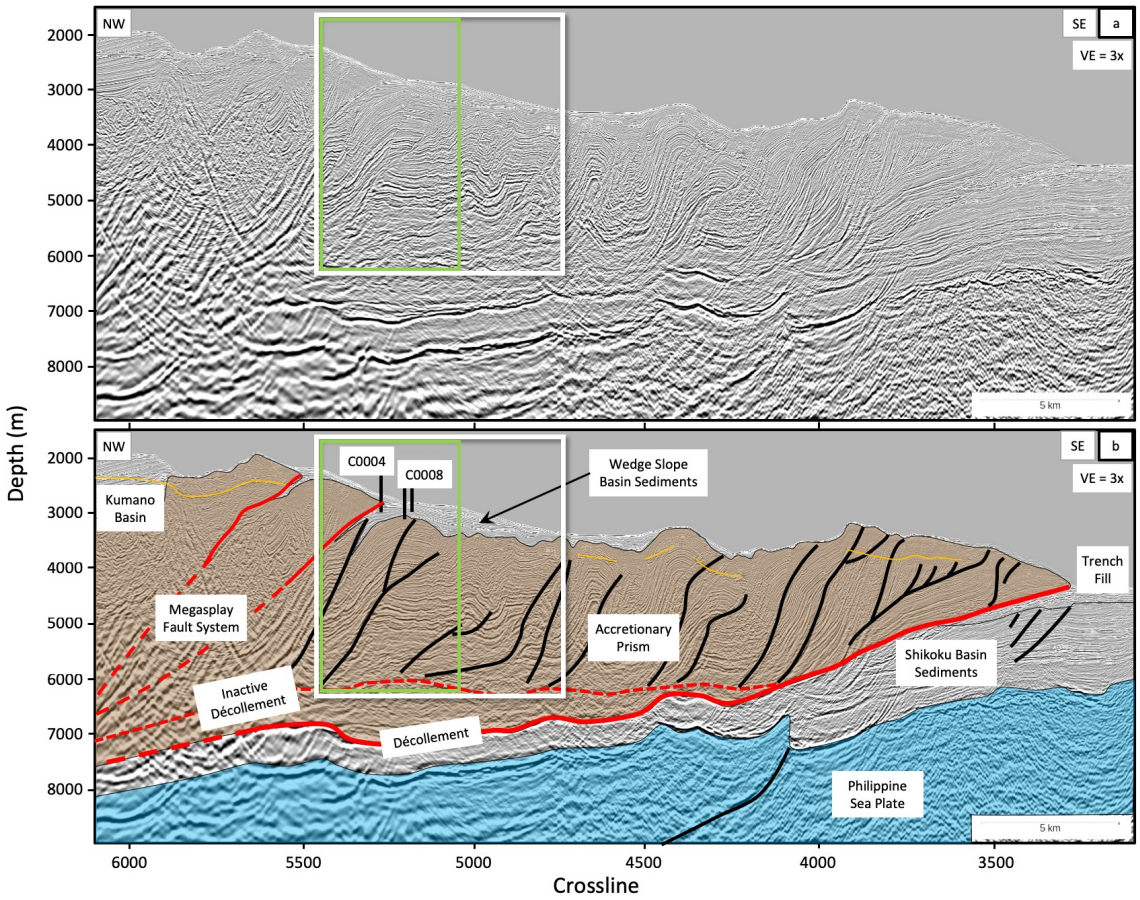

Fig. 4.2. Accretionary prism at IL2675. Location shown in Fig. 4.1. (**a**) Uninterpreted seismic cross section of prism. (**b**) Interpreted seismic cross section of prism. White box indicates the study area for this paper while the green box indicates the boundary of the kinematic restoration. Heavier black lines are major faults and orange lines are bottom simulating reflectors (BSR). C0004 and C0008 show sediment core locations (Fig. 4.4).

Methods

A 3D kinematic structural restoration is carried out via Midland Valley's *MOVE* software suite (Midland Valley Exploration Ltd., 2018). Significant stratigraphic and structural horizons are initially interpreted from the 3D seismic reflection volume and interpretations from previous studies (e.g., Moore *et al.*, 2007; Strasser *et al.*, 2009; Strasser *et al.*, 2011; Kimura *et al.*, 2011). Timing of movement along faults and deposition rates are constrained from data obtained by sediment core analyses from IODP Expeditions 316 and 338 (Expedition 316 Scientists, 2009b, c; Moore *et al.*, 2014). As the kinematic

restoration takes place, erosion (e.g., slope failure) is restored manually via geometric interpolation between the eroded and onlap surfaces.

3D Volume

The full 3D seismic survey (Moore *et al.* 2009) covers roughly 12 km x 56 km extending from the Kumano Basin seaward to the frontal thrust in the dip direction (Fig. 4.1, 4.3). Acquisition occurred aboard the M/V *Nordic Explorer* during April-May 2006 under contract by Petroleum Geo-Services (PGS), utilized two air gun arrays (totaling 51 L or 3090 in^3) fired alternately at 37.5 m shot intervals, and four 4500 m long receiver cables spaced 150 m apart with 360 receiver groups at 12.5 m spacing. This geometry yielded eight source-receiver common midpoint (CMP) lines per sail line at 37.5 m spacing (Moore *et al.*, 2009). The interval between lines and cross lines of the resulting dataset is 18.75 m and 12.5 m, respectively. The vertical resolution is ~5-7 m near the seafloor, degrading to ~10-20 m at depths near 1400 meters below seafloor (mbsf; Moore *et al.*, 2009). Standard pre-processing to reduce noise preceded pre-stack depth migration (PSDM) and produced a clear seismic image in depth (Moore *et al.*, 2009).

Core Data

Coring of the trench slope sediments was accomplished on IODP Expeditions 316 and 338 (Expedition 316 Scientists, 2009a, b, c; Moore *et al.*, 2014) aboard the D/V *Chikyu*. The cored intervals consist primarily of hemipelagic mud interbedded with several MTDs, sandy/silty turbidites, and volcanic ash (Fig. 4.4). Biostratigraphic and magnetostratigraphic dates were obtained by Expedition 316 Scientists (2009b, c). Here, we chose to use the average date as determined by the two dating methods to provide a single target date for our reconstructions. For a more detailed analysis of the core data see Strasser *et al.* (2011), Expedition 316 Scientists (2009b, c), and Moore *et al.* (2014).

Structural Restoration

A kinematic structural restoration of three 2D cross sections oriented approximately across strike of the MS are performed stepwise using the structural geology software suite *MOVE* (Midland Valley Exploration Ltd., 2018). We utilize 2D tri-shear and simple

shear geometric algorithms to restore interpreted cross sections. A trial and error approach is taken to determine the most appropriate tri-shear deformation parameters for successful restoration of fault displacement and horizon geometry. These parameters include displacement, tri-shear angle, tri-shear angle offset, tri-shear apex, and propagation to slip (p/s) ratio (Allmendinger, 1998; Allmendinger *et al.*, 2004). This approach has also been successfully used in other tri-shear restoration models in convergent margin settings (Boston *et al.*, 2016; Ghisetti *et al.*, 2016). It is important to note that, while admissible, the cross sections cannot be fully balanced due to a lack of layer-cake stratigraphy. Additionally, depositional layers were not deposited on a completely horizontal surface and large volumes of material have been eroded and transported away from the study area.

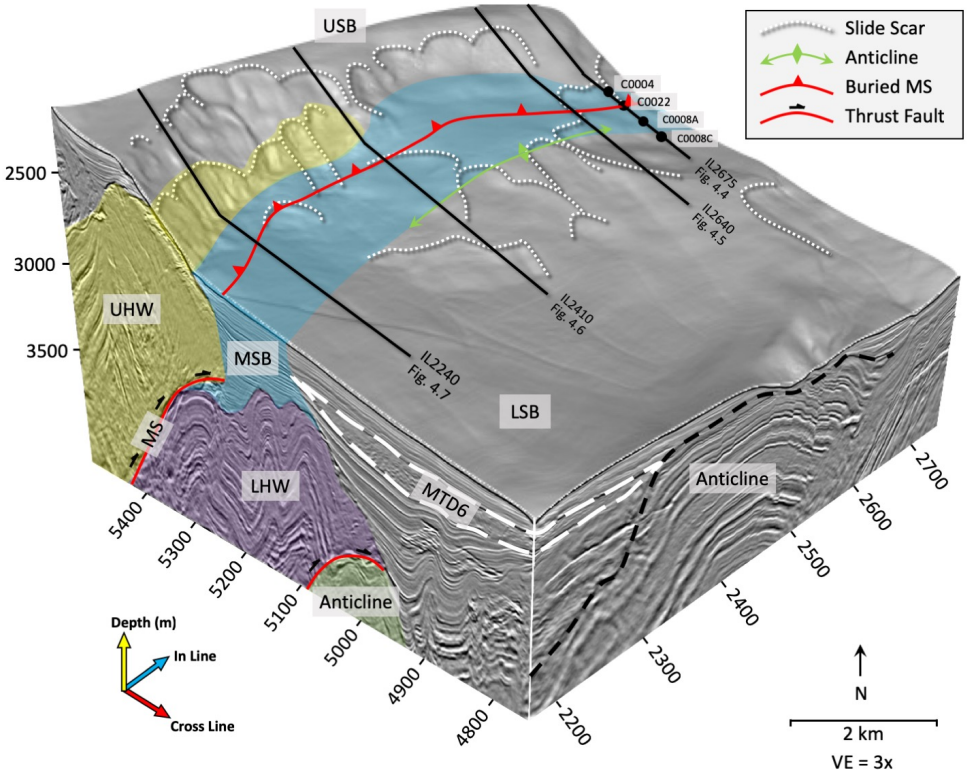

Fig. 4.3. Seismic cube. Three-dimensional seismic cube of the study area extracted from the 3D survey of the M/V *Nordic Explorer* showing prominent structural and surficial features. Note the spatial correlation between slide scars and the buried anticline (green line) and landslide scars and the UHW. IODP drill sites along IL2675 are shown for reference. UHW – Upper hanging wall; LHW – Lower hanging wall; USB – Upper slope basin; MSB – Middle slope basin; LSB – Lower slope basin; MS – Megasplay; MTD6 – Mass transport deposit 6 identified by Strasser et al. (2011).

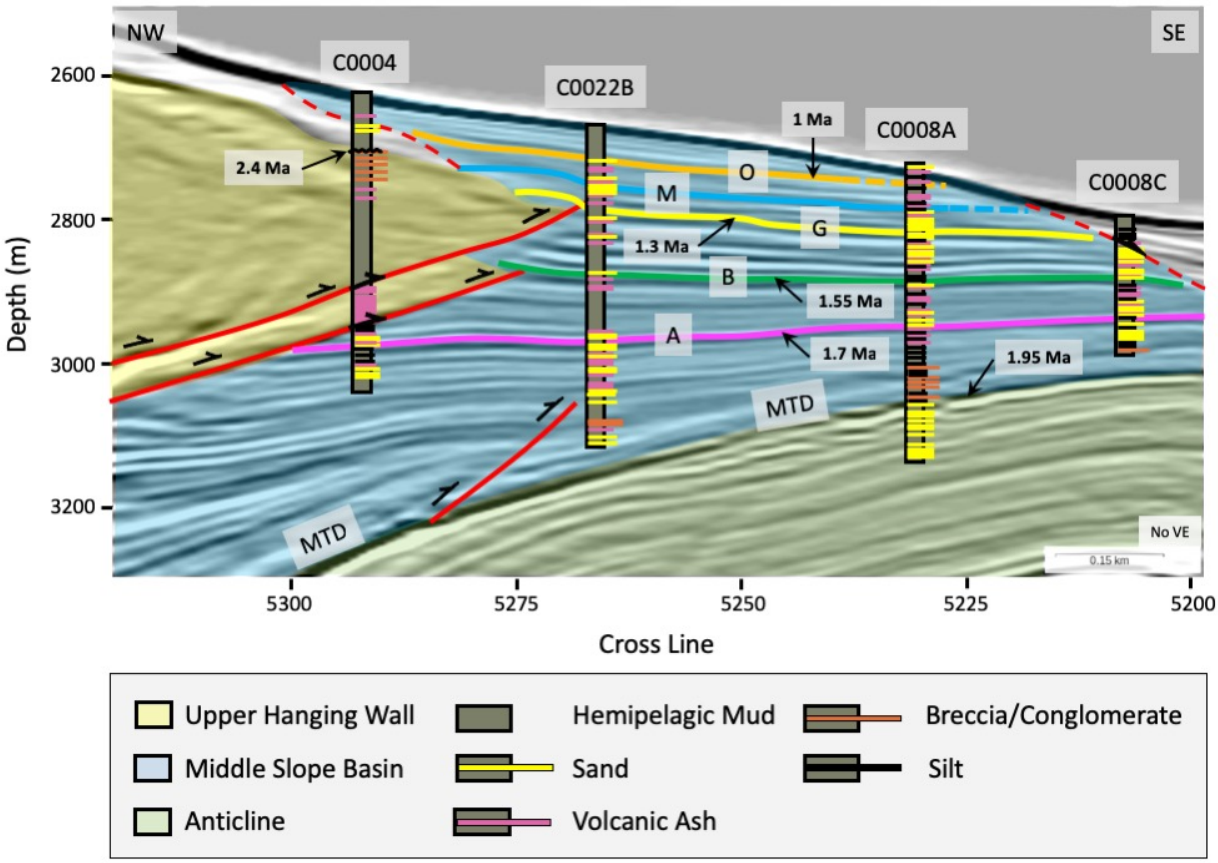

Fig. 4.4. Core data. Interpretation of seismic inline IL2675 crossing IODP Sites C0004, C0022B, C0008A, and C0008C. The location is shown in Fig. 4.3. Lithostratigraphic sections of drill sites are overlain after Expedition 316 Scientists (2009c, 2009d). A, B, G, O (after Strasser et al. (2011)), and M indicate key seismic stratigraphic horizons. Ages are biostratigraphic ages as determined by Expedition 316 Scientists (2009a, b, c).

Inline geometry is used as the primary direction for structural restoration. Although this is not exactly perpendicular to the strike of the MS or other structures within the study area, there is little difference between the inline and perpendicular geometries. Because the underlying stratigraphy does not notably change between these geometries, we chose to utilize the inline geometry as it allows for a more comprehensive view of the entire 3D volume.

The along strike boundaries of our restoration are inlines 2640 in the NE and 2240 in the SW of the 3D volume. The landward boundary is delineated by a smaller slope basin that

overlies the upper hanging wall. While this basin surely influences the development of the middle slope basin (MSB), there are no traceable horizons between the two. Therefore, we chose not to include it in the restorations. The seaward boundary is an onlap surface identified by Strasser *et al.* (2011) and Kimura *et al.* (2011). They explained that this surface represents a slip zone onto which younger sediments onlap, causing the apparent offset in the stratigraphic horizons between the MSB and lower slope basin (LSB). This is further supported by the numerous slope failures identified in the bathymetric data that spatially correlate with the failure surface (Fig. 4.3). Because this surface represents a consistent parameter throughout the evolution of our restoration (constant slope failure) and because it lies above the seaward flank of the anticline, we believe it to be an appropriate boundary for each cross section.

Many faults and folds are either simplified or not included in our restoration due to their deformation being below or near the resolution of our seismic data. For instance, the internal thrust faults that likely exist within the upper hanging wall (UHW; Fig. 4.3) are too numerous, complex, and unresolvable to fully map. To account for this, we map prominent internal thrusts (UI) in each cross section based on both the 3D volume and the shape of the UHW top surface (Figs. 4.5, 4.6, 4.7). These thrusts represent the collective movement of all thrust faults within the UHW.

The anticline that spans the study area also presented several challenges to the restorations. While a reconstruction of the overall anticline is attempted, a full, internal reconstruction is beyond the scope of this paper. Normal faults (e.g., Strasser *et al.*, 2009; Kimura *et al.*, 2011) on top of the structure are not restored. These faults, while important indicators of anticline activity, are unimportant in the overall kinematic restoration. Due to the anticline's high degree of deformation, there are few instances of horizons being traceable between cross sections, therefore, we interpret most of the anticline in each cross section independently. Additionally, the timing of displacement along faults within the anticline cannot be constrained with the available core data. We thus restore this displacement as needed to correct otherwise unaccounted for deformation within the overlying horizons.

Due to their unique geometry, we restore slope failures manually by using the geometry of overlying horizons that have been deformed but have not yet failed. For instance, to restore horizons A and B against the upper hanging wall, we attempt to recreate the same type of deformation as seen in horizons G and M by using their geometries as templates (Fig. 4.5). After a horizon and movement along a fault are restored, imperfections in the geometry of the horizon contacts can be attributed to errors in interpolation to create said contacts.

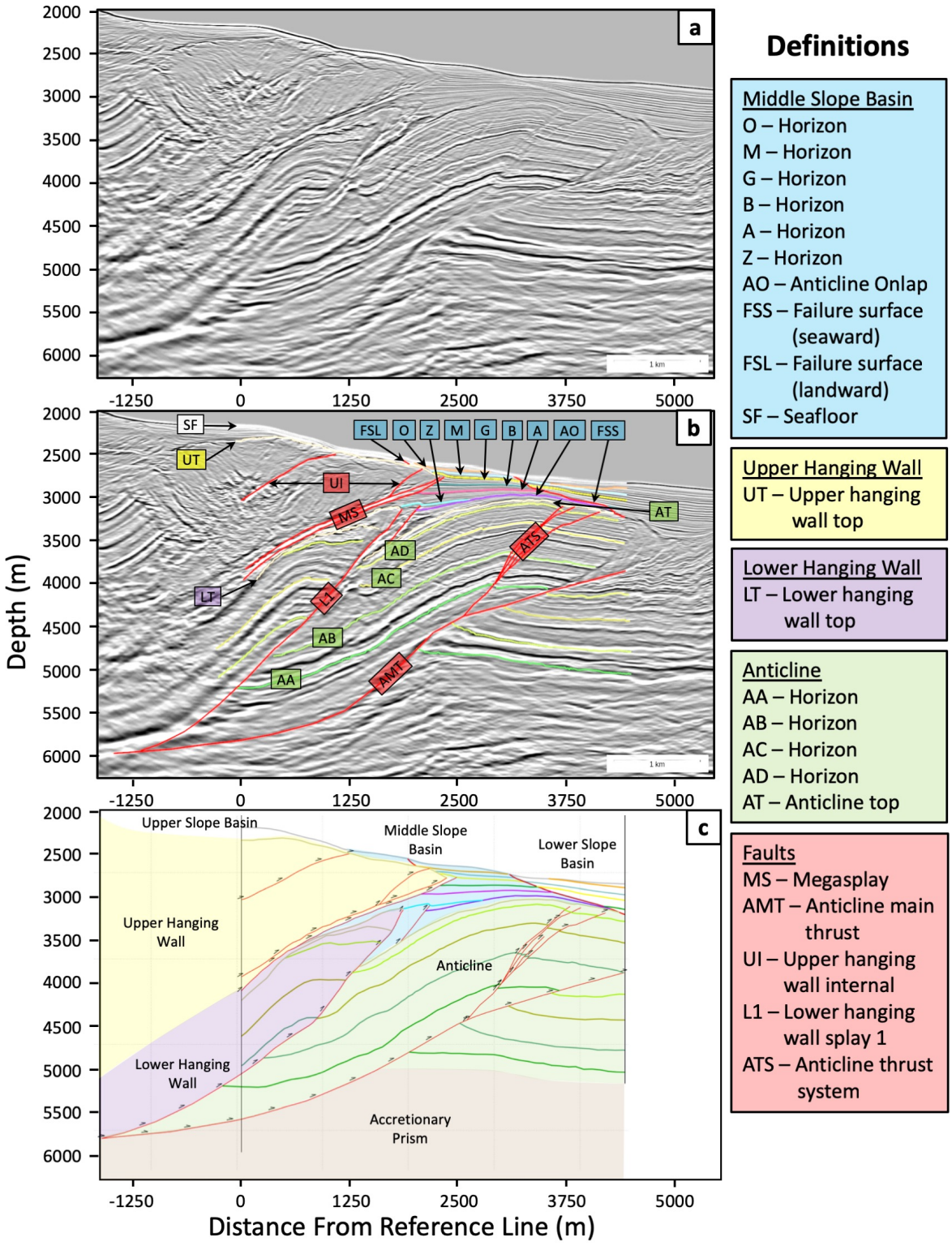

Fig. 4.5. IL2640. (**a**) Uninterpreted seismic cross section. (**b**) Interpreted seismic cross section indicating all key faults and horizons. (**c**) Representation of the cross section showing all key faults, horizons, and major structural blocks.

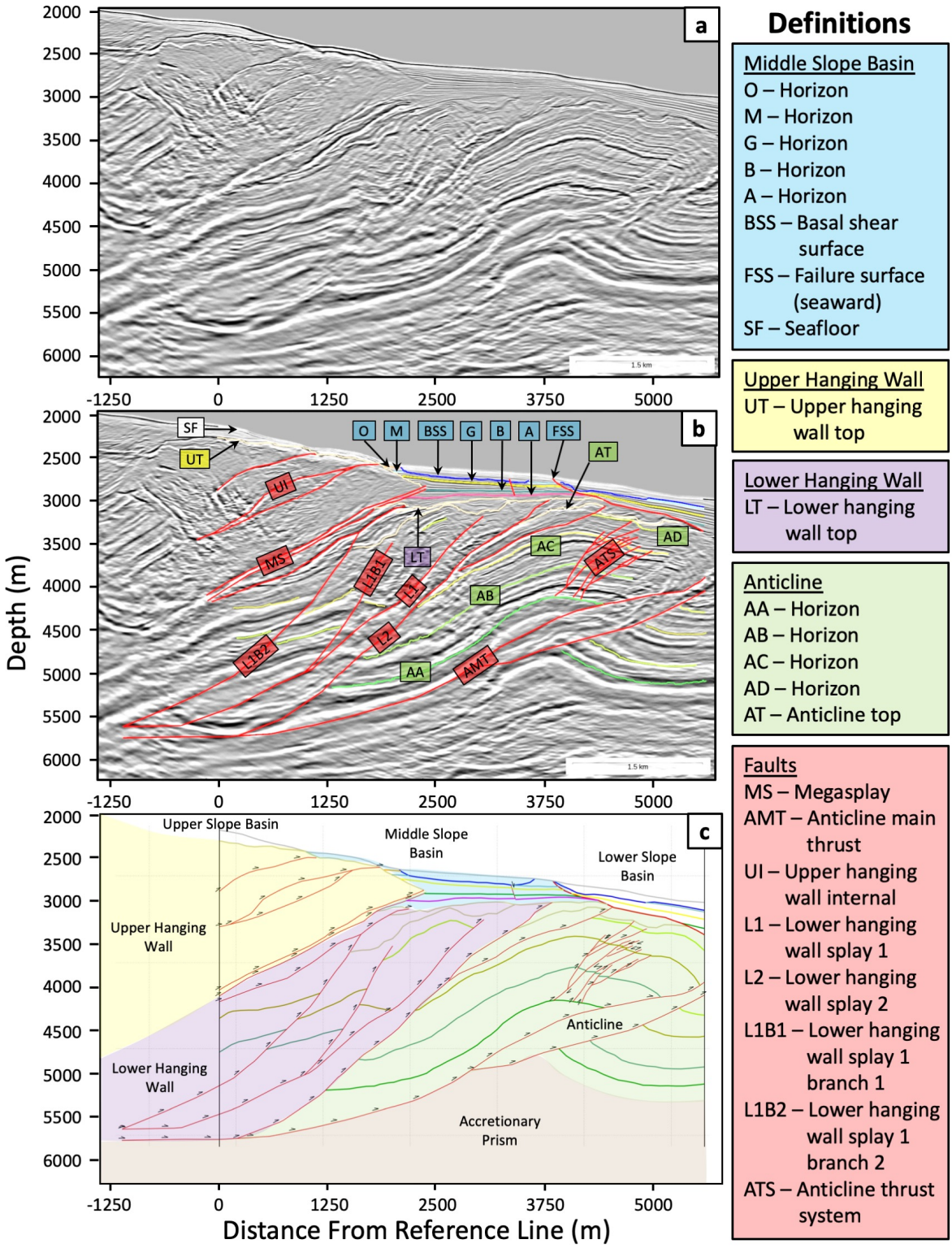

Fig. 4.6. IL2410. (**a**) Uninterpreted seismic cross section. (**b**) Interpreted seismic cross section indicating all key faults and horizons. (**c**) Representation of the cross section showing all key faults, horizons, and major structural blocks.

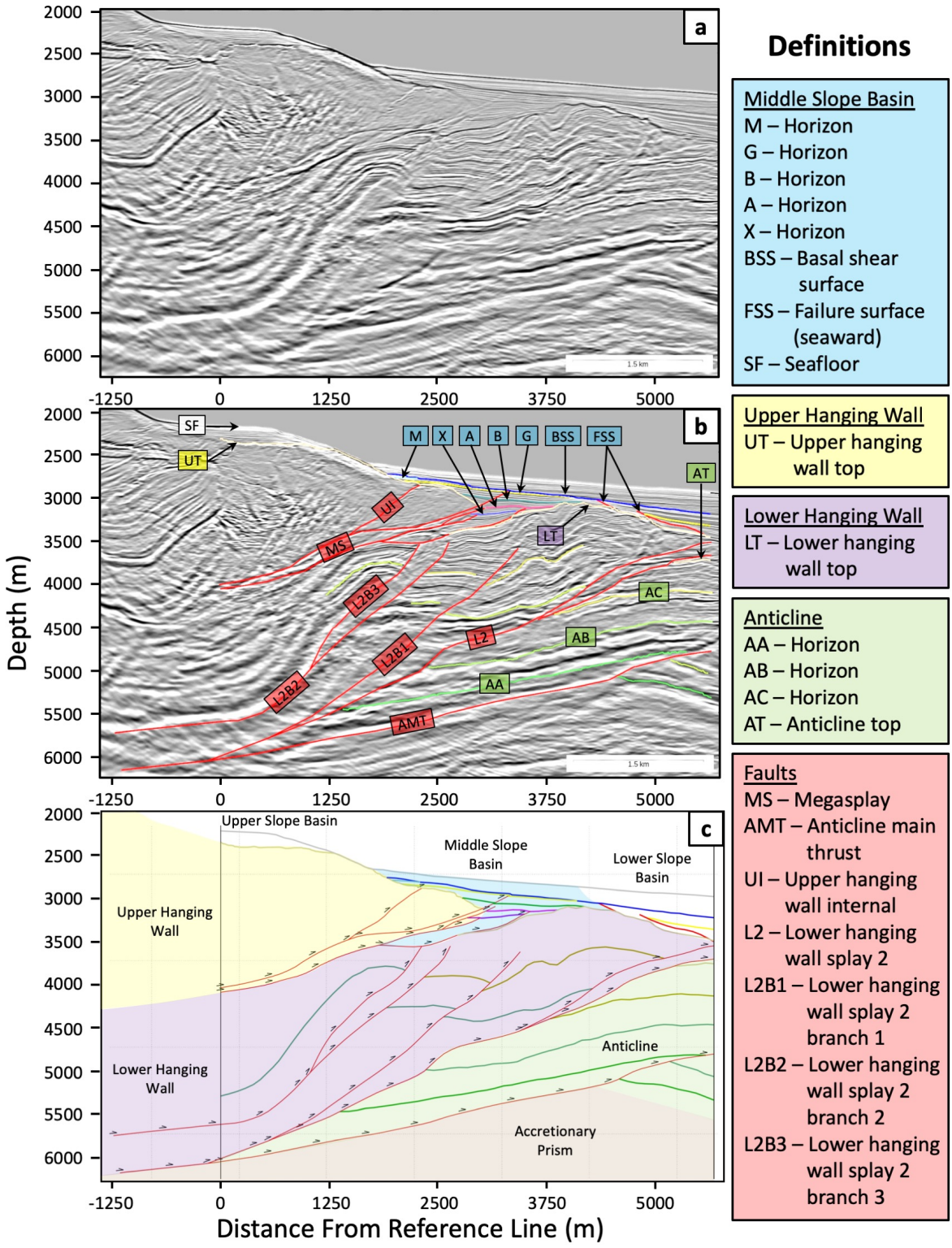

Fig. 4.7. IL2240. (**a**) Uninterpreted seismic cross section. (**b**) Interpreted seismic cross section indicating all key faults and horizons. (**c**) Representation of the cross section showing all key faults, horizons, and major structural blocks.

Results

We successfully restored each cross section to age tie points from the IODP sediment cores and were able to approximate and restore deformation prior to 1.95 Ma based on horizon geometry within the anticline.

IL2640

Inline 2640 (Fig. 4.5) is in the eastern most portion of the study area ~650 m west of the IODP drill sites. This represents the thickest deposit of MSB sediments and the largest displacement within the UHW via the MS. We restore an overall shortening of 5,516 m, with 89% of this occurring between 1.7 – 2.4+ Ma. Much of the inline displacement is accommodated along the anticline main thrust (AMT; 47%) and MS (38%). Deformation within the lower hanging wall (LHW) and anticline is at a minimum in this cross section. This suggests that most of the deformation here is accommodated along major faults such as the MS.

IL2410

Inline 2410 (Fig. 4.6) is in the middle of the study area ~4300 m W of IL2640 and ~3200 m E of IL2240. This cross section represents a transition of displacement from primary fault structures to fault branches and more LHW and anticline deformation. We restore an overall shortening of 4,841 m, with 90% of that occurring between 1.7 – 2.4+ Ma. Inline displacement is accommodated mostly along the AMT (49%) followed by the lower hanging wall fault system (LHWF; 26%) and MS (22%). The LHW becomes a more prominent feature that begins to override the anticline. Fault zones, where there are no traceable horizons, are also present both within the LHW and anticline. Additionally, thrust faults that cut the tops of both the LHW and the anticline are identified in this cross section. Although these features can be traced in the 3D volume, they do not continue far enough to be identified in either of the other cross sections.

IL2240

Inline 2240 (Fig. 4.7) is in the western portion of the study area ~3200 m W of IL2410. This cross section represents the highest degree of LHW and anticline deformation and

contains the fault we believe to be the primary trigger of MTD6 (Strasser *et al.*, 2011). We restore an overall shortening of 5,680 m, with 96% of that occurring between 1.7 – 2.4+ Ma. Inline displacement is accommodated mostly along the LHW (64%) while the MS exhibits the least displacement (11%). The LHW is the prominent structural feature here, overriding the anticline while the basal shear surface of MTD6 dominates the MSB.

3D Observations

Overall (Fig. 4.8), we observe most fault displacement and prism shortening occurring in the early stages of MS development and anticline deformation (1.7 – 2.4+ Ma). The AMT accounts for almost all (90%) of the displacement between 1.95 – 2.4+ Ma, after which the MS system initiates and begins to dominate. From 1.95 – 1.7 Ma we restore ~1,838 m, ~1,195 m, and ~3,920 m of shortening between IL2640, IL2410, and IL2240 respectively. However, shortening is accommodated differently between each cross section. Most of the shortening is along the MS (66%) at IL2640. Along strike to the SW, shortening is transferred deeper into the prism toward IL2240 where the LHWF accommodates the most shortening (89%). The movement along thrusts that cut the tops of the LHW and anticline at IL2410 (Fig. 4.8e & f) help support this observation.

There is a notably large decrease in displacement from 1.7 – 1.55 Ma along all cross sections. Except for 55 m of displacement within the LHW, all displacement during this period occurs within the UHW. As with the previous 250Ky, IL2640 contains the most shortening and displacement (357 m and 370 m, respectively) decreasing along strike to IL2240 (80 m and 115 m, respectively). This trend continues throughout the remainder of the restoration, helping to explain the degree to which the UHW overrides the MSB at IL2640.

From 1.55 Ma – present, most displacement and shortening remain in the UHW and decrease from NE to SW. IL2640 shortens a total of 267 m while IL2410 and IL2240 shorten 207 m and 147 m respectively. Notable displacements occur within the UHW at 1.55 – 1.3 Ma and along the MS at 1 – 0.44 Ma. Between 1.55 – 1.3 Ma an internal thrust (UI1) within the UHW initiates (Kimura *et al.* 2011) with a displacement of 75 m.

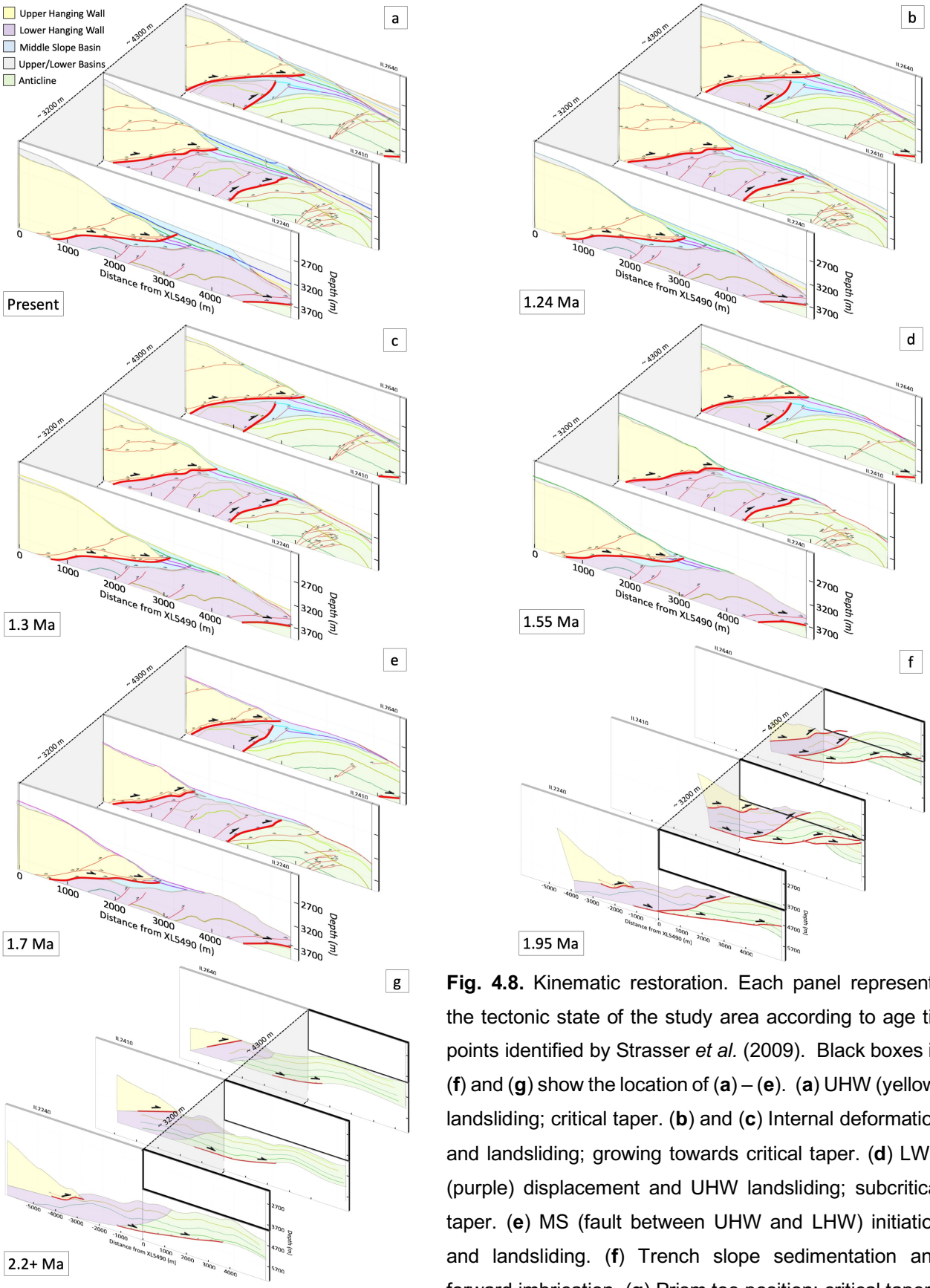

Fig. 4.8. Kinematic restoration. Each panel represents the tectonic state of the study area according to age tie points identified by Strasser *et al.* (2009). Black boxes in (**f**) and (**g**) show the location of (**a**) – (**e**). (**a**) UHW (yellow) landsliding; critical taper. (**b**) and (**c**) Internal deformation and landsliding; growing towards critical taper. (**d**) LWH (purple) displacement and UHW landsliding; subcritical taper. (**e**) MS (fault between UHW and LHW) initiation and landsliding. (**f**) Trench slope sedimentation and forward imbrication. (**g**) Prism toe position; critical taper.

While there is no evidence of fault displacement outside of this period, we restore movement along UI1 periodically to represent movement within the entirety of the UHW. MS3 slips at ~0.9 Ma (Kremer *et al.*, 2017) with a restored displacement of 21 m. We believe this directly correlates with the emplacement of MTD6 as proposed by Strasser *et al.* (2011).

Discussion

Our restoration points to numerous influences on the overall development of the MSB. Movement along the MS and deformation of the LHW and regional anticline could be driven by regional subsurface geology, the prism attempting to maintain critical taper, subduction processes, and/or slope failures.

Accretionary Wedge Shortening

Our reconstruction estimates a minimum shortening that accounts for roughly 5.7 km (~4.3 – 6.5%) of the total plate convergence rate (4 – 6 cm yr^{-1}, or 88 – 132 km) since ~2.2 Ma. However, this estimate accounts only for seismic scale faulting. Other quantifiable factors that can accommodate shortening within an accretionary wedge include sub-seismic scale deformation (up to 30 – 50%; e.g., Mitra, 1994; Koyi, 1995; Koyi et al., 2004) and de-watering and compaction (up to 40%; Moore et al., 2011). Taking these into account, total shortening across the entire wedge due to fault displacement is between 8.8 – 26.4 km and 13.2 – 39.6 km. It is unlikely that our study area constitutes the majority of fault displacement across the entire wedge as it accounts for only 4.5 km (~13%) of the prism as measured across strike. Therefore, we choose to assume that a maximum of ~70% of the plate convergence is accommodated by sub-seismic scale deformation and de-watering and compaction. Under this assumption, the total plate convergence accommodated by fault displacement is 26.4 – 39.6 km. Our study area then represents 14.4 – 21.6% (5.7 km) of the total plate convergence. This means that there is another 8.4 – 15.6% of total shortening that is unaccounted for between our reconstruction, sub-seismic scale deformation, and de-watering and compaction. The most likely explanations for this difference are seismic slip along the décollement (e.g., Ujiie and Kimura, 2014), forward propagation of the décollement (e.g.,

Morgan and Karig, 1995), reactivation of buried faults (Moore et al., 2015), unquantifiable errors within the chosen tri-shear parameters, and deformation that occurs outside the plane of the 2D restorations.

Anticline Formation

The general formation of the anticline in our restoration is explainable using critical taper theory and the history of the Nankai accretionary prism. Prior to ~2.2 Ma, when the study area was in the prism toe position (Fig. 4.8g), the entire prism was likely at critical taper as evidenced by in-sequence forward imbrication (Davis *et al.*, 1983; Strasser *et al.*, 2009). This may have initiated the AMT. Heavy trench slope sedimentation starting between ~2.06 – 1.6 Ma (Underwood & Moore, 2012; Buchs *et al.*, 2015) and subsequent surface denudation between ~1.62 – 1.24 Ma then caused a subcritical taper (Bigi *et al.*, 2010; Alves *et al.*, 2014). This permitted the prism to grow back toward critical taper via internal faulting (Davis *et al.*, 1983) such as we restore along both the MS and LHW fault system between ~ 1.95 – 1.24 Ma. Critical taper continued to reestablish via the formation of the Kumano Basin between ~1.3 – 1 Ma (Gulick *et al.*, 2010) by movement along the MS fault system somewhere outside of our study area. With critical taper reestablished, the prism again grew via forward imbrication from ~1 Ma – present with minimal internal faulting along the MS and within our study area.

While the anticline presently shows signs of activity (Fig. 4.9), the AMT shows no signs of displacement since ~1.95 Ma when the MS initiated (Moore *et al.*, 2007). Therefore, we infer that the current anticline activity is contained within the anticline itself and is the result of compressional stress imparted by the UHW and LHW and uplift as the prism grows. This interpretation is supported by our restoration, the orientation of faults within the anticline, and by its break-backward imbricate structure as shown in Fig. 4.9 (McClay, 1992; Shaw *et al.*, 1999). After movement along the AMT ceases due to continued forward imbrication of the accretionary prism, an incipient fault ruptures along the same basal detachment (the AMT) landward of the initial thrust fault resulting in the LHW. All three cross sections show at least one break-backward imbricate branch of the AMT with increasing faulting and complexity to the SW. We attribute both the faulting and its

increasing complexity to the structure of the anticline seaward of the study area (right side of Fig. 4.9a, b, c). The differences in AMT angle and structure of the seaward anticline, acting as a backstop to anticline growth along the AMT, permit break-backward faulting to occur. Because the angle of the AMT decreases to a point where it projects below the crest of the seaward anticline in the SW, break-backward faulting is more predominant in the SW than in the NE.

The anticline's structural variability and resultant LHW are major influences on the depth of the MSB. At IL2640, accommodation space is created between the anticline's crest and the tip of the MS because of the anticline's seaward movement along the AMT. The UHW then overthrusts the sediments as fault displacement along the AMT slows and transfers to the MS. Less accommodation space is created at IL2410 than at IL2640 as there is less displacement along the AMT. Additionally, displacement along the LHW fault system places the crest of the LHW directly beneath the MSB, filling the accommodation space. Accommodation space increases toward IL2240 where the LHW propagates the furthest seaward thanks to the largest displacement along its fault system. This leads to increased deformation and compression at the crest of the LHW. This creates an anticline-like structure (Fig. 4.9c) and accommodation space much like the anticline at IL2640. As a result, sediment thickness is at a minimum in the middle of the study area (450 m at IL2410; Fig. 4.9b) with increasing thicknesses toward the NE and SW boundaries (620 m at IL2640; Fig. 4.9a; 580 m at IL2240; Fig. 4.9c).

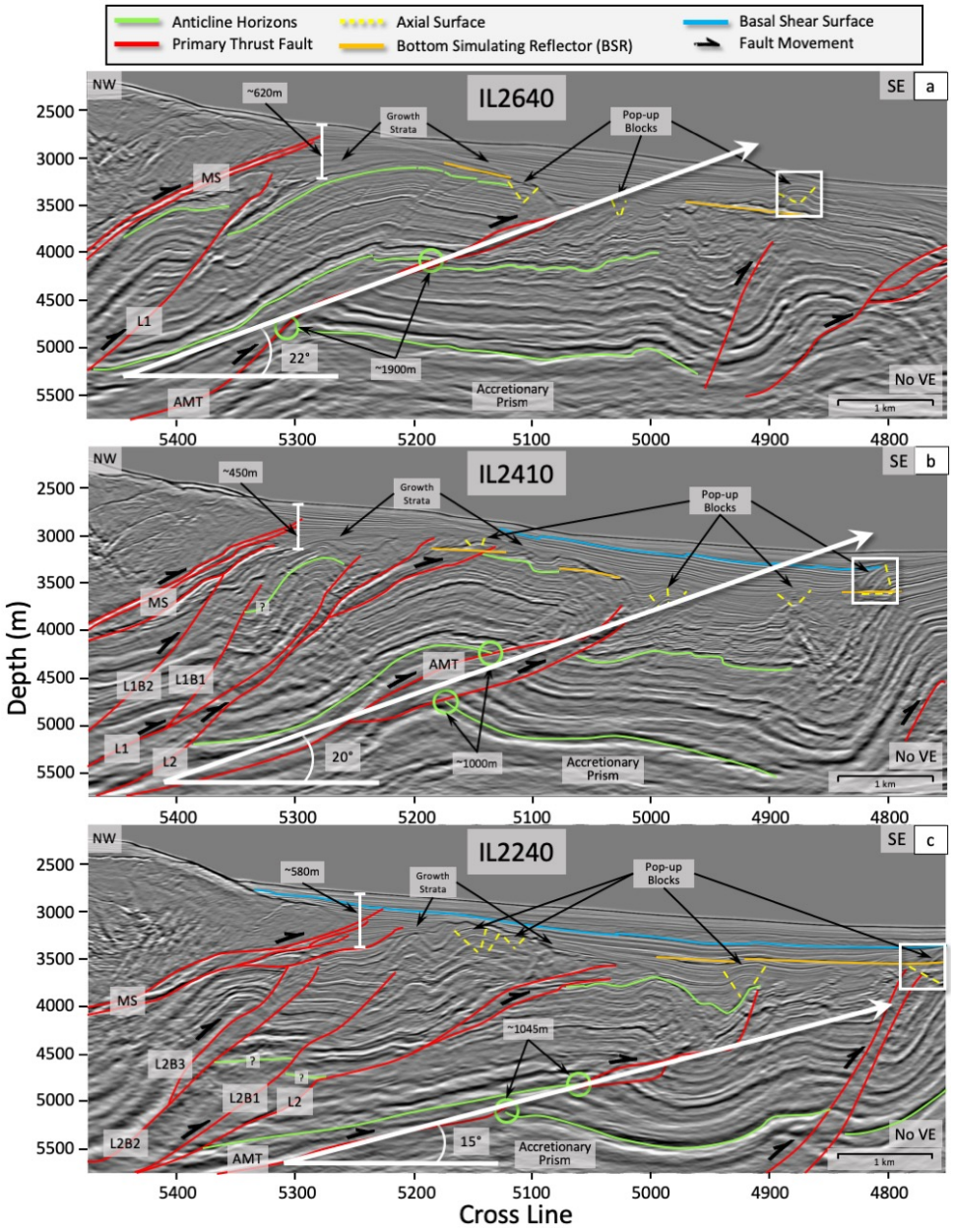

Fig. 4.9. Anticline regional structure. Comparison of the anticline structure from the landward most boundary of the restoration seaward to the following imbricate thrust and resultant anticline. White lines indicate AMT thrust vector, white boxes indicate pop-up blocks at the apex of the seaward anticline's kink bend fold, and green circles indicate where horizon AA from the restoration meets the AMT. Question marks indicate horizons that were inferred from surrounding seismic horizons and our restoration. AMT – Anticline Main Thrust; AA – Anticline A. (**a**) IL2640. The AMT angle is at its greatest here resulting in the fault trajectory projecting above the seaward anticline. Displacement along the AMT is at a maximum as a result. (**b**) IL2410. The AMT angle is reduced here causing the fault trajectory to approach the seaward anticline. Displacement along the AMT is reduced as this cross section represents a transition zone from primarily forward imbricate faulting (IL2640) to primarily break-backward imbricate faulting (IL2240). (**c**) IL2240. The AMT angle is at its lowest here causing the fault trajectory to fall below the seaward anticline. Compared to IL2640, displacement along the AMT is reduced and break-backward imbricate faulting dominates as a result.

Seamount Subduction

Moore *et al.* (2009) proposed that a large embayment to the W of the 3D survey at the toe of the prism is the likely result of small seamount subduction based on a nearby 2D seismic line (ODKM03-I; Taira *et al.*, 2005). Strike-slip faults located W of the 3D survey could be resultant bathymetric features of similar subduction (Fig. 4.1). While there are no clear strike-slip faults directly associated with the embayment (possibly due to the oblique subduction of the Philippine Sea Plate), these faults are found to be common features of seamount subduction in both sandbox experiments and along other subduction zones (Dominguez *et al.*, 1998; Dominguez *et al.*, 2000). The strike-slip faults would relieve compressional stress within the prism that would otherwise cause the MS to rupture in the W part of the study area. That these faults appear to clearly offset the seafloor indicates that they have likely been active since ~0.9 Ma. If displacement had ceased since ~0.9 Ma, there would be either a less pronounced bathymetric manifestation or they would be completely buried by MTD6. Because of this relative timing, it is reasonable to infer that displacement along these faults is a contributing factor to the lack of MS displacement in the W part of the study area since ~0.9 Ma.

Seamount subduction has also been proposed by Kimura *et al.* (2011) to explain the differences in strike between the imbricate thrust zone and the frontal thrust zone and the movement along the MS. The timing they suggest (~1.55 – 1 Ma) places this collision prior to those proposed by Moore *et al.* (2009). Such timing is consistent with regional bathymetry as the scar from the larger seamount to the NE (Fig. 4.1) displays signs of an infilled shadow zone (seamount is fully subducted) while the scars to the SE show clear reentrants (seamount is just subducted).

Slope Failures

Slope failures occur throughout the study area (Lackey *et al.*, 2018a, b) but can be broadly categorized into three groups based on their spatial correlation with the MSB's underlying structure. The first group is located above the onlap surface (Strasser *et al.*, 2011) on the seaward flank of the anticline (Fig. 4.3). This surface has been maintained through anticline growth (McClay *et al.*, 1999) and slope failures. As the anticline grows, normal

faulting associated with extensional stress at the anticline's crest both preconditions and causes slope failure as evidenced by MTDs in the LSB stratigraphy and the modern bathymetric scars.

The second group of failures occur along the flank of the UHW (Fig. 4.3). This surface is similar to the onlap surface on the flank of the anticline. It separates the MSB from the upper slope basin (USB) and is a surface on which slope failures continually occur as evidenced by both MSB stratigraphy (e.g. Expedition 316 Scientists, 2009a, b, c; Kimura *et al.*, 2011; Strasser *et al.*, 2011) and bathymetry (e.g. Moore *et al.*, 2009; Lackey *et al.*, 2018a, b). The cause of these failures, however, is likely different as the UHW is not growing like the anticline. Here, the flank of the UHW is steeper than the flank of the anticline. This over steepened condition is likely the primary factor in slope instability that precedes slope failure via MS displacement and faulting within the UHW.

The third group of slope failures occur because of the displacement along the MS. Here again there are multiple examples in both the stratigraphy (e.g. Expedition 316 Scientists, 2009a, b, c; Kimura et al., 2011; Strasser et al., 2011) and bathymetry (e.g. Moore et al., 2009; Lackey et al., 2018a, b). However, the most striking example is MTD6 as identified by Strasser et al. (2011). There is ~21 m of displacement along the MS at ~0.9 Ma. Tracing MS fault 3 (MS3) through the volume, the fault tip is localized between IL2280 and IL2177 to the area below the basal shear surface (BSS). At IL2240 (Fig. 7), MS3 clearly cuts horizons B, G, and MTD6's BSS with the same offset for each and without any growth structures detectable at the seismic scale. This suggests that the fault may have been created over a relatively short period of time after or coincident with the emplacement of MTD6 as proposed by Strasser et al. (2011).

Our restoration shows little to no displacement along the MS between ~1.3 – 1 Ma, contrary to Gulick *et al.* (2010). However, we do not believe that the interpretation of Gulick *et al.* (2010) is incorrect. Instead, we suggest that the shortening proposed between ~1.3 – 1 Ma that lead to the uplift of the outer forearc and development of the Kumano Basin is accommodated along branches of the MS that break further landward

than our study area (Fig. 4.2). The USB is also overthrust by a branch of the MS and is not included in our restoration of the MSB. Therefore, we suggest that while movement along the MS in our restoration is at a minimum between ~1.55 Ma – present, movement along more landward branches may be greater. Additional, broader scale restoration is needed to validate this conclusion, however.

Compaction

Lithostatic compaction and dewatering affect the sediment layers within the MSB but are not significant enough to include in the reconstruction. We modeled the lithostatic decompaction as a function of porosity using a Sclater-Christie relationship (Fig. 4.10; Sclater and Christie, 1980)

$$f = f_o(e^{-cy})$$

where f = porosity at depth y, f_o = surface porosity, c = porosity depth coefficient (km-1), and y = depth in km. We input porosities and depths from Expedition 316 Scientists (2009a, b, c) in an effort to determine an appropriate depth coefficient. However, we calculated that a coefficient > 1 km^{-1} is required to match the data. We then calculated a best fit line for the data to utilize in lithostatic decompaction calculations (Fig. 4.10) and observed a total change in depth between the present day and de-compacted seafloor of ~10.8 m, or 4% over the 270 m of available porosity data. This assumes that the vertical change is due solely to a loss of porosity. We believe this to be accurate as other available core data show an increase in bulk density from ~1.6 g/cm^3 to ~1.87g/cm^3 and a consistent grain density of ~2.96 g/cm^3 over the same depth interval (Expedition 316 Scientists, 2009a, b, c). Because this vertical change is near the vertical resolution of our seismic data (~10 m at 270 m depth; Moore *et al.*, 2009), we can exclude lithostatic decompaction from the reconstruction. However, it is worth noting that the cored data shows a porosity of 0.5 at 270 m compared to the calculated value of 0.59 utilizing the Sclater-Christie relationship. Comparing the two, we find that the Sclater-Christie curve (Sclater and Christie, 1980) utilizes a depth coefficient of 0.39 km^{-1} while the required depth coefficient to match the core data under strictly lithostatic conditions would be > 1

km^{-1}. This far exceeds the highest observed depth coefficient by Sclater and Christie (1980) (chalk at 0.71). We believe the porosity difference (0.09, or ~15%) between the Sclater-Christie relationship (Sclater and Christie, 1980) and the core data (0.09) is due to the added stress of horizontal compaction of the MSB sediments. Moore *et al.* (2011) demonstrated the significance of horizontal compaction in accretionary environments along the Muroto transect of the Nankai Trough. They concluded that horizontal shortening due to de-watering and compaction is ~40% within the accreted sediments. While the sediments within the MSB are deposited and not accreted, compaction still occurs because of the UHW and LWH displacements as evidenced by numerous small-scale thrust faults and folds within the MSB (Fig. 4.5, 4.6, 4.7). Therefore, we infer that the ~15% difference between calculated and observed porosities is due to horizontal compaction resulting from regional tectonic activity.

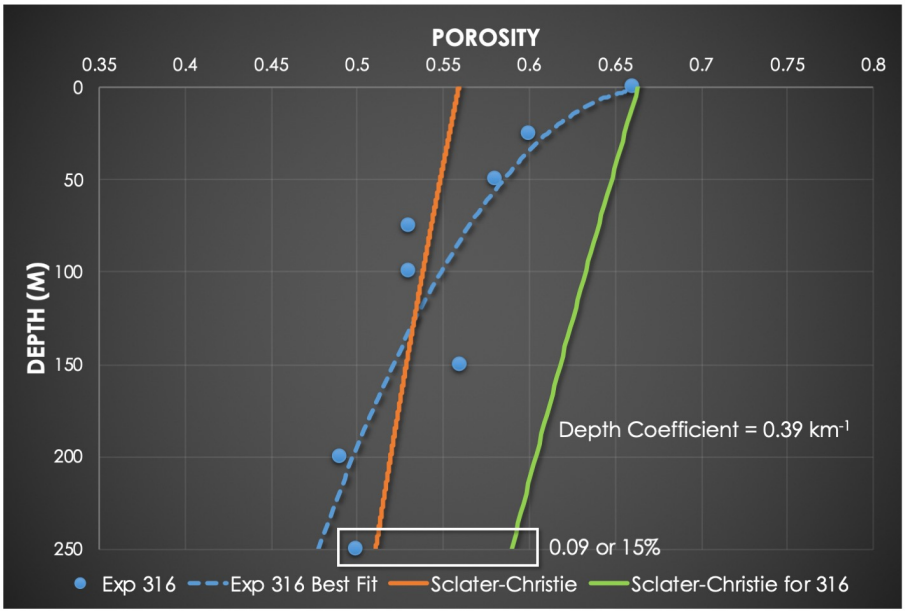

Fig. 4.10. Porosity data from Expedition 316 Scientists (2009a, b, c) (blue) compared to a standard Sclater-Christie curve (Sclater and Christie, 1980) and the application of the curve's depth coefficient to the cored data (Midland Valley Exploration Ltd., 2018) (orange and green respectively). The white box highlights the difference in porosity between the cored data (blue) and the projected value of the data (green) using a depth coefficient of 0.39 km^{-1}.

Conclusions

Three main conclusions are drawn from our 3D kinematic restoration of a trench slope basin on the Nankai accretionary prism:

1. The patterns of faulting that created and influenced the trench slope basin can be explained by changes in prism taper relative to critical (critical taper theory).

2. Development of the MSB is driven and influenced by the underlying anticline formation and deformation, regional seamount subduction, and slope failure above and within the basin.

3. Uplift of the outer forearc that formed the Kumano Basin was likely accommodated on the MS fault system landward of the study area.

Acknowledgements

The 3D data reprocessing was supported by the Japan Society for the Promotion of Science (JSPS) through a KAKENHI Grant-in-Aid for Scientific Research S (JP15H05717), and by the Ministry of Education, Culture, Sports, Science, and Technology (MEXT) through management expense grants at the Research and Development Center for Ocean Drilling Science (ODS) and the Center for Deep Earth Exploration (CDEX) of Japan Agency for Marine-Earth Science and Technology (JAMSTEC). We thank Paradigm Geophysical and Midland Valley for making their software available to us.

CHAPTER 5
CONCLUSIONS AND FUTURE WORK

We set out to better understand the mechanisms by which landsliding is distributed and initiated along the Nankai accretionary prism off southwest Japan. Overall, we believe that these goals have been met. Through a robust examination of the seafloor, via high resolution bathymetric data, we were able to catalog an unprecedented number of landslide scars along the prism and correlate them to surficial faulting. Because of the detailed analysis of each scar, this data set can contribute to a larger global database of submarine landslides to help better understand their impacts of the seafloor and human populations.

Our 3D investigation of a nested series of landslides that occurred from ~1 – 0.44 Ma in the Kumano Basin highlights indirect links between earthquakes and landslides. Large scale, megathrust earthquakes are not required to relieve stress within the prism, meaning smaller earthquakes that sufficiently reorient the primary compressional stress within the prism could cause moderate to large landslides and, by consequence, tsunami. That the inter-seismic period of the earthquake cycle can lead to slope failure in forearc basins should be a key consideration in the construction of submarine and costal infrastructure due to the threat of landslide generated tsunami.

The tectonic reconstruction of the outer wedge and a spatially-correlated trench slope basin directly relates accretionary tectonics with slope failures and sedimentation. By back-striping movement along the megasplay and other prominent faults within the region, we have further constrained the timing and evolution of the prism. Now, we better understand how sedimentation is both affected by regional tectonics and how the prism responds to sedimentation throughout its evolution.

For future students that want to study accretionary environments, furthering this work should involve a broader scale reconstruction of the accretionary prism from the proto-thrust zone landward to the Kumano Basin incorporating all the data and conclusions to

date. Being one of the most heavily studied subduction zones on the planet, there are numerous studies along the entirety of the Nankai Trough, accretionary prism, and Kumano Basin to include IODP cores, seismic data, seismicity studies, sedimentation rates, etc. The integration of all these data, combined with the knowledge and skills gained within this dissertation, would permit such a broad reconstruction and provide an unprecedented view of subduction related tectonics on a regional scale.

It is my hope that these studies serve to further the understanding and knowledge of the Earth Sciences and allow future scientists to continue studying and broadening our knowledge of our planet.

REFERENCES

Abrahamson NA and Somerville PG (1996) Effects of the hanging wall and footwall on ground motions recorded during the Northridge earthquake. Bulletin of the Seismological Society of America, 86, S93–S99.

Allmendinger RW (1998) Inverse and forward numerical modeling of trishear fault-propagation folds, Tectonics, 17, 640–656.

Allmendinger RW, Zapata T, Manceda R, Dzelalija F (2004) Trishear kinematic modeling of structures, with examples from the Neuquén Basin, Argentina, in Thrust Tectonics and Hydrocarbon Systems, Am. Assoc. Pet. Geol. Mem. 82, edited by K. R. McKlay, pp. 356 – 371, Am. Assoc. of Pet. Geol., Tulsa, Okla.

Alves TM, Strasser M, Moore GF (2014) Erosional features as indicators of thrust fault activity (Nankai Trough, Japan). Marine Geology, 356, 5-18.

Ando M (1975) Source mechanisms and tectonic significance of historical earthquakes along the Nankai Trough, Japan. Tectonophysics, 27, 119-140.

Ashi J, Sawada R, Omura A, Ikehara K (2014) Accumulation of an earthquake-induced extremely turbid layer in a terminal basin of the Nankai accretionary prism. Earth, Planets and Space, 66.

Baba T, Cummins PR, Hori T, Kaneda Y (2006) High precision slip distribution of the 1944 Tonankai earthquake inferred from tsunami waveforms: Possible slip on a splay fault. Tectonophysics, 426, 119-134.

Bangs NL, Hornbach MJ, Moore GF, Park JO (2010) Massive methane release triggered by seafloor erosion offshore southwestern Japan. Geology, 38, 1019-1022.

Bardet JP, Synolakis CE, Davies HL, Imamura F, Okal EA (2003) Landslide Tsunamis: Recent Findings and Research Directions. In: Bardet JP, Imamura F, Synolakis CE, Okal EA, Davies HL (eds) Landslide Tsunamis: Recent Findings and Research Directions. Pageoph Topical Volumes. Birkhäuser, Basel, pp 1793-1809.

Bigi S, Di Paolo L, Vadacca L, Gambardella G (2010) Load and unload as interference factors on cyclical behavior and kinematics of Coulomb wedges: Insights from sandbox experiments. Journal of Structural Geology, 32, 28-44.

Bondevik S, Kaland PE, Svendsen JI, Johnsen G, Mangerud J (1997) The Storegga tsunami along the Norwegian coast, its age and runup. Boreas, 26, 29-53.

Bøe R, Hovland M, Instanes A, Rise L, Vasshus S (2000) Submarine slide scars and mass movements in Karmsundetand Skudenedfjorden, southwestern Norway: morphology and evolution. Marine Geology 167:147–165.

Buchs DM, Cukur D, Masago H, Garbe-Schönberg D (2015) Sediment flow routing during formation of forearc basins: Constraints from integrated analysis of detrital pyroxenes and stratigraphy in the Kumano Basin, Japan. Earth and Planetary Science Letters, 414, 164-175.

Bull S, Cartwright J, Huuse M (2009) A Review of Kinematic Indicators from Mass-Transport Complexes Using 3D Seismic Data. Marine and Petroleum Geology, vol 26, no 7, pp 1132-1151.

Caress DW, Chayes DN (1996) Improved processing of Hydrosweep DS multibeam data on the R/V Maurice Ewing. Marine Geophysical Researches, vol 18, pp 631-650.

Caress DW and Chayes DN (2008) MB-System: Open source software for the processing and display of swath mapping sonar data. http://www.mbari.org/data/mbsystem/.

Dahlen FA, Suppe J, Davis D (1984) Mechanics of fold-and-thrust belts and accretionary wedges: cohesive coulomb theory. Journal of Geophysical Research, 89, 10, 087-010, 102.

DeVore JR, Sawyer DE (2016) Shear Strength of Siliciclastic Sediments from Passive and Active Margins (0–100 m Below Seafloor): Insights into Seismic Strengthening. In: Lamarche G et al (eds) Submarine Mass Movements and their Consequences. Advances in Natural and Technological Hazards Research, vol 41, pp 173-180. Springer, Cham.

Dominguez S, Lallemand SE, Malavieille J, Von Huene R (1998). Upper Plate Deformation Associated with Seamount Subduction. Tectonophysics, 293.3-293.4, 207-24.

Farrell SG (1984) A dislocation model applied to slump structures, Ainsa Basin, South Central Pyrenees. Journal of Structural Geology 6:727–736.

Dominguez S, Malavieille J, Lallemand SE (2000) Deformation of accretionary wedges in response to seamount subduction: insights from sandbox experiments. Tectonics, 19(1):182–196.

Expedition 316 Scientists (2009a) Expedition 316 methods, in NanTroSEIZE Stage 1: Investigations of Seismogenesis, Nankai Trough, Japan, Proc. Integr. Ocean Drill. Program, 314/315/316.

Expedition 316 Scientists (2009b) Expedition 316 Site C0004, in NanTroSEIZE Stage 1: Investigations of Seismogenesis, Nankai Trough, Japan, Proc. Integr. Ocean Drill. Program, 314/315/316.

Expedition 316 Scientists (2009c) Expedition 316 Site C0008, in NanTroSEIZE Stage 1: Investigations of Seismogenesis, Nankai Trough, Japan, Proc. Integr. Ocean Drill. Program, 314/315/316.

Fitch TJ (1972) Plate convergence, transcurrent faults, and internal deformation adjacent to Southeast Asia and Western Pacific. Journal of Geophysical Research, 23, 4432-4460.
Frey Martinez J, Cartwright J, Hall B (2005) 3D seismic interpretation of slump complexes: examples from the continental margin of Israel. Basin Research 17:83–108.

Frey Martinez J, Cartwright J, James D (2006) Frontally confined versus frontally emergent submarine landslides: a 3D seismic characterisation. Marine and Petroleum Geology 23:585–604.

Gafeira J, Bulat J, Evan D (2007) The southern flank of the Storegga Slide: imaging and geomorphological analyses using 3D seismic. In: Lykousis V, Sakellariou D, Locat J (eds) Submarine Mass Movements and Their Consequences. Springer, Dordrecht, The Netherlands, pp 57–66.

Gee MJR, Gawthorpe RL, Friedmann JS (2005) Giant striations at the base of a submarine landslide. Marine Geology 214:287-294.

Gee MJR, Gawthorpe RL, Friedmann SJ (2006) Triggering and evolution of a giant landslide, offshore Angola revealed by 3D seismic stratigraphy and geomorphology. Journal of Sedimentary Research 76:9–19.

Ghisetti FC, Barnes PM, Ellis S, Plaza-Faverola AA, Barker DHN (2016) The last 2 Myr of accretionary wedge construction in the central Hikurangi margin (North Island, New Zealand): Insights from structural modeling, Geochem. Geophys. Geosyst., 17, 2661–2686.

Gulick SPS, Bangs NLB, Moore GF, Ashi J, Martin KM, Sawyer DS, Tobin HJ, Kuramoto S, Taira A (2010) Rapid forearc basin uplift and megasplay fault development from 3D seismic images of Nankai Margin off Kii Peninsula, Japan. Earth Planet Sci Lett 300(1–2):55–62.

Gutscher MA, Klaeschen D, Flueh E, Malavieille J (2001) Geology 29:379-382.

Holbrook WS, Lizarralde D, Pecher IA, Gorman AR, Hackwith KL, Hornbach M, Saffer D (2002) Escape of methane gas through sediment waves in a large methane hydrate province. Geology, 30, 467.

Ikari MJ, Strasser M, Saffer DM, Kopf AJ (2011) Submarine landslide potential near the megasplay fault at the Nankai subduction zone. Earth and Planetary Science Letters, 312, 453-462.

Ike T, Moore GF, Kuramoto S, Park JO, Kaneda Y, Taira A (2008) Variations in sediment thickness and type along the northern Philippine Sea Plate at the Nankai Trough. Island Arc, 17, 342-357.

Katz O, Einav R, Einat A (2015) Submarine Landslides and Fault Scarps along the Eastern Mediterranean Israeli Continental-slope. Marine Geology, 369, 100-115.

Kimura G, Kitamura Y, Yamaguchi A, Raimbourg H (2007a) Links among mountain building, surface erosion, and growth of an accretionary prism in a subduction zone -- An example from southwest Japan. Geol. Soc. Amer. Spec. Paper, 436.

Kimura G, Kitamura Y, Hashimoto Y, Yamaguchi A, Shibata T, Ujiie K, Okamoto SY (2007b) Transition of accretionary wedge structures around the up-dip limit of the seismogenic subduction zone. Earth and Planetary Science Letters, 255, 471-484.

Kimura G, Moore GF, Strasser M, Screaton E, Curewitz D, Streiff C, Tobin H (2011) Spatial and temporal evolution of the megasplay fault in the Nankai Trough. Geochemistry Geophysics Geosystems, 12.

Kimura G, Hashimoto Y, Kitamura Y, Yamaguchi A, Koge H (2014) Middle Miocene swift migration of the TTT triple junction and rapid crustal growth in southwest Japan: A review. Tectonics, 33, 1219-1238.

Kinoshita M, Tobin H, Ashi J, Kimura G, Lallemant S, Screaton EJ, Curewitz D, Masago H, et al. (2009) Proc. IODP, 314/315/316.

Kopp H and Kukowski N (2003) Backstop geometry and accretionary mechanics of the Sunda margin, Tectonics, 22(6), 1072.

Koyi H (1995) Mode of internal deformation in sand wedges. J. Struct. Geol., 17(2), 293–300.

Koyi HA, Sans M, Teixell A, Cotton J, Zeyen H (2004) The significance of penetrative strain in the restoration of shortened layers—Insights from sand models and the Spanish Pyrenees, in Thrust Tectonics and Hydrocarbon Systems. Am. Assoc. Pet. Geol. Mem. 82, edited by K. R. McKlay, pp. 207–222, Am. Assoc. of Pet. Geol., Tulsa, Okla.

Kremer K, Usman MO, Satoguchi Y, Nagahashi Y, Vadakkepuliyambatta S, Panieri G, Strasser M (2017) Possible climate preconditioning on submarine landslide along a convergent margin, Nankai Trough (NE Pacific). Progress in Earth and Planetary Science, 4, 20.

Lackey JK, Moore GF, Strasser M, Kopf A, Ferreira CS (2018a) Spatial and temporal cross-cutting relationships between fault structures and slope failures along the outer Kumano Basin and Nankai accretionary wedge, SW Japan. Subaqueous Mass Movements. Geological Society, London, Special Publications, 477.

Lackey JK, Moore GF, Strasser M (2018b) Three-dimensional Mapping and Kinematic Characterization of Mass Transport Deposits Along the Outer Kumano Basin and Nankai Accretionary Wedge, Southwest Japan. Prog. Earth Planet. Sci., Special Issue, v. 5/65.

Lastras G, Canals M, Hughes-Clarke JE, Moreno A, De Batist M, Masson DG, Cochonat P (2002) Seafloor imagery from the BIG'95 debris flow, western Mediterranean. Geology 30:871–874.

Lee HJ, Locat J, Boulanger E, Konrad JM (2004) Seismic strengthening, a conditioning factor influencing submarine lanslide development. Paper presented at the 57th Canadian Geotechnical Conference; 5th Joint CGS/IAH-CNC Conference, Quebec City, Quebec, Canada, October 24–27, 2004.

Lee HJ (2009) Timing of occurrence of large submarine landslides on the Atlantic Ocean margin. Marine Geology, 264, 53-64.

Locat J, Lee H, Kayen R, Israel K, Savoie M-C, Boulanger E (2002) Shear strength development with burial in Eel River margin slope sediments. Mar Georesour Geotechnol 20(2):111–135.

Lucente CC, Pini GA (2003) Anatomy and emplacement mechanism of a large submarine slide within a Miocene foredeep in the northern Apennines, Italy: a field perspective. American Journal of Science 303:565–602.

Martinsen OJ (1994) Mass movements. In: Maltman, A. (ed) The Geological Deformation of Sediments. Chapman and Hall, London, pp 127–165.

Masson DG, Hugget QJ, Brunsden D (1993) The surface texture of the Saharan debris flow deposit and some speculation on submarine debris flow processes. Sedimentology 40:583–598.

Matheus S, Sobiesiak G, Alsop I, Kneller B, Milana JP (2017) Sub-seismic scale folding and thrusting within an exposed mass transport deposit: A case study from NW Argentina. Journal of Structural Geology 96:176-191.

McAdoo BG, Pratson LF, Orange DL (2000) Submarine landslide geomorphology, US continental slope. Marine Geology, 169, 103-136.

McCarthy J and Scholl DW (1985) Mechanism of subduction accretion along the central Aleutian Trench, Geol. Soc. Am. Bull., 96, 691–701.

Midland Valley Exploration Ltd. (2018) *MOVE* software. Glasgow, United Kingdom. http://www.mve.com

Milkov AV (2004) Global estimates of hydrate-bound gas in marine sediments: how much is really out there? Earth-Science Reviews, 66, 183-197.

Mitra G (1994) Strain variation in thrust sheets across the Sevier fold-and-thrust belt (Idaho-Utah-Wyoming): Implications for section restoration and wedge taper evolution. J. Struct. Geol., 16(4), 585–602.

Miyakawa A, Saito S, Yamada Y, Tomaru H, Kinoshita M, Tsuji T (2014) Gas hydrate saturation at Site C0002, IODP Expeditions 314 and 315, in the Kumano Basin, Nankai trough. Isl. Arc 23:142-156.

Moore GF and Strasser M (2016) Large Mass Transport Deposits in Kumano Basin, Nankai Trough, Japan. Submarine Mass Movements and Their Consequences Advances in Natural and Technological Hazards Research, 371-379.

Moore GF, Shipley TH, Stoffa PL, Karig DE, Taira A, Kuramoto S, Tokuyama H, Suyehiro K (1990) Structure of the Nankai Trough Accretionary Zone from Multichannel Seismic-Reflection Data. Journal of Geophysical Research-Solid Earth and Planets, 95, 8753-8765.

Moore GF, Bangs NL, Taira A, Kuramoto S, Pangborn E, Tobin HJ (2007) Three-dimensional splay fault geometry and implications for tsunami generation. Science, 318, 1128-1131.

Moore GF, Park JO, Bangs NL, Gulick SP, Tobin HJ, Nakamura Y, Saito S, Tsuji T, et al. (2009) Structural and seismic stratigraphic framework of the NanTroSEIZE Stage 1 transect. Proc. IODP, 314/315/316, 1-46.

Moore GF, Saffer D, Studer M, Costa Pisani P (2011) Structural restoration of thrusts at the toe of the Nankai Trough accretionary prism off Shikoku Island, Japan: Implications for dewatering processes. Geochemistry, Geophysics, Geosystems 12.

Moore GF, Boston BB, Sacks AF, Saffer DM (2013) Analysis of normal fault populations in the Kumano Forearc Basin, Nankai Trough, Japan: 1. Multiple orientations and generations of faults from 3-D coherency mapping. Geochemistry, Geophysics, Geosystems, 14, 1989-2002.

Moore GF, Kanagawa K, Strasser M, Dugan B, Maeda L, Toczko S, Party I.E.S. (2014) IODP Expedition 338: NanTroSEIZE Stage 3: NanTroSEIZE plate boundary deep riser 2. Sci. Dril., 17, 1-12.

Moore GF, Boston BB, Strasser M, Underwood MB, Ratliff RA (2015) Evolution of tectonosedimentary systems in the Kumano Basin, Nankai Trough forearc. Mar Petrol Geol 67:604–616.

Moore JC, Klaus A, Bangs N, Bücker C, Brückmann W, Erickson S, Hansen O, et al. (1998) Consolidation patterns during initiation and evolution of a plate-boundary decollement zone: Northern Barbados accretionary prism. Geology, 26, 811-814.

Moore JG, Clague DA, Holcomb RT, Lipman PW, Normark WR, Torresan ME (1989) Prodigious Submarine Landslides on the Hawaiian Ridge. Journal of Geophysical Research-Solid Earth and Planets, 94, 17465-17484.

Morgan JK, Karig DE (1995) Decollement processes at the Nankai accretionary margin, southern Japan: Propagation, deformation and dewatering. J. Geophys. Res, 100, 15221–15231.

Nicholls RJ and Small C (2002) Improved Estimates of Coastal Population and Exposure to Hazards Released. Eos, Transactions American Geophysical Union, 83.28, 301.

Plafker G (1972) Alaskan Earthquake of 1964 and Chilean Earthquake of 1960: Implications for Arc Tectonics. Journal of Geophysical Research, 77, 901-925.

Prior DB and Coleman JM (1978) Disintegrating Retrogressive Landslides on Very-low-angle Subaqueous Slopes, Mississippi Delta. Marine Geotechnology, 3.1, 37-60.

Prior DB, Bornhold BD, Johns MW (1984) Depositional characteristics of a submarine debris flow. Journal of Geology 92:707–727.

Ruff L and Kanamori H (1980) Seismicity and the Subduction Process. Physics of the Earth and Planetary Interiors, 23.3, 240-252.

Sacks AF, Saffer DM, Fisher DM (2013) Analysis of normal fault populations in the Kumano Forearc Basin, Nankai Trough, Japan: 2. Principal axes of stress and strain from inversion of fault orientations. Geochem. Geophys. Geosyst. 14:1973-1988.

Saffer D, McNeill LC, Byrne T, Araki E, Toczko S, Eguchi N, Takahashi K, Expedition Scientists (2010) NanTroSEIZE Stage 2: NanTroSEIZE riser/riserless observatory. Proc. IODP, 319.

Satake K (2012) Tsunamis generated by submarine landslides. In: Yamada Y (ed) Submarine mass movements and their consequences. Advances in natural and technological hazards research, vol 31. Springer, Dordrecht/Heidelberg/London/New York, pp 475–484.

Sclater JG, Christie PAF (1980) Continental stretching: An explanation of the Post-Mid-Cretaceous subsidence of the central North Sea Basin. J. Geophys. Res., 85(B7), 3711–3739.

Seno T (1989) Philippine Sea plate kinematics. Modern Geology 14:87–97.

Sharman GR, Schwartz TM, Shumaker LE, Trigg CR, Nieminski NM, Sickmann ZT, Malkowski MA, Hourigan JK, Schulein BJ, Graham SA (2017) Submarine Mass Failure within the Deltaic Domengine Formation (Eocene), California (USA). Geosphere, 13.3, 950-973.

Shaw JH, Bilotti F, Brennan PA (1999) Patterns of Imbricate Thrusting. Geological Society of America Bulletin; August 1999; v. 111; no. 8; p. 1140–1154.

Shiraishi K, Moore GF, Yamada Y, Kinoshita M, Kimura G (in review) Seismogenic zone structures revealed by improved 3D seismic images in the Nankai Trough off Kumano. Prog. Earth Planet. Sci.

Strasser M, Moore GF, Kimura G, Kitamura Y, Kopf AJ, Lallemant S, Park JO, Screaton EJ, et al. (2009) Origin and evolution of a splay fault in the Nankai accretionary wedge. Nature Geosci, 2, 648-652.

Strasser M, Moore G, Kimura G, Kopf A, Underwood M, Guo J, Screaton E (2011) Slumping and mass-transport deposition in the Nankai forearc: Evidence from IODP drilling and 3-D reflection seismic data Geochemistry, Geophysics, Geosystems, 12, Q0AD13.

Strasser M, Henry P, Kanamatsu T, Thu MK, Moore GF and Expedition Scientists (2012) Scientific drilling of mass-trasnport deposits in the Nankai accretionary wedge: First results from IODP Exp 333. In: al., Y.Y.e. (ed) Submarine Mass Movements and Their Consequnces. Springer, New York.

Strasser M, Dugan B, Kanagawa K, Moore GF, Toczko S, Maeda L and Expedition 338 Scientists (2014) Proc. IODP, 338: Yokohama (Integrated Ocean Drilling Program).

Strasser M, Kopf A, Abegg FW, Asada M, Bachmann AK, Cuno P, Dos Santos Ferreira C, Fleischmann T, Fujiwara T, Hatakeyama E, Heesemann BR, Hillman JIT, Hoehne M, Huusmann H, Ikari M, Ikehara K, Jaeger FD, Kanamatsu T, Kang M, Kaul NE, Kioka A, Koelling M, Lange K, Luebben N, Matthiessen T, Mchugh CM, Meier A, Menapace W, Mochizuki K, Moernaut J, et al (2017) REPORT AND PRELIMINARY RESULTS OF R/V SONNE CRUISE SO251: Extreme events Archived in the GEological Record of Japan's Subduction margins (EAGER-Japan). Berichte, MARUM – Zentrum für Marine Umweltwissenschaften, Fachbereich Geowissenschaften, Universität Bremen.

Taira A (2001) Tectonic evolution of the Japanese Island Arc System. Ann. Rev. Earth Planet. Sci., 29, 109-134.

Taira A, Curewitz D, et al. (2005) CDEX Technical Report, Volume 1: Nankai Trough Seismogenic Zone Site Survey, Philippine Sea, Offshore Kii Peninsula, Japan.

Takahashi M (1999) Large felsic magmatism of Miocene outerzone of southwest Japan. Earth Mon. Extra, 23, 160-168.

Tanioka Y and Satake K (2001) Coseismic slip distribution of the 1946 Nankai earthquake and aseismic slips caused by the earthquake. Earth, Planets and Space, 53, 235-241.

ten Brink US, Geist EL, Andrews BD (2006) Size distribution of submarine landslides and its implication to tsunami hazard in Puerto Rico. Geophysical Research Letters, 33.

Ujiie K and Kimura G (2014) Earthquake faulting in subduction zones: insights from fault rocks in accretionary prisms. Progress in Earth and Planetary Science, 1:7.

Underwood MB and Moore GF (2012) Evolution of sedimentary environments in the subduction zone of southwest Japan: recent results from the NanTroSEIZE Kumano transect. In: Busby, C.J. & Azor, A.P. (eds) Tectonics of Sedimentary Basins: Recent Advances. Wiley-Blackwell, New York, 310-326.

Underwood MB, Moore GF, Taira A, Klaus A, Wilson MEJ, Fergusson CL, Hirano S, Steurer J (2003) Sedimentary and tectonic evolution of a trench-slope basin in the Nankai subduction zone of southwest Japan. Journal of Sedimentary Research, 73, 589-602.

Urgeles R and Camerlenghi A (2013) Submarine landslides of the Mediterranean Sea: Trigger mechanisms, dynamics, and frequency-magnitude distribution. Journal of Geophysical Research: Earth Surface, 118, 2600-2618.

Urlaub M, Talling PJ, Masson DG (2013) Timing and frequency of large submarine landslides: implications for understanding triggers and future geohazard. Quaternary Science Reviews 72(0):63–82.

Ward SN, Day S (2001) Suboceanic Landslides. 2002 Yearbook of Science and Technology, 249-352.

Wessel P, Smith WHF, Scharroo R, Luis J, Wobbe F (2013) Generic Mapping Tools: Improved Version Released. EOS Trans. AGU, 94(45), 409-410.

Westbrook GK, Thatcher KE, Rohling EJ, Piotrowski AM, Pälike H, Osborne AH, Nisbet EG, Minshull TA, et al. (2009) Escape of methane gas from the seabed along the West Spitsbergen continental margin. Geophysical Research Letters, 36.